





UNIVERSITAT  
ROVIRA I VIRGILI

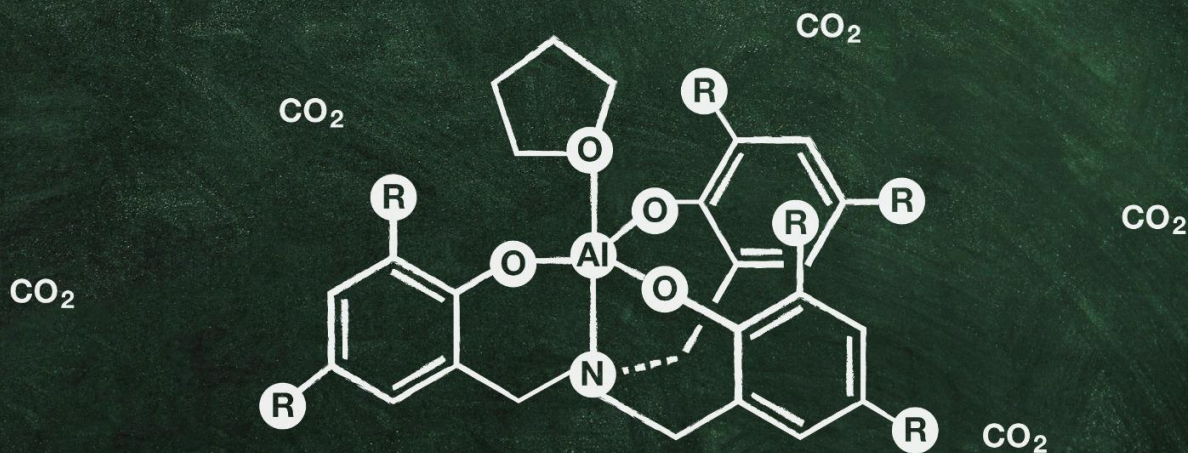
.  
.

7 ca di hUjcbU`8 Yg][ b`cZ7 UhU nglhg`Zcf`7 UfVcb`8 ]cl ]XY`  
F YWmW]b[ .

Á

Á

RU OEP ÁOU P Z7 ŠÒZ ÁZCÓÜ CEA



8 C7 HCF5 @H<9G=G`  
&\$%

UNIVERSITAT ROVIRA I VIRGILI

Computational Design of Catalysts for Carbon Dioxide Recycling

Joan González Fabra



UNIVERSITAT  
ROVIRA i VIRGILI

UNIVERSITAT ROVIRA I VIRGLI

Computational Design of Catalysts for Carbon Dioxide Recycling

Joan González Fabra



UNIVERSITAT ROVIRA I VIRGILI

Computational Design of Catalysts for Carbon Dioxide Recycling

Joan González Fabra

UNIVERSITAT ROVIRA I VIRGILI

Computational Design of Catalysts for Carbon Dioxide Recycling

Joan González Fabra

Joan González Fabra

# Computational Design of Catalysts for Carbon Dioxide Recycling

Ph.D. Thesis

Supervised by Dr. Carles Bo Jané



Tarragona

2018

UNIVERSITAT ROVIRA I VIRGILI

Computational Design of Catalysts for Carbon Dioxide Recycling

Joan González Fabra





UNIVERSITAT  
ROVIRA i VIRGILI

Dr. Carles Bo i Jané, professor de l'Institut Català d'Investigació Química,

FAIG CONSTAR que aquest treball, titulat "*Computational Design of Catalysts for Carbon Dioxide Recycling*", que presenta Joan González Fabra per a l'obtenció del títol de Doctor, ha estat realitzat sota la meua direcció a l'Institut Català d'Investigació Química, i que compleix els requisits per poder optar a la Menció Internacional.

---

Tarragona, 31 de Setembre de 2018

El director de la tesi doctoral

A handwritten signature in black ink, appearing to be 'C. Bo i Jané', written over a horizontal line.

Dr. Carles Bo i Jané

UNIVERSITAT ROVIRA I VIRGILI

Computational Design of Catalysts for Carbon Dioxide Recycling

Joan González Fabra

# Acknowledgements

Els qui les heu escrit ja ho sabeu; els qui les escriureu, prepareu-vos. Sí, són les línies més difícils d'escriure d'una tesi. Hi ha tantes persones a qui agrair, tants sentiments que expressar i tant de neguit pel que vindrà, que veus aquestes pàgines en blanc i no voldries deixar-te res, ni ningú. Per tant, començo pel principi.

Gràcies a l'Anna Clotet Romeu per animar-me a visitar l'ICIQ mentre buscava un lloc per fer les pràctiques externes del Grau de Química. Recordo com li explicava que jo em volia dedicar recerca, i que volia fer les pràctiques en aquest sentit. Gràcies a aquell qui em va rebre, em va acollir i em va presentar el centre, què feien allí i com: Carles Bo i Jané ha estat un magnífic tutor, mestre i mentor des del 2 de febrer de 2014, quan vaig posar el peu a l'ICIQ, fins el dia d'avui. Al seu costat he après molta química (i també com fer anar un ordinador), però sobretot he après a treballar, a veure la vida sempre des del cantó positiu (reconec que, a vegades, em costa una mica). Carles m'ha ensenyat a estimar la ciència i la recerca, des d'una vessant respectuosa amb la matèria que estudiem i amb la comunitat amb la qual compartim il·lusions i curiositat. Tot i això, la lliçó més gran que he après va ser: fem el què fem, perquè ens agrada; i, perquè, tot i les dificultats, quan tornem a casa, hi tornem contents i satisfets, en pau i estant a gust amb la gent que estimem. Per això ho fem, i per això ho hauriem de fer tot: pels qui estimem.

Aquests anys al laboratori de teòrics de l'ICIQ m'han permès conèixer gent magnífica. Tenim molta sort de treballar en un ambient agradable, tranquil i a la vegada divertit. Voldria agrair a aquells i aquelles que em van acollir els primers dies al laboratori, començant pel meu mestre (i jefe) Fernando Castro. Gràcies per la paciència i les primeres lliçons com a químic computacional, no tant pel reggaeton, ho he de dir. Gràcies pels bons moments, pels consells i l'ajuda dels companys i companyes que ja han marxat del laboratori de teòrics: Max García, Guillem Revilla, Luca Bellarosa, Lluís Artús, Marçal Capdevila, Damien Cornu, Víctor Fernández, Charles Goehry, Michael

Higham, Rositha Kuniyil, Oier Lakuntza, Xavi Sanz, Neyvis Almora, Miquel García i també lo Ximo Soriano. Menció especial a la Dolores Melgar per ser una guia més enllà de la ciència i pels bons moments dins i fora del laboratori. També a l'Stefano Serapian, el senyor dels mil idiomes. Com ens vas salvar la vida a Fulda i com se't troba a faltar! A Nuno Bandeira, el mestre que tenia assegut just al davant, però, a qui no preguntava mai només aixecant el cap, sinó que anava a seure al seu costat: sabia que podia aprendre molt allí. Quan vaig començar al laboratori creia que ell ho sabia tot. Encara ho crec. Gràcies per les hores d'aquests anys.

Segueixo amb els col·legues amb els quals encara tinc la sort de compartir laboratori. Gràcies a l'Adiran de Aguirre. Ha estat un plaer compartir Grau, Màster i Doctorat amb tu Adi, ets un pou de bondat. Gràcies a la Maria Besora per la saviesa i els dinars compartits amb la NV. Gràcies a l'Ignacio Funes i el seu esperit divulgatiu; a Rodrigo García i el seu català magnífic (no deixis de practicar-lo); a l'Àngel Luís Mudarra i el seu somriure inextingible; a Marcos Rellán i el seu humor àcid i políticament incorrecte (no per inconformista, sinó per políticament equivocat); a Franzika Hegner, Qiang Li, Mauro Fianchini, Bruna Sánchez, Shaofei Ni, Raúl Pérez, Bob Nguyën, Javi Navarro (quin gran fill ha parit Sabadell!), Manu Ortuño, Edvin Fako, Nathan Daelman, Konstantin Karaiovic, Paulina Pršlja, Albert Sabadell (deixa les amanides empaquetades!), Federico Dattila i Jordi Morales. Acabo amb els de casa, als tres membres del grup Bo pel seu suport i afecte: l'Anna Mateo, per ser una valenta inconformista que mira als ulls i parla sense por; la Mireia Segado, per ensenyar-me que una ideologia és una forma de vida per fer un món millor des de la pau i la felicitat; i, l'Enric Petrus, per ser un incomparable company i, encara que ell no s'ho cregui, un gran mestre. La menció final va pels imprescindibles. Gràcies al professor Feliu Maseras pel seu humor únic i la seva immesurable contribució a l'hora de generar un ambient de treball agradable al laboratori. Gràcies a la professora Núria López pels consells, per deixar-me ser la *bèstia petita* del laboratori i per propiciar les nostres "tertúlies de tietes" amb la Maria i la Vendrell. Gràcies a la Núria Vendrell per ser la líder moral dels tres grups teòrics i una companya de lluita digital i real. Gràcies també per la professionalitat i l'eficiència, al teu costat és molt fàcil

treballar; al Martin Gumbau, el senyor dels cables i les pantalles, per l'ajuda constant i per ensenyar-me a fer funcionar mig dignament un ordinador (tenim pendent una cerca de caixetes a costes ebrenques); al Moisés Àlvarez, per ensenyar-me el poder de les expressions regulars i tants altres estris i ginys informàtics, però sobretot per l'amistat i el companyerisme d'aquests anys.

I would like to thank also professor Rosa Bulo for her warm welcome in her group in Utrecht during three months. It was an exciting and beautiful stay where I felt like home. I would like to thank Manuel Louwerse, Jelle Boereboom, Stanislav Šimko and Katarína Stančiaková for their help and lessons during my stay. I never thought that I could learn so much in just three months.

Fora de l'àmbit científic, voldria donar les gràcies pel seu suport a tota la colla de la *piscina de can Joan*, enguany s'han quedat sense piscina i sense paella, però l'any vinent ho compensem. Gràcies a Pelló, Aitor, Carme, Àlex, Davinia, Ferran, Gemma, Judit, Neus, Lourdes, Núria, Àngela i JL per l'amistat. Gràcies a Júlio per ser el meu il·lustrador de referència durant aquests anys, prometo que quan sigui gran aprendré a combinar colors com cal; a Laura pels moments entranyables i per l'estima, no cal dir-ho, es nota; i, a Gerard per ser l'amic que mai falla, que sempre hi és, fins i tot quan no el crides, però el necessites. Sap que l'estimo, però no sap quant.

Gràcies a tota la bona gent de la Colla Jove Xiquets de Tarragona i especialment a les *xanetas* per ensenyar-me que junts ho podem tot. No hi ha res impossible, si tenim clar que no hi ha ningú més important que ningú. La vida és fer pinya i cuidar-se els uns als altres.

No em puc deixar a tota aquella gent que durant els últims anys m'han ensenyat que es pot estimar un projecte sense límits, que es pot donar tot sense esperar res a canvi. Tot per una manera d'entendre la vida i l'esperança de millorar-la. És gent que vol canviar el món, i a més, ho intenta. Han començat per un trosset preciós i únic del planeta. Gràcies a la Liz Castro, Ariadna Isern, Anna Llord, Ricard Ibáñez, Núria Quintana, Arnau Galobardes, lo puto Jordi Calvís, David Ros, Oriol Codina, Josep Sabaté, Miquel Noguera, Quim Delgado, Laia Morgui, Galdric Peñarroja, Ferran

Garriga, Gemma Cots, Rosa Alentorn, Jordi Salvador, Josep Maria Nogué, Jordi Roura i Lola Martínez. Sou licor d'arròs, família. Seguint amb els separatistes, però ara els de prop de casa. Gràcies a l'esperit sant, també conegut com a Toni Rosich; al MHC Gilbert Frigola, a la genial Irene Martín, al savi Jordi Jaria, a l'amic prèmium Xavi Jornet, a la jefa Irene Fornós, a la referent Josepa Ribera, a l'incorruptible en la bondat Víctor Reverter i al mestre i pare Pere Grau, us estaré eternament agraït.

Finalment, els culpables de tot. Els qui et posen dret, et donen unes sabates i et diuen: “ànims, tu pots! Però qui ha de caminar ets tu...” Gràcies a Noe, Agustí i Lia per donar sense mirar, sense esperar res a canvi. Gràcies a mons iaïos, per lluitar contra una vida cruel i injusta, i posar les bases d'un món millor pels seus fills. A mons pares Janet Fabra i Juan González, per ensenyar-me que l'esforç ens fa imparables i l'amor, inoblidables. A ma germana, Maria, per ser tan gran i fer-me sentir tan *xocotet* davant la seua immensitat.

I gràcies a tu, bonica, per donar-li sentit, per fer-ho nostre. Per cridar junts que “no tinim tamor” i, a cau d'orella, “tot anirà bé”.

# Funding Agencies



UNIVERSITAT ROVIRA I VIRGILI

Computational Design of Catalysts for Carbon Dioxide Recycling

Joan González Fabra



# List of Publications

## Related with this Thesis

**Al(III) Catalyzed Formation of Poly(limonene)carbonate: DFT Analysis of the Origin of Stereoregularity.** Peña Carrodeguas, L.; González-Fabra, J.; Castro-Gómez, F.; Bo, C.; Kleij, A. W. *Chemistry – A European Journal*, **2015**, *21*, 6115.

**A Metal-free Synthesis of N-Aryl Carbamates under Ambient Conditions.** Guo, W.; González-Fabra, J.; Bandeira, N.; Bo, C.; Kleij, A. W. *Angewandte Chemie International Edition*, **2015**, *54*, 11686.

**Mechanistic Insights into the Carbon Dioxide-Cyclohexene Oxide Copolymerization reaction: Is one Metal Center enough?** González-Fabra, J.; Castro-Gómez, F.; Kleij, A. W.; Bo, C.; *ChemSusChem*, **2017**, *10*, 1233.

**Caught in the act: Deciphering key intermediates in the transformation of carbon dioxide into heterocyclic products.** Huang, R.; Rintjema, J.; González-Fabra, J.; Martín, E.; Escudero Adán, E. C.; Bo, C.; Urakawa, A.; Kleij, A. W. *Manuscript submitted for publication*.

**DFT Studies on the Al(III) Catalyzed Formation of Cyclic Carbonates from CO<sub>2</sub> and Epoxides: Towards a Quantitative Evaluation of the Catalytic Activity.** González-Fabra, J.; Castro-Gómez, F.; Sameera, W.M.C.; Nyman, G.; Kleij, A. W.; Bo, C.; *Manuscript in preparation*.

## Not Related with this Thesis

**Thermodynamic Stability of Heterodimetallic [LnLn'] Complexes: Synthesis and DFT Studies.** González-Fabra, J.; Bandeira, N. A. G.; Velasco, V.; Barrios, L. A.; Aguilà, D.; Teat, S. J.; Roubeau, O.; Bo, C.; Aromí, G.; *Chemistry – A European Journal*, **2017**, *23*, 5117.

**Efficient Vanadium-Catalyzed Aerobic C-C Bond Oxidative Cleavage of Vicinal Diols.** Amadio, E.; González-Fabra, J.; Carraro, D.; Denis, W.;

Gjoka, B.; Zonta, C.; Bartik, K.; Cavani, F.; Solmi, S.; Bo, C.; Licini, G.  
*Advanced Synthesis & Catalysis*, **2018**, 360. DOI: 10.1002/adsc.201800050.

**Selective Lanthanide Distribution within a Comprehensive Series of Heterometallic [LnPr] Complexes.** Aguilà, D.; Velasco, V.; Barrios, L. A.; González-Fabra, J.; Bo, C.; Teat, Simon J.; Roubeau, O.; Aromí, G. *Inorganic Chemistry*. DOI: 10.1021/acs.inorgchem.8b01112.

**PubChemDFT: A live experiment that computes and tweets molecules.** González-Fabra, J. Mateo, A.; Álvarez-Moreno, M.; Gumbau, M.; Petrus, E.; Bo, C. *Manuscript in preparation*.

# Table of Contents

Chapter 1: General Introduction .....	23
1.1 Climate Change and Carbon Dioxide Utilization .....	23
1.2 Carbon Dioxide as Carbon Building Block .....	27
1.3 Al-Catalyzed Reaction of CO <sub>2</sub> and Epoxides towards Polycarbonates and Cyclic Carbonates .....	30
1.4 Aims and Objectives .....	34
Chapter 2: Computational Methods .....	37
2.1 Quantum Mechanics .....	37
2.2 Density Functional Theory .....	40
2.2.1 Functionals of the electron density .....	43
2.2.2 Including dispersion interactions into DFT calculations .....	45
2.3 Solvation Models .....	47
2.4 Translational Entropy Corrections .....	48
2.5 Adaptive QM/MM Metadynamics Simulations .....	50
2.5.1 Metadynamics .....	50
2.5.2 Adaptive multiscale methods .....	53
Chapter 3: Cyclic Carbonates .....	55
3.1 Introduction .....	55
3.1.1 Previous Mechanistic Studies .....	58
3.2 Quantitative Evaluation of the Catalytic Activity .....	60
3.2.1 Goals and Motivation .....	60
3.2.2 Computational Details .....	61
3.2.3 Results and Discussion .....	62

3.2.3.a Reaction mechanism of cyclic carbonate formation from CO <sub>2</sub> and 1,2-epoxyhexane .....	62
3.2.3.b Evaluation of different DFT functionals. The key role of dispersion corrections .....	67
3.2.3.c Realistic approximations to account the translational entropy in solution.....	70
3.2.4 Conclusions .....	75
3.3 Epoxy-Alcohols as Building Blocks for Functionalized Cyclic Carbonates .....	76
3.3.1 Goals and Motivation.....	76
3.3.2 Computational Details .....	78
3.3.3 Results and Discussion .....	79
3.3.3.a Catalyst reaction order.....	79
3.3.3.b Determination of CO <sub>2</sub> insertion selectivity.....	81
3.3.3.c Revealing the crucial role of water as proton shuttle .....	82
3.3.3.d CO <sub>2</sub> insertion and ring-closing in one step .....	85
3.3.3.e Racemization of Glycidol Carbonate .....	88
3.3.3.f Vibrational Frequencies Analysis: IR <i>in operando</i> .....	89
3.3.4 Conclusions .....	90
Chapter 4: N-Aryl Carbamates.....	93
4.1 Organocatalyzed N-Aryl Carbamates from Cyclic Carbonates.....	93
4.1.1 Introduction.....	93
4.1.2 Goals.....	98
4.1.3 Computational Details .....	98
4.1.4 Results and Discussion .....	99
4.1.4.a Uncatalyzed Reaction Mechanism .....	99

4.1.4.b N-aryl carbamate formation catalyzed by TBD .....	102
4.1.5 Conclusions .....	104
Chapter 5: Polycarbonates .....	105
5.1 Introduction .....	105
5.1.1 Previous Mechanistic Studies .....	110
5.2 Mechanistic Study on Copolymerization Reactions .....	113
5.2.1 Goals and Motivation.....	113
5.2.2 Computational Details .....	113
5.2.3 Results and Discussion .....	114
5.2.3.a Initiation of polymerization and CO <sub>2</sub> insertion .....	114
5.2.3.b The propagation step through bimetallic mechanisms ..	116
5.2.3.c Evaluation of the catalytic activity via modification of the ligand.....	122
5.2.4 Conclusions .....	124
5.3 Origin of the Stereoregularity of Poly(limonene)carbonate.....	126
5.3.1 Goals and Motivation.....	126
5.3.2 Computational Details .....	126
5.3.3 Results and Discussion .....	127
5.3.3.a The effect of the nucleophile in the initiation step .....	127
5.3.3.b Insertion of CO <sub>2</sub> and ring-closing to LO-CyC .....	129
5.3.3.c Propagation of the LO-CO <sub>2</sub> copolymer .....	132
5.3.4 Conclusions .....	136
Chapter 6: Effect of CO <sub>2</sub> Pressure .....	139
6.1 Multiscale Metadynamics as Exploring Tool for Reactivity.....	139
6.1.1 Introduction.....	139

6.1.2 Goals.....	143
6.1.3 Computational Details .....	144
6.1.4 Groundwork.....	145
6.1.5 Results and Discussion .....	147
6.1.5.a Racemization of Cyclic Carbonates .....	147
6.1.5.b Decarboxylation.....	156
6.1.6 Conclusions .....	160
Chapter 7: Conclusions .....	163
References .....	167

# Abstract

The utilization of carbon dioxide as chemical substrate has become a popular strategy from an environmental and economic perspective to mitigate CO<sub>2</sub> emissions to the atmosphere and, at the same time, reduce the petroleum dependency to provide carbon based substrates. The activation of carbon dioxide is not a straightforward process. Actually, high internal energy substrates are required to compensate its thermodynamic stability, and also, efficient catalysts are crucial to overcome the high kinetic barrier of activation. In this line, homogeneous catalysis has become an interesting technique to achieve such purpose due to its versatility, flexibility and chemoselectivity. Therefore, we aim to improve our understanding on CO<sub>2</sub> fixation processes, in order to design new catalysts that present higher activity and selectivity, thus contributing to scale up the CO<sub>2</sub> fixation processes at the industrial level.

The design of new catalysts is a complex task that requires the combination of several experimental and theoretical techniques. One of the most relevant is molecular modelling, which allow to describe the system in detail and to understand how the system behaves or how a reaction mechanism takes place. Nowadays, the combination of two factors, being the increase of the computational power and the improved efficiency of the theoretical algorithms, enable computational chemists to study large systems at a reasonable level of accuracy, to mimic the experimental conditions, and consequently, obtain crucial information on the studied system.

In this Thesis we study computationally the reaction of carbon dioxide and epoxides catalyzed by a binary catalytic system formed by a halide and an aluminum aminotriphenolate complex.

The first chapter contains a summary of the effect of CO<sub>2</sub> excess in the atmosphere, as well as the difficulties of activating CO<sub>2</sub>, together with several reported catalytic systems used nowadays that achieved relevant performances on CO<sub>2</sub> fixation. Then, there is a brief description of the

catalyst and the particularities of epoxides. Finally, we detail the main goals of each chapter of the Thesis.

In Chapter 2, we explain the theoretical background of the methodology used in this Thesis. We summarize the main aspects of Density Functional Theory and the different families of functionals, we depict the solvation models and entropic corrections used in the calculations presented in the next chapters, and finally, we explain the characteristics and details of adaptive multiscale metadynamics used in the last chapter of the Thesis.

The first chapter that collects results is related to the formation of cyclic carbonates. The chapter is divided in two parts. In the first one, we present a quantitative evaluation of the catalytic activity of the binary system used in the reaction between 1,2-epoxyhexane and CO<sub>2</sub>. We evaluate different aspects that affect the calculated Gibbs free-energy, like solvation, translational entropy and the chosen DFT functional. In the second part of the chapter we investigate the reaction mechanism of functionalized epoxides, considering glycidol as a model of epoxy-alcohols. A detailed mechanistic study is presented, explaining the reaction order of the catalyst, the regioselectivity and the enantioselectivity observed in the experiments.

Chapter 4 is not related directly on CO<sub>2</sub> fixation but the utilization of cyclic carbonates, which are the products of the reaction studied in the previous chapter, to produce high-value chemicals. In this case, we elucidate the reaction mechanism between cyclic carbonates and arylamines, catalyzed by a guanidine based organocompound, to selectively produce N-aryl carbamates.

The reaction between CO<sub>2</sub> and epoxides may lead to polycarbonates, which are the alternative product to cyclic carbonates. In the fifth chapter we investigate the copolymerization mechanism of internal epoxides considering several active species of the catalyst. In this part, we compare the catalytic activity of a single complex with two separated complexes, and even a non-covalent dimeric ensemble of the catalyst. We also modify the catalytic system to computationally benchmark its activity. The second part of the chapter is a more specific study, related to the mechanism elucidation of limonene oxide



copolymerization with carbon dioxide. Limonene oxide is a biorenewable substrate with a complex structure that presents three stereocenters. Consequently, we pay special attention on the stereoregularity of the obtained copolymer, considering multiple reaction pathways and evaluating its feasibility.

The last chapter where we present our results is not based on DFT methods. We move to adaptive multiscale metadynamics to evaluate the effect of CO<sub>2</sub> pressure in the free-energy barrier of two different reactions of cyclic carbonates: decarboxylation and racemization. In the last chapter of the Thesis, the most relevant conclusions of each chapter can be found.

UNIVERSITAT ROVIRA I VIRGILI

Computational Design of Catalysts for Carbon Dioxide Recycling

Joan González Fabra

*"Scientists do not coddle ideas. They crash test them. They run them into a brick wall at sixty miles per hour and examine the pieces. If the idea is sound, the pieces will be that of the wall."*  
*Anonymous*

# Chapter 1

## General Introduction

### 1.1 Climate Change and Carbon Dioxide Utilization

World population has experienced a continuous growth since the Great Plague in 1350 (at that time, around 370 million people lived on the planet). However, the highest growth rates occurred between 1955 and 1975, increasing the world population above 1.8% per year. In 1960, 3 billion people lived on the planet. Nowadays, more than 7.4 billion people share the natural resources of the Earth.<sup>[1]</sup> Food production was one of the first problems due to this demographic increase, which was mitigated in the first half of the 20<sup>th</sup> century by the Haber-Bosch process that allowed the chemical fixation of nitrogen in the form of ammonia to easily produce fertilizers, thus increasing the efficiency of our crops.<sup>[2]</sup>

A second concern is the continuous increase of energy consumption due to both the increase of population and a higher energy demand in our society.

Currently, energy consumption increases faster than population. According to the “World Energy Outlook 2016” report of the International Energy Agency, in the 2000-2014 period world population growth was 26%, whereas the increase in energy demand was 56%. This energy dependence situation is worsened by the current energy production processes based on burning fossil fuels, which first, are not renewable and second, generate large amounts of polluting waste like carbon dioxide (CO<sub>2</sub>).

In 2015, CO<sub>2</sub> levels in the atmosphere surpassed 400ppm for the first time in history. In June 2018, the CO<sub>2</sub> concentration in volume was around 408.47ppm (see **Figure 1.1**).<sup>[3]</sup>

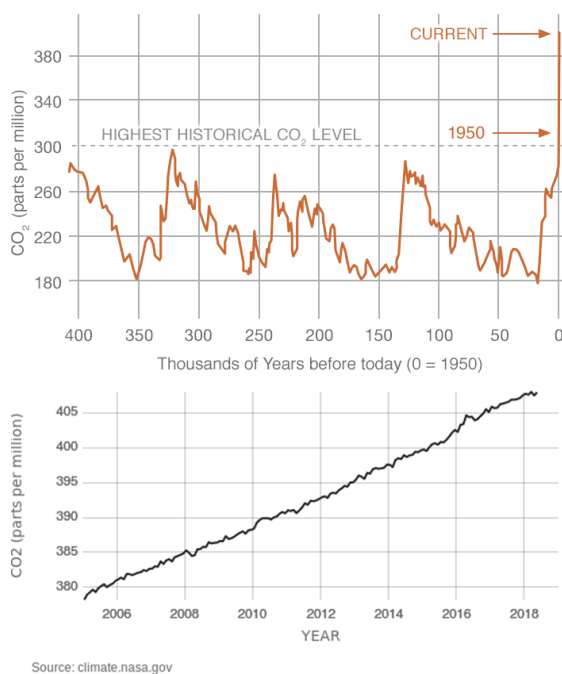
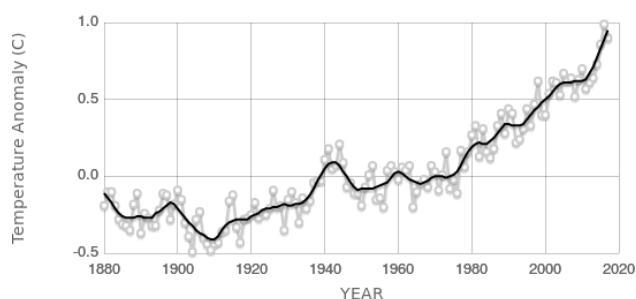


**Figure 1.1** CO<sub>2</sub> concentration in the atmosphere measured at Mauna Loa Observatory, Hawaii. Historical levels (top) and a detailed evolution of CO<sub>2</sub> levels in recent years (bottom).

Carbon dioxide (CO<sub>2</sub>) is the main sub-product of many human activities such as logging and combustion of fossil fuels.<sup>[4]</sup> Moreover, CO<sub>2</sub> is also released through natural chemical processes like respiration, decomposition of organic

materials and volcanic eruptions. According to the “State of the Climate in 2016” report from the National Oceanic and Atmospheric Administration (NOAA) and the American Meteorological Society, the amount by which atmospheric carbon dioxide increases each year has roughly quadrupled since the 1960s. In fact, the global growth rate of atmospheric CO<sub>2</sub> has risen from  $0.6 \pm 0.1$  ppm per year in the early 1960s to an average of  $2.3 \pm 0.6$  ppm per year during the past ten years. Moreover, the increase in global annual mean CO<sub>2</sub> from 2015 to 2016 was  $3.5 \pm 0.1$  ppm ( $0.88\% \pm 0.03\%$ ), the largest annual increase observed in the 58-year atmospheric measurement record.<sup>[5]</sup>

Carbon dioxide is an important heat-trapping (greenhouse) gas. Actually, CO<sub>2</sub> warms the lower part of atmosphere, hence the increase in atmospheric concentrations of CO<sub>2</sub> and other greenhouse gases such as methane, nitrous oxide and ozone have caused the rise in the average global temperature since the 20th century. In **Figure 1.2**, we present the change in global surface temperature in the 1880-2017 period. The maximum increase was observed in 2016, when there was a 1°C increase respect the historic average. Carbon dioxide is of greatest concern because it causes a larger overall warming influence than all of these other gases combined and because it has a long atmospheric lifetime due to its high thermodynamic and kinetic stability.



Source: climate.nasa.gov

**Figure 1.2** Global surface temperature evolution (°C) from 1880 to 2017. The year 2016 ranks as the warmest in the records.

The increase of global surface temperature leads to many ecological problems like the decrease in arctic ice surface (13.2% per decade) or decrease in the

global mass of ice sheets ( $127 \pm 37$  Gt per year). Consequently, the sea level has increased 3.2 mm per year since 1880.<sup>[6]</sup>

Two different strategies have arisen to mitigate CO<sub>2</sub> emissions to the atmosphere.<sup>[7]</sup> The first strategy is CO<sub>2</sub> capture and storage<sup>[7c]</sup> through different techniques like chemical absorption (ethanolamine, diethanolamine, potassium or sodium hydroxide, etc.), adsorption (alumina, zeolites, etc.), cryogenics (dry ice formation at low temperatures), polymer-based membranes (polyphenylene oxide, polyionic liquids, etc.), inorganic membranes like zeolites or ceramic membranes, and using algal or microbial systems.<sup>[8]</sup> Carbon dioxide processed in different physical forms has many applications such as additive in foods and beverages, inert gas, fire extinguisher, or as supercritical solvent.<sup>[9]</sup>

Alternatively, the second strategy is the chemical fixation of CO<sub>2</sub> into molecules, thus using CO<sub>2</sub> as carbon feedstock.<sup>[10]</sup> This approach tackles both problems mentioned above: reduce the dependence on petroleum as carbon source and store energy chemically in molecules.<sup>[10c]</sup> Actually, CO<sub>2</sub> utilization as C1 building block presents a major challenge due to the high thermodynamic and kinetic stability of CO<sub>2</sub>. In order to overcome such limitation, the scientific community has invested many efforts in the design of efficient catalytic systems to transform CO<sub>2</sub> into value-added products in combination with high internal energy substrates that compensate the high stability of CO<sub>2</sub>. Currently, several catalysts are robust enough to convert CO<sub>2</sub> obtained directly from several industrial processes, still maintaining the high activity of the catalyst. Additionally, the high chemoselectivity showed by some catalytic systems prevents obtaining undesired side-products in CO<sub>2</sub> fixation processes. Consequently, several economic analysis draw attention to the good economic perspective of chemical fixation of CO<sub>2</sub> in the industry.<sup>[11]</sup>

Nowadays, around 115 million tons of CO<sub>2</sub> are used annually by the global chemical industry. However, this is a tiny amount compared to the 24 billion tons of annual anthropogenic CO<sub>2</sub> emissions.<sup>[8]</sup> Consequently, we cannot exclude any of the two strategies presented above to mitigate CO<sub>2</sub> emissions and reduce CO<sub>2</sub> concentration in the atmosphere. Both technologies have to

be improved in order to become more efficient, therefore more widely used.<sup>[12]</sup> In the work summarized in this Thesis I aim to contribute to improving the efficiency of several CO<sub>2</sub> fixation processes via the chemical reaction of CO<sub>2</sub> with epoxides, proposing new routes to produce valuable products that are nowadays produced in the industry using conventional synthetic processes.

## 1.2 Carbon Dioxide as Carbon Building Block

The chemical utilization of CO<sub>2</sub> as carbon feedstock is motivated by the reduction of the CO<sub>2</sub> emission into the atmosphere. An example of a chemical reaction where CO<sub>2</sub> may be used as reagent is the formation of cyclic carbonates (CyCs) from epoxides. In fact, CyCs are interesting molecules that may be used as polar aprotic solvents or as precursors of polycarbonates and pharmaceuticals among other high-value products.

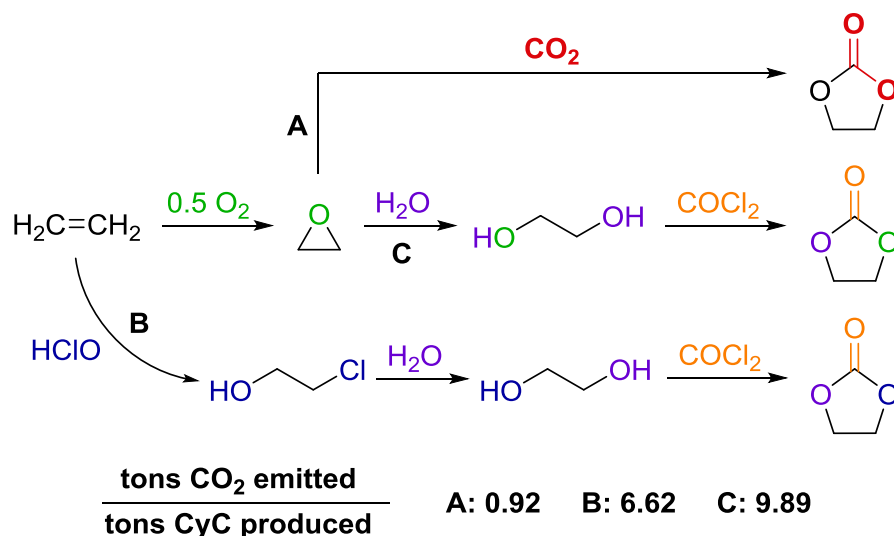


**Figure 1.3** Reaction routes to obtain ethylene carbonate from ethylene. A: Oxidation to ethylene oxide and CO<sub>2</sub> addition. B: Chlorination with hydrochloric acid (phosgene route). C: Hydrolysis of ethylene oxide (phosgene route). Relation of tons of CO<sub>2</sub> emitted respect tons of ethylene carbonate produced for each process is showed.

As an example, two conventional processes to produce ethylene carbonate from ethane are depicted in **Figure 1.3**.<sup>[10a]</sup> Additionally, the synthetic route labeled **A** is also showed, which is based on the oxidation of ethane to produce ethylene oxide and followed by CO<sub>2</sub> coupling towards ethylene carbonate through a catalyzed reaction at mild reaction conditions. The two conventional routes (**B** and **C**) are based on phosgene reaction with ethylene glycol.

In the **B** pathway, ethylene is chlorinated by hypochlorous acid forming 2-chloroethanol, which is then hydrolyzed to ethylene glycol. The third synthetic route (**C**) is based on the hydrolysis of ethylene oxide to ethylene glycol to produce ethylene carbonate. The ratio of tones of CO<sub>2</sub> emitted over tons of ethylene carbonate produced for the three processes is showed in the bottom of **Figure 1.3**. As it can be seen, route **A** where CO<sub>2</sub> is used as carbon feedstock presents a considerably lower CO<sub>2</sub> emission than conventional phosgene-based routes.

Nowadays, a wide variety of chemical reactions using CO<sub>2</sub> as substrate have been reported. Activation of CO<sub>2</sub> may be overcome by using different types of catalysts and reactants, each according to CO<sub>2</sub> reactivity. Carbon dioxide presents one electrophilic center, which is the carbon atom, and two different nucleophilic targets, which are the two oxygen atoms and the  $\pi$  system of the two double bonds between carbon and oxygen atoms (see **Figure 1.4**).

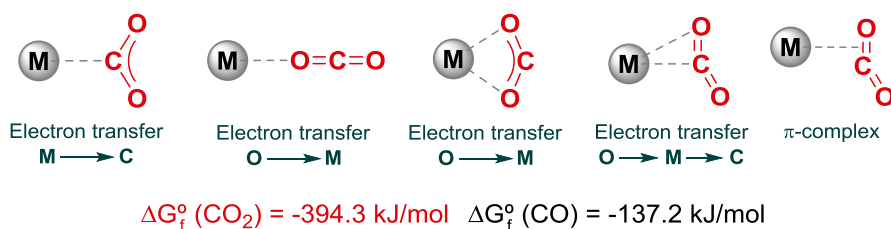


**Figure 1.4** Five chelating modes of CO<sub>2</sub> to a generic metal complex illustrating the different reactive sites of the substrate. Standard Gibbs free-energy of formation of CO<sub>2</sub> and CO are depicted below to compare their relative stability.

In addition, in **Figure 1.4** we show the standard Gibbs free-energy of formation of CO<sub>2</sub> and CO. Carbon monoxide is used in many carbonylation



reactions, like Fischer-Tropsch, due to its high reactivity. Contrarily, carbon dioxide is more stable, which is the main motivation to design efficient catalytic systems for CO<sub>2</sub> fixation.

Taking into consideration the different reactive sites of the CO<sub>2</sub> molecule, several synthetic strategies have been reported to activate CO<sub>2</sub>. The reduction of CO<sub>2</sub> to produce CH<sub>x</sub>O<sub>y</sub> moieties is one of the most investigated processes in CO<sub>2</sub> fixation.<sup>[13]</sup> Actually, the CO<sub>2</sub>/H<sub>2</sub> coupling to produce formic acid, formaldehyde or methanol is a challenging and motivating catalytic reaction that has been explored by using both molecular complexes, supramolecular structures and solid surfaces as catalysts.<sup>[14]</sup> Reduction of CO<sub>2</sub> using H<sub>2</sub> is crucial to produce fuels from a renewable carbon source such as CO<sub>2</sub>.<sup>[15]</sup>

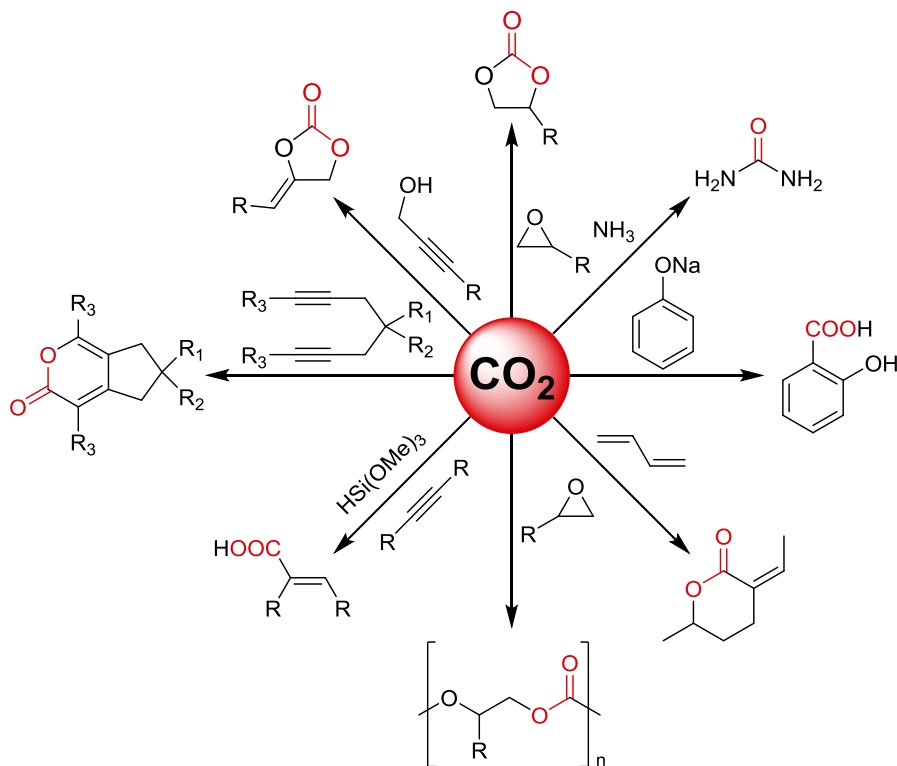


**Figure 1.5** Schematic representation of the main transformations of CO<sub>2</sub> to high-value chemicals. The two CO<sub>2</sub> reactions with epoxides are investigated in this Thesis.

As alternative to fuel production, there are other processes where CO<sub>2</sub> is used as substrate that have been industrialized. For example, the production of urea or CyCs, which are interesting monomers for polyurethanes and polyureas or polycarbonates, respectively.<sup>[16]</sup> Many other reactions using CO<sub>2</sub> are studied (see **Figure 1.5**) and some of these are already being implemented in alternative industrial processes to the conventional routes, which are more pollutant and less atomic efficient than CO<sub>2</sub> based.<sup>[10c, 16]</sup>

The formation of salicylic acid (the precursor to aspirin) was reported by Hermann Kolbe and Rudolf Schmitt at the end of the 19<sup>th</sup> century.<sup>[17]</sup> The Kolbe-Schmitt process is a carboxylation reaction of sodium phenoxide with CO<sub>2</sub> under 100 atm of pressure and 125 °C to produce salicylic acid after treating sodium salicylate with sulfuric acid. This process as well as sodium bicarbonate formation from sodium hydroxide and CO<sub>2</sub> are some of the first examples of chemical reactions where CO<sub>2</sub> is used as substrate. Nowadays, more complex products can be formed using other substrates like dienes,<sup>[18]</sup> alkynes,<sup>[19]</sup> epoxides, amines<sup>[20]</sup> or alkenes<sup>[19b]</sup> and CO<sub>2</sub>.

In this Thesis I focus on the computational study of reaction mechanisms of formation of cyclic carbonates and polycarbonates, as well as other related reactions involving these two important products.

### 1.3 Al-Catalyzed Reaction of CO<sub>2</sub> and Epoxides towards Polycarbonates and Cyclic Carbonates

As we pointed out in the previous section, the high thermodynamic stability of CO<sub>2</sub> has to be compensated by high internal energy substrates. We have considered epoxides as substrate due to their versatility, availability and easy handling.

Cyclic ethers that form a three-atom ring, also known as epoxides or oxiranes, have been widely used in synthetic chemistry. Ethylene oxide, was first synthesized by Charles-Adolphe Wurtz in 1859.<sup>[21]</sup> An alternative method to produce epoxides is the direct oxidation by air using a silver catalyst, which

was patented in 1931 by Lefort and six years later was industrialized by Union Carbide. Nowadays, Shell has improved this methodology, which currently accounts for the majority of ethylene oxide production worldwide. Unfortunately, direct oxidation is limited to ethylene and does not work for other alkenes. Consequently, alternative techniques have been developed for epoxide synthesis (see **Figure 1.6**).

Epoxides are ideal substrates for CO<sub>2</sub> chemical fixation. The most used nowadays are the simplest ones: ethylene oxide and propylene oxide. Nevertheless, cyclohexene oxide and other internal epoxides are also employed both in polycarbonate or CyC synthesis. More complex epoxides like limonene oxide present a greater challenge due to their structural complexity. In fact, they arouse great interest in the scientific community because some epoxides like limonene oxide may be obtained from renewable sources. For example, limonene oxide is synthesized from limonene, which is the major component in the oil of citrus fruits.

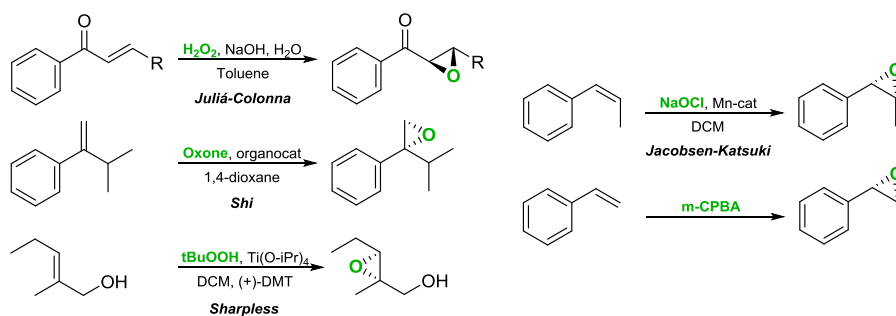


**Figure 1.6** Synthetic routes for the epoxidation of alkenes.

The reaction of CO<sub>2</sub> and epoxides may lead to two different products, cyclic carbonates or polycarbonates, depending on the catalytic system and the reaction conditions (see **Figure 1.7**). On one hand, CyCs are useful organic compounds as monomers for polycarbonate production, but are also used as intermediate in fine chemicals industry. Additionally, CyCs are also used as polar aprotic solvents or as high permittivity component of electrolytes in lithium batteries.

On the other hand, the direct copolymerization of epoxides and CO<sub>2</sub> towards polycarbonates may also take place. Polycarbonates are widely produced in the polymer industry and may be used in electronic components, as automotive, aircraft, railway and security components, in niche and medical applications, in mobile phones or as construction materials. Actually, polycarbonates used in engineering are strong and resistant transparent materials. They are thermoplastic polymers that can be easily manipulated, molded and thermoformed.

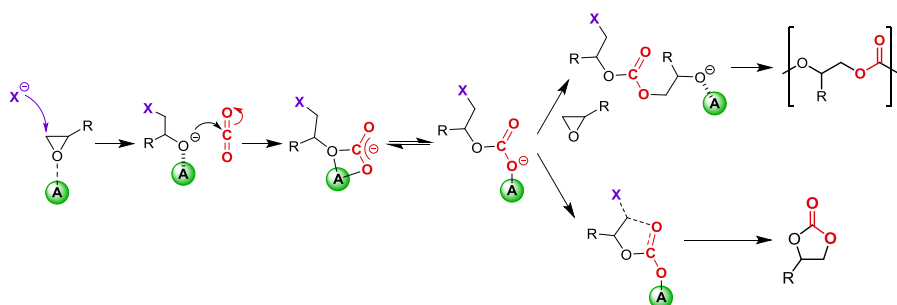


**Figure 1.7** Schematic representation of a tentative CO<sub>2</sub> reaction mechanism with epoxides to produce either polycarbonates or cyclic carbonates. The reaction may be catalyzed by an electron withdrawing actor like a Lewis acid (A) and a nucleophilic co-catalyst (X).

In recent years, the interest of the scientific community in the design of active and selective catalysts for the reaction of CO<sub>2</sub> and epoxides is constantly growing. Actually, the designed catalysts have to guarantee different aspects like decreasing the reaction time, increasing the chemoselectivity between polycarbonate and cyclic carbonate, and increasing the enantioselectivity for enantiomeric epoxides.

In order to accomplish such requirements, homogeneous catalysts based on transition metals<sup>[22]</sup> like cobalt,<sup>[23]</sup> chromium,<sup>[24]</sup> iron<sup>[25]</sup> or zinc<sup>[26]</sup> have gained much attention in the community. Nevertheless, many catalysts based on magnesium<sup>[27]</sup> or aluminum<sup>[28]</sup> have also been reported to show great performance. In combination with these metals, many different ligands have been designed to improve their catalytic efficiency. The most popular catalysts both for CyC and polycarbonate formation have been collected in **Figure 1.8**.

It is worth mentioning the first reported catalyst by Inoue et al. in 1983 that was used initially for cyclic carbonate synthesis but later on in 1986 also proved to be active catalyzing copolymerization reactions.<sup>[29]</sup> The catalyst was based on a porphyrin ligand and aluminum as metal center. Several modifications of this catalyst improved its performance. Sometimes the first reported ligand is not the most popular one. Actually, in this case, the most widely used and studied is the salen ligand. The reaction mechanism and catalytic performance of Cr-salen and Co-salen catalysts have been investigated in detail by Darensbourg et al. among others.<sup>[30]</sup> However, zinc or magnesium have also been used as metal centers for salen complexes.

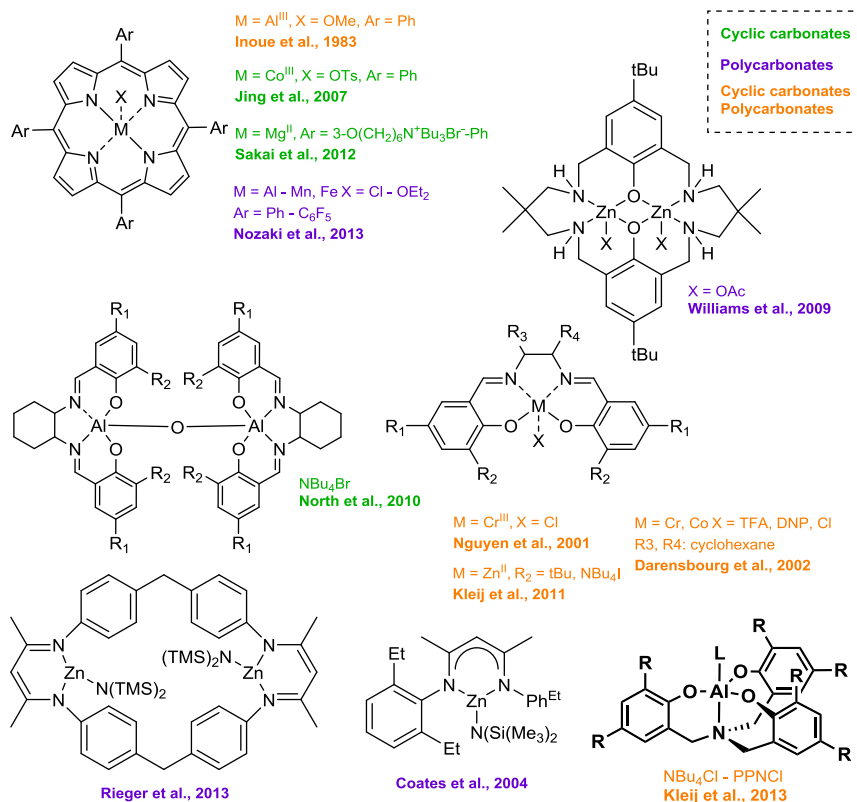


**Figure 1.8** Popular reported metal complexes to catalyze the reaction between CO<sub>2</sub> and epoxides to produce either cyclic carbonates or polycarbonates.

In this Thesis we study the reaction mechanism of CO<sub>2</sub> fixation reactions with epoxides catalyzed by an Al-based complex. This Al complex is easily

synthesized combining the aminotriphenolate ligand with trimethylaluminum (see **Figure 1.9**). The aminotriphenolate ligand was first synthesized in 1922 by Zemplén and Kunz.<sup>[31]</sup> However, aminotriphenolate started being used as a ligand in coordination complexes just 20 years ago.<sup>[32]</sup> One of the main differences between aminotriphenolate complex with other widely used complexes based on salen or porphyrins ligands is that the salen and porphyrin-based metal complexes adopt a planar conformation, while the aminotriphenolate ligand forms trigonal bipyramid complexes with aluminum.

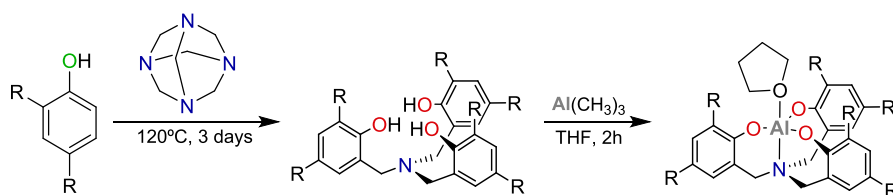


**Figure 1.9** Two-step synthetic route to Al-aminotriphenolate complex from phenol derivatives, methanamine and trimethylaluminum.

Kleij et al. have reported high catalytic activity of this complex in epoxide/ $\text{CO}_2$  coupling reaction to produce both cyclic carbonates and polycarbonates.<sup>[33]</sup>

## 1.4 Aims and Objectives

The main goal in this Thesis is to investigate computationally the mechanistic pathways of  $\text{CO}_2$  fixation reactions. In fact, computational chemistry has become a crucial tool for mechanism elucidation in recent years.<sup>[30c, 34]</sup> In this Thesis we complement our computational results with the experimental data provided by Kleij's group. In Chapters 3, 4 and 5 our results are presented with theirs, thus enhancing the comprehension of both and corroborating the proposed mechanisms. The collaboration between our groups has been fruitful and efficient because we mutually benefit in a symbiotic manner, hence improving the catalytic system using the mechanistic studies and at the same time, facilitating the mechanism elucidation using the characterization

and kinetic experiments. This strategy has proved to be effective in many other reported studies that lead to a better comprehension of complex systems.<sup>[24a, 27b, 35]</sup> Next, we will summarize the contents and objectives of each chapter of the Thesis.

In Chapter 2 we present the theoretical background of the methodology employed in the next chapters. We mainly used Density Functional Theory (DFT) based methods, which are the most used methodology in homogeneous catalysis modelling due to its high accuracy describing reactive events and low computational time. We also describe the entropic corrections that we consider in the calculations showed during the Thesis. These entropic corrections are analyzed in detail in Chapter 3. Additionally, we explain the theoretical background of adaptive multiscale metadynamics that we use in Chapter 6.

Chapter 3 is organized in two parts, both regarding the study of cyclic carbonates formation. In the first part, we present a general investigation on the i) effects of solvation, ii) the accounting of entropy and iii) the used DFT functional on the Gibbs free-energy profile obtained for the carboxylation of 1,2-epoxyhexane to produce the corresponding cyclic carbonate. In the second part we detail the elucidation of the glycidol reaction mechanism to form glycidol carbonate from CO<sub>2</sub>. Our results are complemented with experiments to determine the reaction order of the catalyst, as well as the regioselectivity and enantioselectivity of the process.

In Chapter 4 we do not present a reaction mechanism involving CO<sub>2</sub> fixation but the utilization of a cyclic carbonate as substrate, which has been produced using the epoxide/CO<sub>2</sub> coupling described in the previous chapter. The reaction is based on the aminolysis of a simple cyclic carbonate to produce N-aryl carbamates in mild conditions using arylamines and catalyzed by 1,5,7-triazabicyclodec-5-ene (TBD), which is an inexpensive organocatalyst.

Chapter 5 is also divided into two parts like Chapter 3, but in this case regarding the mechanism elucidation of polycarbonate formation. Keeping the same format as in Chapter 3, the first part of the chapter is a general investigation on the reaction mechanism of copolymerization of internal

epoxides and CO<sub>2</sub> catalyzed by Al aminotriphenolate complex. The main purpose in this section is to determine how many aluminum complexes are involved in the reaction mechanism and in which form. In the second part of the chapter, a more particular case is studied. The reaction mechanism of the copolymerization of the renewable substrates limonene oxide and CO<sub>2</sub> is elucidated, taking into consideration the stereoselectivity of the process due to the high complexity of limonene oxide, since it has three stereocenters in its structure.

The last chapter that collects results is Chapter 6 where no static DFT based methods are used. Instead, a metadynamic study is presented using multiscale methods (semi-empirical and molecular mechanics) to study the reaction mechanism of racemization of glycidol carbonate, the formation mechanism from glycidol and CO<sub>2</sub> of which is investigated in Chapter 3. By using metadynamics we have been able to include explicitly the solvent and determine its role in the reaction mechanism. Additionally, we studied the decarboxylation of glycidol carbonate, which is the opposite reaction to CO<sub>2</sub> insertion to epoxides. Both reactions are evaluated at different pressures of CO<sub>2</sub> in the system, in order to determine its effect in the activation energy of the reaction.



*"All science is either physics or stamp  
collecting." Ernest Rutherford*

# Chapter 2

## Computational Methods

### 2.1 Quantum Mechanics

Physics (*phusis*) in ancient Greek means *nature* or *natural*. An etymologic interpretation of physics is “knowledge of nature”. Indeed, in our times physics is understood as the scientific discipline that studies how matter behaves. During centuries classical mechanics has been the milestone of physics, enabling the comprehension and explanation of physical phenomena. However, classical mechanics fails at describing the microscopic world at the so-called *quantum realm*, which refers to the size scales where quantum mechanical effects become important. Consequently, in the beginning of XX century, some theories were proposed trying to explain observations that cannot conceal with classical mechanics. Actually, classical mechanics and quantum mechanics are not opposed theories but classical mechanics is just an approximation of

quantum mechanics for large systems (*correspondence principle*). Therefore, the study of a large system within the *classical limit*, gives the same answers through classical or quantum mechanics.

The *quantization* is one of the reasons that makes quantum and classical mechanics to differ. Magnitudes like energy or momentum, among others, have to be restricted to discrete values. A second variation is the *wave-particle duality*, which states that objects have characteristics of both particles and waves. Finally, the precision to determine quantities is limited, as states the *uncertainty principle* postulated by Werner Heisenberg in 1927 (**Eq. 2.1**).

$$\Delta x \Delta p \geq \frac{\hbar}{2} \quad \text{Eq. 2.1}$$

Thus, the more precisely one property is determined, the less precisely the other can be measured. Accordingly, quantum mechanics is limited to calculate a range of probabilities of position and momentum for a given particle. This range of probabilities named *quantum state* is described by the *wavefunction*. The Schrödinger equation describes the evolution in time of the *wavefunction* (**Eq. 2.2**).

$$i\hbar \frac{\partial}{\partial t} \Psi(x, t) = \hat{H} \Psi(x, t) \quad \text{Eq. 2.2}$$

In **Eq. 2.2**  $\hat{H}$  is the Hamiltonian operator that generates the time evolution of quantum states and provides the value for the energy of the system. The  $\hat{H}$  operator is expressed as the sum of two other operators: kinetic and potential operators. If we assume that the Hamiltonian does not contain time, hence the total energy of the system is constant, the space and time dependency of  $\Psi$  can be separated obtaining the time-independent Schrödinger equation (**Eq. 2.3**).

$$\hat{H} \Psi(x) = E \Psi(x) \quad \text{Eq. 2.3}$$

Quantum chemistry aims at solving this time-independent Schrödinger equation using *ab initio* (“from the beginning”) methods. As we know from the lines above,  $\hat{H}$  is the Hamiltonian operator,  $E$  is the total energy of the quantum system that we want to study and  $\Psi$  is the *wavefunction* defined by  $x$  that contains the nuclear and electronic coordinates of the system. The Hamiltonian operator can be split in terms of attraction or repulsion energies: the kinetic energies of the electrons and nuclei, the coulombic attraction of the electrons to the nuclei and the coulombic repulsions between electrons and between nuclei. Considering the Born-Oppenheimer approximation the kinetic energy of nuclei can be neglected respect to the kinetic energy of electrons because nuclei velocities are much lower than electrons due to nuclei mass its much higher than electrons. Moreover, the repulsion between nuclei can be considered constant because the distance between nuclei can be considered constant also. The resultant Schrödinger equation to be solved is showed in **Eq. 2.4**.

$$(T_{el} + V)\Psi_{el}(x, y) = U_n(x)\Psi_{el}(x, y) \quad \text{Eq. 2.4}$$

where  $T_{el}$  stands for the kinetic energy of electrons,  $V$  stands for the sum of coulombic interactions between electrons, nuclei and electrons and nuclei.  $U_n$  is the sum of the electronic and the potential energy of the nuclei for fixed nuclear coordinates. By solving the Schrödinger equation one would obtain  $U_n$  for a set of nuclear coordinates, which actually is the Potential Energy Surface of the system.

Despite the mentioned approximations, the exact solution of this electronic time-independent Schrödinger equation is only possible to be obtained for a one-electron system. For many-electron systems like molecules, which are the systems that we are interested in, it is compulsory to take into account more approximations in addition to Born-Oppenheimer. The reason why we cannot calculate the electron-electron interactions is that we cannot solve a problem of N-electrons as a sum of N one-electron. In order to overcome this limitation, several

methods have been developed. Despite the fact that in this thesis Density Functional Theory (DFT) will be explained below, since has been the theoretical base used to obtain the presented results in this manuscript, it is worth mentioning the importance of Hartree-Fock (HF) method. Most of the so-called post-HF methods are based on corrections or improvements of HF, even DFT-based methods take into account HF exchange for the definition of hybrid functionals, as it will be explained in the corresponding part of this chapter. The *ab initio* methods aim to solve the electronic Schrödinger equation leading to the computation of the wavefunction for a given nuclear coordinates, which is a function of  $3N$  coordinates and  $N$  spin variables, being  $N$  the number of electrons of the system. Therefore, computing the wavefunction for a small organic system of 40 atoms is already highly expensive, not to mention that larger systems with metals like coordination complexes become unaffordable.

## 2.2 Density Functional Theory

There is an alternative to the methods based on the wavefunction. The Density Functional Theory (DFT) is based on the Hohenberg-Kohn theorem,<sup>[36]</sup> which postulates that the ground-state electronic energy and other properties of a molecule are determined by its electron density function  $\rho(\vec{r})$  that depends only on three spatial coordinates, independently of the number of electrons of the studied system, thus simplifying considerably the mathematical problem (see **Eq. 2.5**).

$$\rho(\vec{r}) = N \int \dots \int |\psi(\vec{x}_1, \vec{x}_2, \dots, \vec{x}_n)|^2 ds_1 d\vec{x}_2 \dots d\vec{x}_N \quad \text{Eq. 2.5}$$

As it can be seen in **Eq. 2.5**, the electron density function is defined as the multiple integral over the spin variables of all the electrons and over all but one of the spatial coordinates. The electronic energy is expressed as:

$$E_0 = E[\rho_0] = \int \rho_0(\vec{r})V_{ne}(\vec{r})d\vec{r} + F[\rho_0(\vec{r})] \quad \text{Eq. 2.6}$$

where  $V_{ne}(\vec{r})$  is the potential energy obtained from the nucleus-electron interaction and  $F[\rho_0(\vec{r})]$  is the functional of the electron density. The first Hohenberg-Kohn theorem states the relation between a functional and the energy of the system (*existence theorem*), but does not describe how to find this functional. The functional of the electron density can be expressed as a sum of several independent terms showed in **Eq. 2.7**.

$$F[\rho_0(\vec{r})] = T_s[\rho_0(\vec{r})] + J[\rho_0(\vec{r})] + E_{Ne}[\rho_0(\vec{r})] + E_{XC}[\rho_0(\vec{r})] \quad \text{Eq. 2.6}$$

In **Eq. 2.6**,  $T_s[\rho_0(\vec{r})]$  is the kinetic energy of the non-interacting electrons,  $J[\rho_0(\vec{r})]$  is the classical Coulomb electron-electron repulsion,  $E_{Ne}[\rho_0(\vec{r})]$  is the electron-nucleus interaction and  $E_{XC}[\rho_0(\vec{r})]$  is the exchange-correlation energy, which is the unknown term that includes the kinetic energy of the interacting electrons, the exchange energy and the correlation energy. In order to describe this exchange-correlation energy in the most accurate way, many approximations have been proposed, leading to the wide variety of DFT functionals available nowadays in the literature.

Kohn and Sham in 1965 developed the first method to calculate the electronic state using the theoretical basis of the Hohenberg-Kohn theorems.<sup>[37]</sup> Their basic idea was to obtain from a single Slater determinant the exact kinetic energy of a non-interacting reference system that has the same electronic density as the studied system. A Slater determinant is an antisymmetrized product of N one-electron wavefunctions. This determinant contains the one-electron wavefunctions in the columns and the electron coordinates are collected

along the rows. Furthermore, the system of non-interacting N-electrons can be described as the summation of one-electron Hamiltonians. The resulting equation is showed in **Eq. 2.7**.

$$h_i^{KS} \varphi_i^{KS} = \varepsilon_i \varphi_i^{KS} \quad \text{Eq. 2.7}$$

In **Eq. 2.7**,  $h_i^{KS}$  is the one-electron Kohn-Sham Hamiltonian,  $\varphi_i^{KS}$  represents the KS spin-orbitals and  $\varepsilon_i$  is the KS orbital energy. Regrouping the non-interacting term and building the electronic density from a set of orbitals allowed to use the DFT for calculations of real systems. Due to the Hamiltonian depends on the electronic density, a trial electronic density function is considered as initial guess. Therefore, in order to solve **Eq. 2.7**, an iterative self-consistent approach (SCF) is considered, similar to the used in the Hartree-Fock method (see **Figure 2.1**).

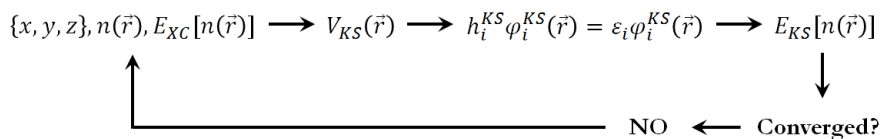


**Figure 2.1** Kohn-Sham iterative flow chart to calculate the KS energy.

The second theorem postulated by Hohenberg and Kohn states that the electronic density obeys a variation principle. Therefore, they state that any electronic density function will give an energy higher (or equal) to the exact ground-state energy. Consequently, using the HK theorems and KS method a wide variety of functionals have been designed to find the closest energy to the exact one for the studied system. In particular, the efforts have been focused on describing the exchange-correlation energy, which is the unknown part of **Eq. 2.6**. John P. Perdew proposed in 2009 a schematic way to organize the so-called “soup of functionals”. The DFT Jacob’s ladder connects the “Hartree world” with the “Heaven of Chemical Accuracy”. Below I briefly describe the simplest approximation to calculate  $E_{XC}[\rho_0(\vec{r})]$  followed by more complex approximations that

constitute the families of functionals available nowadays. Special emphasis will be put on the functionals used in this Thesis.

### 2.2.1 Functionals of the electron density

The simplest approach is the Local Density Approximation (LDA), which assumes that the density can be treated locally as a uniform electron gas. The exchange part is obtained from the Thomas-Fermi-Dirac method and the correlation term from highly accurate Monte-Carlo simulations of the uniform electron gas. Despite this method describes solids rather well, fails in situations where the electronic density changes rapidly. An example of this situation are molecules, which is the case that we are interested in. Therefore, we should move forward to a more complex description of the electronic density.

The Generalized Gradient Approximation (GGA) does not depend solely on the electronic density but on its gradient, both in the exchange and correlation functionals (see **Eq. 2.8**).

$$E_{XC}^{GGA}[\rho] = \int \rho(\vec{r}) \varepsilon_{XC}[\rho(\vec{r}), \nabla\rho(\vec{r})] dr \quad \text{Eq. 2.8}$$

There are two possible approaches regarding the development of GGA exchange functionals. On one hand, some functionals like B or B88 developed by Becke,<sup>[38]</sup> are based on parameters obtained from high-accurate quantum calculations or experimental data. On the other hand, other functionals like PBE developed by Perdew are designed from quantum mechanical principles.<sup>[39]</sup> The correlation part is calculated from analytical equations. Some relevant examples are P86<sup>[39]</sup> or LYP<sup>[40]</sup> functionals. The combination of exchange and correlation functionals lead to the highly popular functionals used nowadays in computational chemistry like BP86, BLYP or PBEPBE.

In all the DFT-based studies collected in Chapters 3, 4 and 5 of this Thesis, we use B97-D3 functional. The B97D functional is a semiempirical GGA-type based on Becke's that was developed by Stefan

Grimme in 2006.<sup>[41]</sup> A new damping function of the dispersion correction (see next section for dispersion corrections) was proposed also by Grimme in 2010, constituting the new series of D3-BJ dispersion corrections.<sup>[42]</sup>

The next generation of electron density functional approximations are the Meta Generalized Gradient Approximation (m-GGA), which do not only account the derivative of the density but the second derivative (Laplacian,  $\nabla^2$ ). This type of functionals were not used in this Thesis because their minor improvement of the accuracy in the studied systems did not compensate their higher computational cost in comparison to GGA functionals.

The exchange part of the exchange-correlation energy may be obtained from HF theory. Actually, the combination of GGA methods with a certain percentage of HF exchange lead to significant improvements in terms of accuracy in real chemical systems. These type of functionals are the so-called Hybrid-GGA (H-GGA). The most popular example of this type of functionals is the well-known B3LYP functional, obtained from the combination of B88 exchange and LYP correlation functionals.<sup>[40, 43]</sup> In addition to B88 and LYP, three parameters are included in the equation of the exchange-correlation energy (see **Eq. 2.9**), which one of them is the amount of HF exchange (20%) and the other two are the weight of LDA exchange-correlation and GGA exchange-correlation (B88-LYP).

$$E_{XC}^{B3LYP} = (1 - a)E_X^{LDA} + aE_X^{HF} + bE_X^{B88} + (1 - c)E_C^{LDA} + cE_C^{LYP} \text{ Eq. 2.9}$$

The B3LYP functional is used in Chapter 3 of this Thesis, as well as  $\omega$ B97XD, which is a long-range corrected hybrid functional developed by Head-Gordon<sup>[44]</sup> that we employed in the calculations reported in Chapters 3 and 5 of this Thesis.

There is still another family of DFT functionals based on the combination of m-GGA and H-GGA, which are the so-called meta-hybrid GGA functionals, which use the first and second derivative of the density and



also a certain contribution of HF exchange. The most popular example of these functionals are the Minnesota suite of functionals (M06, M06-L, M06-2X and M06-HF, depending on the HF contribution to the exchange energy). In this Thesis we used M06-2X (57% of HF exchange) in Chapters 3 and 6.<sup>[45]</sup>

### 2.2.2 Including dispersion interactions into DFT calculations

The applicability of DFT based methods in elucidating chemical reaction mechanisms and other important parameters of reactivity is far from any doubt. Nowadays, DFT is the most widely used theoretical approach due to its high accuracy and low computational cost. Actually, the description of short-range interactions like chemical bonds are usually well described by the exchange-correlation effects accounted in DFT functionals. However, the medium-range and long-range interactions like van der Waals interactions or hydrogen bonds are not properly described in some cases. This limitation becomes relevant when weak interactions, also named dispersion interactions, play a crucial role in the chemical system aimed to study, which is the case of this Thesis. In order to overcome this problem, Truhlar and Grimme postulated two different methods. In this Thesis, we mainly used the second approach reported by Grimme but we briefly describe Truhlar's methodology down below.

The M06 functionals created by Truhlar et al. have shown high correlation between experimental data and calculations. Indeed, these functionals are extensively used nowadays to computationally study a wide variety of chemical systems.<sup>[45-46]</sup> The M06 functionals are developed fitting their parameters to experimental data, hence including implicitly the contribution of dispersion interactions.

Alternatively, Grimme included the dispersion interactions into DFT explicitly adding an energy term  $E_D$  to the calculated DFT energy (see **Eq. 2.10**).<sup>[47]</sup>

$$E_{DFT-D} = E_{DFT-KS} + E_D \quad \text{Eq. 2.10}$$

The mathematical expression of  $E_D$  is depicted in **Eq. 2.11**, where  $S_6$  is a scaling factor that depends on the functional used,  $N$  is the number of atoms and  $C_6^{ij}$  is the dispersion coefficient for the two atoms  $ij$ , which are separated by  $R_{ij}$ . The dispersion coefficient depends on the van der Waals radii of the atom. The last term  $f_{dmp}$  is a damping function (see **Eq. 2.12**) that rapidly decays at small  $R_{ij}$ , hence the regular bonds are not included in  $E_D$ .

$$E_D = -S_6 \sum_{i=1}^{N-1} \sum_{j=i+1}^N \frac{C_6^{ij}}{R_{ij}^6} f_{dmp}(R_{ij}) \quad \text{Eq. 2.11}$$

$$f_{dmp}(R) = \frac{1}{1+e^{-\alpha(\frac{R}{R_0}-1)}} \quad \text{Eq. 2.12}$$

In 2010, Grimme et al. reported a new refined methodology to account dispersion interactions into DFT functionals.<sup>[48]</sup> This new approach named DFT-D3, after DFT-D2 published at 2006,<sup>[49]</sup> is an improved method that includes an additional term  $S_n$  ( $n = 6, 8$ ), as it can be seen in **Eq. 2.13**. The related damping function is showed in **Eq. 2.14** below.

$$E_{D3} = \sum_{n=6,8} S_n \sum_{i,j>1}^N \frac{C^{ij}}{R_{ij}^n} f_{dmp}(R_{ij}) \quad \text{Eq. 2.13}$$

$$f_{dmp}(R) = \frac{1}{1+6\left(\frac{R_{ij}}{s_{r,n}R_0^{ij}}\right)^{-\alpha n}} \quad \text{Eq. 2.14}$$

Recently, Grimme and coworkers reported a new damping function for the DFT-D3 named D3BJ (see **Eq. 2.15** and **Eq. 2.16**).<sup>[42]</sup>

$$E_{D3BJ} = \sum_{n=6,8} S_n \sum_{i,j>1}^N \frac{C^{ij}}{R_{ij}^n + (f_{dmp})^n} \quad \text{Eq. 2.15}$$

$$f_{dmp}(R) = \alpha_1 \sqrt{\frac{C_8^{ij}}{C_8^{ij}}} + \alpha_2 \quad \text{Eq. 2.16}$$

In this Thesis, both D3 and D3BJ corrections have been used, since are included in the  $\omega$ B97XD and B97-D3 functionals, respectively. In Chapter 3 and 6, we also used M06-2X that accounts the dispersion interactions implicitly.

## 2.3 Solvation Models

Solvation is crucial in the kinetics of many chemical reactions. Actually, only changing the polarity of the solvent, the obtained product may change due to the enhancement or undermining of an alternative mechanistic pathway. Therefore, accounting the solvent in an accurate manner is crucial in order to describe chemical reactivity, especially in homogeneous catalysis. There are two methodologies to include solvation effects in computational chemistry. The first one is by including explicitly a certain amount of molecules of the solvent in the calculation. This method allows us to describe the solute-solvent interaction, which may be determinant in some cases. However, adding enough solvent molecules to the system to mimic the real concentration of solute into the solvent it is unaffordable when using DFT based methods because the system becomes too large. The second approach, which is the implicit solvation model, is usually considered in the DFT calculations where solvation has to be included. The implicit solvation model is based in the formation of a cavity in a continuum medium that its dielectric constant is the same that of the solvent. The solute is placed into the cavity, which its shape is based on the solute structure. Then, the dielectric medium produces an electrostatic interaction with the solute and *vice versa*. This process takes place iteratively until the mutual polarization reaches the self-consistency (Self-Consistent Reaction Field, SCRF).<sup>[50]</sup>

The mathematical expression to calculate the solvation Gibbs free-energy when SCRF method is used is showed in **Eq. 2.17**,

$$\Delta G_{solv} = \Delta G_{cav} + \Delta G_{disp} + \Delta G_{rep} + \Delta G_{el} \quad \text{Eq. 2.17}$$

where  $\Delta G_{cav}$  is the energy required to create the cavity for the solute and  $\Delta G_{disp}$  is the energy related to the exergonic interaction between the solute and the solvent. Contrarily, the  $\Delta G_{rep}$  term is the repulsive energy between the solute and the solvent. Finally,  $\Delta G_{el}$  is a stabilizing term that corresponds to the electrostatic interactions of the solute molecules in the solvent and *vice versa*.

In this Thesis we use two different continuum models. On one hand, the traditional Polarized Continuum Model (PCM).<sup>[51]</sup> On the other hand, the Solvation Model based on Density (SMD).<sup>[52]</sup> The PCM model is based on the Poisson-Boltzmann equation, while SMD is based on the generalized Born equation, which is an approximation of Poisson's equation for cavity shapes. Therefore, both models are rather similar. The major difference between them is SMD uses a set of specifically parametrized radii to create the cavity.

## 2.4 Translational Entropy Corrections

The ideal gas model is considered in the DFT calculations to obtain the molecular partition functions (see **Eq. 2.18**). Therefore, the equations used in the electronic calculations are based on a hypothetical ideal gas, where the concentrations are equivalent to standard state ( $P = 1 \text{ atm}$ ). This presents an important limitation when a considerable change of entropy takes place in solution.

$$q_{trans} = \left(\frac{2\pi mRT}{h^2}\right)^{3/2} \frac{RT}{P} \quad \text{Eq. 2.18}$$

Actually, in the systems studied in this Thesis we may observe the formation of one entity from four independent bodies, thus implying a strong entropy penalty.<sup>[53]</sup> In order to overcome this limitation, several corrections have been reported to adjust the translational entropy in solution to a more realistic situation.

We have evaluated three different methods in a specific system in Chapter 3, although we use a specific correction proposed by Martin in almost all the DFT calculations reported in this Thesis.

The simplest approach was reported by Morokuma et al.<sup>[34a]</sup> They propose to neglect the translational entropy term in solution. Thus only accounting the electronic, vibrational and rotational entropy in the system.

The second approach is postulated by Wertz<sup>[54]</sup> and Ziegler<sup>[55]</sup> in 1980 and 2002, respectively. This approach is separated into three parts. In the first part of this method, the solute considered as an ideal gas is compressed from standard conditions to the standard volume of the solvent. Then, the compressed solute is transferred to the solvent. The resulting solution presents the intermolecular interactions of a dilute solution. In this step, the entropy lost by the solute is the same as the solvent would lose going from gas to liquid. This entropy loss labeled as  $\alpha$  is calculated by using **Eq. 2.19**.

$$\alpha = \frac{S_{liq}^0 - (S_{gas}^0 + R \ln \frac{V_{m,liq}}{V_{m,gas}})}{S_{gas}^0 + R \ln \frac{V_{m,liq}}{V_{m,gas}}} \quad \text{Eq. 2.19}$$

As it can be seen in **Eq. 2.19**, the entropy loss can be determined from the absolute entropies of the solvent in its gas ( $S_{gas}^0$ ) and liquid ( $S_{liq}^0$ ) phases.

In the third part of the process the solute is expanded again to the concentration of the desired solution. The change of entropy of the solute related to the first and third steps can be calculated by **Eq. 2.20**, where

$V_{m,f}$  is the final solute molar volume and  $V_{m,i}$  is the initial solute molar volume.

$$\Delta S = R \ln\left(\frac{V_{m,f}}{V_{m,i}}\right) \quad \text{Eq. 2.19}$$

Considering the entropy loss of the second part  $\alpha$ , and the entropy difference of the first and third steps, we can calculate the entropy of solvation using **Eq. 2.20** showed below.

$$\Delta S_{solv} = R \ln \frac{V_{m,liq}}{V_{m,gas}} - \alpha \left( S_{gas} - R \ln \frac{V_{m,liq}}{V_{m,gas}} \right) + R \ln \frac{V_m^0}{V_{m,gas}} \quad \text{Eq. 2.20}$$

The last approximation proposed by Martin and coworkers in 1998<sup>[56]</sup> determines the applicable pressure ( $P = n/V RT$ ) at the concentration of the solvent from its experimental density. Then, the higher is the density of the solvent, the higher is the pressure applied at the system to model the solvation.

Taking liquid water as example, which has a density of  $\rho = 997.02 \text{ kg}\cdot\text{m}^{-3}$ , requires a pressure of 1354 atm to correct the aqueous solution concentration. The actual concentration (1354 atm/ $RT$ ) is incorporated to the calculation of the translational partition function in **Eq. 2.18**. This approximation is used for adjusting the solvent concentration of the gas-phase entropy in the whole Thesis.

## 2.5 Adaptive QM/MM Metadynamics Simulations

### 2.5.1 Metadynamics

The study of reaction mechanisms using static standard DFT methods presents several limitations regarding the effect of solvation, or accounting thermodynamic parameters like pressure or temperature. These limitations can be overcome using alternative theoretical

methodologies. One of these alternative methods is metadynamics, which in recent years have increased its popularity due to its flexibility and efficiency gathering information of the studied system. Metadynamics is a method proposed by Alessandro Laio and Michele Parrinello in 2002<sup>[57]</sup> that has been applied mainly in three different fields: solid-state physics,<sup>[58]</sup> biomolecules<sup>[59]</sup> and chemical reactions.<sup>[60]</sup> In our case, we focused on the latter case.

Metadynamics simulations is a modification of molecular dynamics, which has become a standard tool not only in chemistry, but in many areas of science. By using molecular dynamics, we can understand complex processes like protein folding or the interaction between molecules (*ligand docking*). However, molecular dynamics is not an appropriate method to study processes where two states are separated by a high free-energy barrier. Actually, we need long simulations to visit all the energetically relevant configurations, which makes computationally unfeasible to study such situations. For example, the isomerization between two conformations of a molecule could have a high energetic barrier, so would be difficult to observe the isomerization. Another case are chemical reactions, which is the field that we are interested in.<sup>[61]</sup> Additionally, in chemical reactions bonds are formed and broken, hence cannot be studied properly by Molecular Mechanics, which is the methodology usually used in conformational studies. We will address this limitation in the next section of this chapter.

Regarding the unfeasibility of studying slow processes using molecular dynamics, several enhanced sampling techniques have been reported in recent years. Such techniques allow us to consider not the whole period of time that the studied process needs, but a representative period of such event. An example of this methodology is umbrella sampling, suggested by Torrie and Valleau in 1977,<sup>[62]</sup> which considers several states of the chemical process that are related to the consequent periods of time of the reaction. By preventing the evolution of these states towards the next or the previous ones, we can evaluate independently all these representative

states of the process. In our case, metadynamics facilitates the sampling of the process by the introduction of a biased force that is applied to a selected number of degrees of freedom called collective variables (CVs). Metadynamics is able to reconstruct the free-energy surface at the same time it enhances sampling towards the selected CVs.<sup>[63]</sup> Thus, is a powerful technique to obtain a lot of information from the studied system.

The history-dependent external force (or potential) used in metadynamics to bias the system is a function of the CVs. This force that can be expressed as a sum of Gaussian functions is added to the Hamiltonian ( $\hat{H}$ ) of the system. These Gaussians are deposited along the system trajectory in the space of the selected CVs to prevent the system from going back to already visited configurations that have already been sampled.

In order to understand how this technique works, we can imagine a situation where someone is located inside a swimming pool of unknown shape and depth. This subject has its eyes covered and the only way to escape from the pool is placing bags of sand along the 3D surface of the swimming pool and climbing them. By counting the bags of sand and knowing its size, the shape and depth of the swimming pool can be determined. The narrower and shallower the bags, the better prediction would be done, but also, more bags have to be placed to map the surface.

In the reality, when metadynamics is applied to chemistry, the bags of sand of the imaginary example are Gaussian functions. The height of these functions determine the height of the free-energy barrier, while the width of the functions allow us to describe the shape of the surface. As always, we have to reach a compromise between accuracy and computational time. If we use too small functions, we would never scape from the minima. Nevertheless, choosing the size of the Gaussian functions is not the most complex part of metadynamics.

As I mentioned before, we have to choose a set of degrees of freedom (CVs) that will be biased by an external force. These CVs are crucial to



reach the desired product because if inappropriate CVs are chosen one would obtain a different product or would follow a pathway higher in energy than the most suitable, thus describing erroneously the reaction pathway. We explain in Chapter 6 of this Thesis, how to choose the correct CVs and how to validate them.

## 2.5.2 Adaptive multiscale methods

In the previous section we already pointed out the two main inconveniences of using molecular dynamics to study chemical reactions. On one hand, the need of populating the convenient energy states towards the product of the reaction. This limitation is overcome by sampling methods like metadynamics. On the other hand, the bond forming and bond breaking processes cannot be properly described by using molecular mechanics. Moreover, we cannot afford the description of the whole system by QM methods because we are including explicit solvent and we need to run a significant amount of simulation time.

In recent years, multiscale methods have become a popular approach to solve this dilemma. In the hypothetical case of studying a catalyzed chemical reaction, we have to describe by QM methods the section of the system where the reaction takes place. For example, the catalyst, substrates and the first sphere of solvation may be involved in the reaction mechanism, which would be the molecules described by QM methods. Consequently, we would compute the rest of the system (environment), which is usually the solvent, using molecular mechanics.

The QM/MM approach was first introduced by Warshel and Levitt in 1976,<sup>[64]</sup> which earned them the 2013 Nobel Prize in Chemistry together with Martin Karplus. The energy computed by QM/MM methods is defined by **Eq. 2.21**:

$$E_{Total}^{QM/MM} = E_{Act}^{QM} + E_{Env}^{MM} + E_{Act/Env}^{QM/MM} \quad \text{Eq. 2.21}$$

where  $E_{Act}^{QM}$  is the energy of the active section computed at the QM level,  $E_{Env}^{MM}$  is the energy of the environment computed at the MM level and  $E_{AS/ES}^{QM/MM}$  is the energy related to the interaction between the two sections. There are many methods to calculate this latter term. Actually, treating the charge near the boundary between regions is not straightforward. Depending on the treatment of the electrostatic interaction between the *Act* and *Env*, the QM/MM methods can be separated into two groups: mechanical or electric embedding. Mechanical embedding treats the interactions between the *Act* and *Env* at the MM level. The Integrated Molecular-Orbital Molecular-Mechanics (IMOMM) scheme reported by Morokuma and Maseras,<sup>[65]</sup> which is the method that we considered in this Thesis, is a mechanical embedding scheme.

As we mentioned before, in some cases we may need to describe not only the catalyst and substrates at the QM level, but also the first sphere of solvation of these molecules. Actually, if we want to study the role of the solvent in the reaction mechanism, which is one of the limitations of static DFT methods, we have to compute the solvent around the active site at the QM level. Considering a static calculation there is no problem, but when we run a dynamic simulation the diffusive nature of the solvent causes that the molecules considered in the first sphere of solvation of the active site move away from the substrate and catalyst, replacing those for other solvent molecules considered at the MM level. In order to solve this problem, adaptive QM/MM methods have been proposed where instead of choosing discrete molecules to be treated at the QM level, a continuum volume around the active site is set. Thus, we define a sphere of a certain diameter where all molecules within this region are described QM and the molecules outside this region are computed at MM level. Bulo and coworkers reported in 2009<sup>[66]</sup> an efficient and accurate adaptive multiscale molecular dynamics method that enable the detailed study of large molecular systems. In Chapter 6 of this Thesis we used FlexMD, which is the program developed by Bulo et al.,<sup>[67]</sup> to study two different reactions in solvent mimicking the experimental conditions.

*"The proper use of science is not to  
conquer nature but to live in it."*

*Barry Commoner*

# Chapter 3

## Cyclic Carbonates

### 3.1 Introduction

One of the main challenges that scientific community is facing in 21<sup>st</sup> century is global warming.<sup>[4-6, 12, 68]</sup> The problematic depends on two correlated factors, being the dependence on pollutant and limited fossil fuels (coal, oil, and natural gas) and the high concentration of greenhouse gases in the atmosphere. The most abundant and problematic greenhouse gas is carbon dioxide (CO<sub>2</sub>) mainly produced as sub-product of many industrial processes like combustion of fossil fuels or large scale oxidation processes.<sup>[7-8, 69]</sup> Therefore, the capture and utilization of CO<sub>2</sub> from industrial processes is a straightforward solution to mitigate greenhouse gases emission and consequently, climate change,<sup>[10a, 10c, 16, 22, 70]</sup> while at the same time presents interesting economic opportunities.<sup>[11]</sup>

The synthesis of cyclic carbonates is one of the most popular and widely investigated catalytic strategies to chemically fixate CO<sub>2</sub>.<sup>[71]</sup> Cyclic carbonates (CyCs) are valuable intermediates for many chemical reactions in the pharmaceutical industry or as raw materials for polymers.

Alternatively, CyCs are also used as polar aprotic solvents<sup>[72]</sup> or as high permittivity component of electrolytes in lithium batteries.

The obsolete industrial synthetic route to obtain CyCs used phosgene, which produces hydrogen chloride as waste.<sup>[73]</sup> Considering instead the catalyzed reaction of epoxides with CO<sub>2</sub> no waste is generated and CO<sub>2</sub> is chemically stored into the product. Epoxides are ideal substrates for this reaction due to its high internal energy that compensate the high thermodynamic stability of CO<sub>2</sub>. The activation of CO<sub>2</sub> is an energetically demanding process due to its kinetic stability, thus a catalyst is required to speed-up the process.

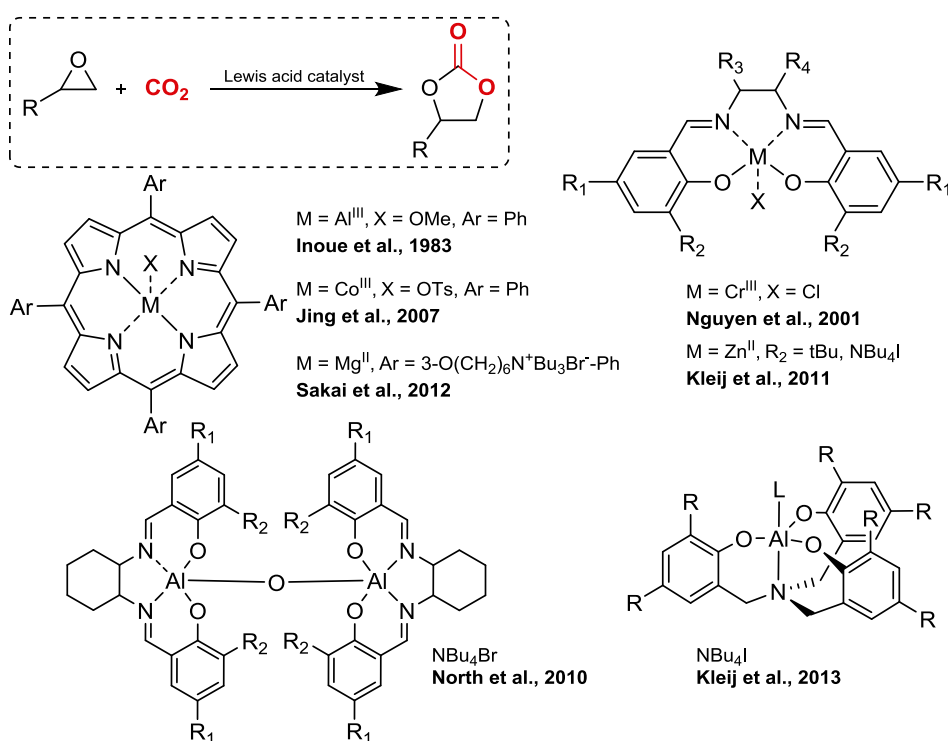


**Figure 3.1** Several reported catalysts for the formation of cyclic carbonates from oxiranes using CO<sub>2</sub> as carbon feedstock.

Several types of catalysts have been considered for this purpose, such as ionic liquids,<sup>[74]</sup> nanoparticles,<sup>[75]</sup> alkali metal halides,<sup>[76]</sup> quaternary

ammonium salts,<sup>[77]</sup> organocatalysts,<sup>[78]</sup> transition metal complexes<sup>[24a, 26b, 71c, 79]</sup> or aluminum and magnesium coordination complexes.<sup>[27b, 28b, 71a, b, 80]</sup>

The first catalytic system being able to trap CO<sub>2</sub> and transform it to CyC was the metalloporphyrin (TPP)AlOMe complex (see **Figure 3.1**) reported by Inoue and co-workers in 1983.<sup>[29a]</sup> In later years several metalloporphyrin catalysts were reported improving the activity of (TPP)AlOMe, like a cobalt based catalyst reported by Jing et al. in 2007.<sup>[81]</sup> More recently in 2012, Sakai and coworkers proposed a highly active bifunctional magnesium-porphyrin complex<sup>[82]</sup> that combines in the same complex an organocatalytic group (Ph-NBu<sub>3</sub>Br) and the metal ion (Mg<sup>II</sup>) acting as Lewis acid. This binary catalytic system reported high turnover number (TON = 103,000) under neat conditions. Alternatively, Nguyen and coworkers reported in 2001 an active and commercially available Cr(III)-salen complex to obtain CyC under mild temperatures and pressures.<sup>[83]</sup>

The evolution of salen ligand to salphen by placing an aromatic ring in the N-bridge (R<sub>3</sub>, R<sub>4</sub> in **Figure 3.1**) proposed by Kleij et al. (2011) allowed the utilization of non-pressurized CO<sub>2</sub> to efficiently produce CyC.<sup>[79a]</sup> In the same direction, North and coworkers reported a dimeric Al(salen) complex able to undergo CyC at room temperature and 1 bar of CO<sub>2</sub>.<sup>[71b]</sup>

The catalytic system studied in this thesis depicted in **Figure 3.2** was reported by Kleij et al. in 2013,<sup>[33a]</sup> which is constituted by an Al aminotriphenolate complex [**Al<sup>R</sup>**] acting as Lewis acid and a nitrogen based nucleophile named tetrabutylammonium iodide (NBu<sub>4</sub>I). The aromatic substituents in *ortho* and *para* positions of the ligand change the activity and chemoselectivity of the ligand, leading to dimerization (n=2) when protons or tert-butyls and nitro groups are considered. The remarkably catalytic activity presented by this binary system exceeded TONs of 100,000 with TOFs as high as 36,000 h<sup>-1</sup>.

In this chapter we present our results regarding mechanistic aspects of the catalyzed reaction of CO<sub>2</sub> and epoxides to produce cyclic carbonates.

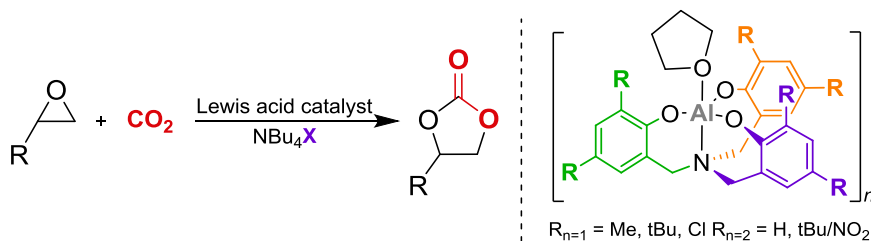


**Figure 3.2** Schematic representation of the reaction and the catalytic system. Several aromatic substituents can be considered in the orto/para positions of the ligand, which can lead to the dimerization of the Al complex.

In the first part, we will consider a quantitative approach to analyze the main factors that influence the Gibbs free-energy values obtained computationally, hence aiming to improve the accuracy of our calculations for this system or similar. In the second part we will consider a functionalized epoxide that may present different reactivity towards CO<sub>2</sub> fixation. Our computational results will be presented in parallel with the experimental data provided by Kleij and coworkers.

### 3.1.1 Previous Mechanistic Studies

The rapid development of catalytically active coordination complexes to transform CO<sub>2</sub> to CyC lead to many questions regarding the mechanistic insights of the process. Due to the kinetic stability of CO<sub>2</sub>, the knowledge on the reaction mechanism becomes crucial to improve the catalytic efficiency of the system. Moreover, modern and efficient DFT-based methods enable us to compute entire catalytic systems with reasonable accuracy and affordable times. Consequently, a number of mechanistic proposals for several catalytic routes have been reported in the recent years.<sup>[24a, 27b, 76, 78a, 84]</sup>

It is worth mentioning the work of North and coworkers in the detailed study of the catalyzed reaction mechanism using the Al(salen)-O-Al(salen)/Bu<sub>4</sub>NX binary catalyst system.<sup>[71a]</sup>

In our group we studied in detail the reaction mechanism catalyzed by the Zn(salphen) and the Al aminotriphenolate complex in collaboration with

Kleij's group.<sup>[79b, 80d]</sup> The proposed mechanism by our group is similar for both Zn and Al catalytic systems, hence a single scheme considering  $[Al^R]$  is depicted in **Figure 3.3**.

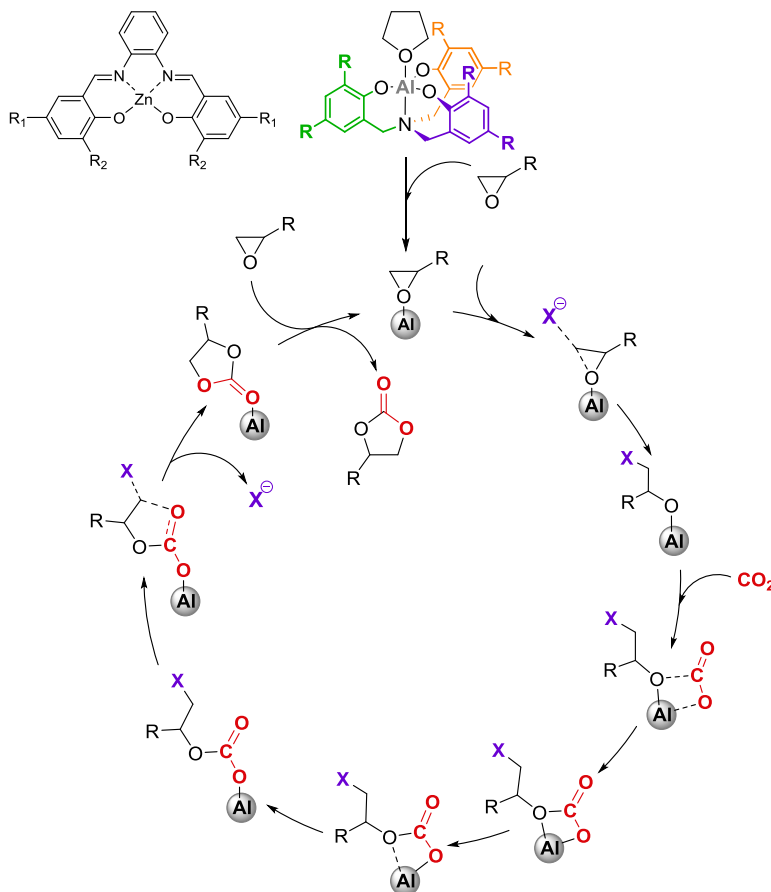


**Figure 3.3** Catalytic cycle for the ring-expansion addition of CO<sub>2</sub> to epoxides catalyzed by Zn(salphen) or Al aminotriphenolate complexes and co-catalyzed by a generic halide (X<sup>-</sup>). All intermediates and transition states are illustrated.

The reaction mechanism starts with the coordination of the epoxide to the axial position of the catalytic complex (after decooordination of THF in the Al case). This intermediate constitutes the most stable assembly of the entire mechanism, therefore is the resting state of the reaction. The nucleophilic attack of a halide to open the epoxide is a fast process

because the high reactivity of the substrates and the stabilization of the formed alkoxide by the metal. Noteworthy, the major oxophilicity of aluminum leads to major stabilization of the formed alkoxide in comparison with zinc complex. After alkoxide formation, CO<sub>2</sub> is activated through the nucleophilic interaction with the alkoxide. Additionally, the resulting chelating fashion carbonate is stabilized by the coordination of one oxygen of the CO<sub>2</sub> moiety to the metal center conforming a stable octahedral geometry. Via an isomerization process, the chelate carbonate evolves to a linear hemi-carbonate that presents a more suitable conformation to facilitate the nucleophilic ring-closing step where the carbonyl oxygen expulses the halide generating the CyC coordinated to the metal center by the carbonyl oxygen of the product. The reaction of CO<sub>2</sub> with epoxides to obtain CyC is not a high exergonic process due to the high thermodynamic stability of CO<sub>2</sub>, hence a high internal energy substrate like epoxides is required to compensate this important inconvenient.

## 3.2 Quantitative Evaluation of the Catalytic Activity

### 3.2.1 Goals and Motivation

As we introduced in the previous section, the reaction of CO<sub>2</sub> with epoxides to produce cyclic carbonates has been widely investigated. However, only in some cases the used catalytic systems present high activity indicated by high turnover frequencies (TOFs). Kleij and coworkers have shown that Al aminotriphenolate complex [Al<sup>R</sup>] combined with NBu<sub>4</sub>I (TBAI), form an efficient binary catalyst for the coupling of CO<sub>2</sub> with epoxides accounting high activity with TOFs up to 36,000 h<sup>-1</sup> using a wide scope of substrates.

In addition to the interest of this reaction because its relevance in terms of sustainability, the multicomponent nature of the reaction provides the opportunity to explore the contribution of the translational entropy in the



Gibbs free-energy reaction profile. Note that the chemical process we aim to study implies a reactive event in which four bodies must encounter. This implies a strong entropy penalty, which is not properly accounted when considering the ideal gas equations model.

Thus, we investigated the mechanism for the formation of cyclic carbonates from CO<sub>2</sub> and 1,2-epoxyhexane catalyzed by an Al complex/NBu<sub>4</sub>I binary system. The outcome of this catalytic cycle is examined in terms of the energetic span model ( $\delta E$ ) developed by Kozuch and Shaik.<sup>[85]</sup> We considered all the factors that affect the Gibbs free-energy and consequently the TOF: the solvation model, the changes in entropies in solution, and the use of hybrid, meta-hybrid and dispersion-corrected DFT functionals. We analyzed in detail how the different terms affected the Gibbs free-energy barriers and TOFs. This analysis provides a guideline to identify those factors really relevant to obtain quantitative results.

### 3.2.2 Computational Details

All calculations in this study were performed by using the Gaussian 09 package.<sup>[86]</sup> The hybrid B3LYP functional,<sup>[40, 43]</sup>  $\omega$ B97XD<sup>[44]</sup> and B97-D3<sup>[87]</sup> dispersion-corrected functionals and the parametrized with implicit dispersion corrections M06-2X<sup>[88]</sup> functional were employed. The Pople 6-311G(d,p) basis set<sup>[89]</sup> was used to describe H, C, N and O atoms. The LANL2DZ<sup>[90]</sup> basis set and the associated relativistic effective core pseudopotential were used for Al, Cl, and I atoms. Full geometry optimizations were performed without constraints. All stationary points were characterized either as minima or transition state by means of harmonic vibrational frequencies analysis. Gibbs free-energies were initially calculated at standard conditions (T=298.15 K, P=1 atm).

Solvent effects were accounted for gas-phase optimized structures by using the polarizable continuum model (PCM). Also, optimized geometries in gas phase were re-optimized using the SMD solvation model. The reaction takes place in neat condition, hence the solvent of

the reaction is the 1,2-epoxyhexane itself. The dielectric constant ( $\epsilon$ ) of the simplest epoxide, ethylene oxide, is  $\epsilon=12.42$ ,<sup>[91]</sup> hence we choose the parameters for 1-hexanol solvent ( $\epsilon=12.51$ ), as implemented in the Gaussian09 package.

Many authors have suggested that translation entropies computed *in the gas phase* must be corrected when they are applied to reactions in solution. Note that solvation free-energies do not account for the loss of molar entropy of a liquid with respect to a gas. Since there is no well-defined standard approach to evaluate entropies in solution accurately, we applied here three approaches from literature: i) neglecting the translational-entropy terms in the calculation of the entropy in solution,<sup>[34a]</sup> ii) the approach proposed by Martin and coworkers,<sup>[56]</sup> and iii) the method described by Wertz<sup>[54]</sup> and used by Cooper and Ziegler<sup>[55, 92]</sup> that is based on a ratio related to the molar entropy lost by the solvent. The Turnover Frequency (TOF) values were calculated at 363.15 K (90°C) by applying the equations of the energetic span model as implemented in the user-friendly AUTOF program.<sup>[85, 93]</sup> In the energetic span model defined by Kozuch et al. the entire Gibbs free-energy profile, thus all the intermediates and transition states in the reaction pathway, are accounted in the TOF calculation. This approach is not equivalent to Eyring's equation, which only considers the absolute Gibbs free-energy barrier.

### 3.2.3 Results and Discussion

#### 3.2.3.a Reaction mechanism of cyclic carbonate formation from CO<sub>2</sub> and 1,2-epoxyhexane

The reaction mechanism of the formation of cyclic carbonates from CO<sub>2</sub> and terminal epoxides catalyzed by the Al aminotriphenolate/NBu<sub>4</sub>X was previously reported by our group.<sup>[80d]</sup> In this section we will present the reaction mechanism of the same reaction with minor changes that will be crucial to reproduce the kinetic results obtained experimentally (see **Figure 3.4**). The reaction mechanism involves 1,2-epoxyhexane as

epoxide, tetrabutylammonium iodide (TBAI) is used as co-catalyst and the  $[Al^{Cl}]$  complex is used as Lewis acid, having chlorides as aromatic substituents in the phenolate ligand.

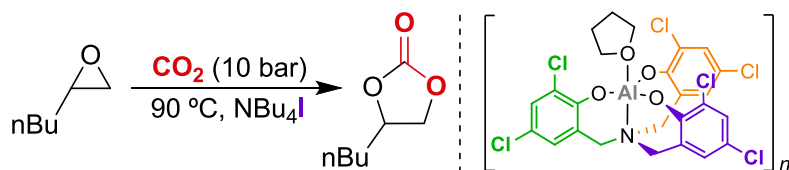


**Figure 3.4** Schematic representation of cyclic carbonate formation from 1,2-epoxyhexane and CO<sub>2</sub> catalyzed by  $[Al^{Cl}]$  and TBAI.

The obtained free-energy profile taking into account the conditions indicated in **Figure 3.4** will be considered to analyze the effect of several factors like solvation, entropy or the chosen DFT functional. These factors will be analyzed by comparing the calculated TOF from the obtained Gibbs free-energy with the experimentally obtained TOF (36,000 h<sup>-1</sup>). First, we evaluated the effect of the solvation in the Gibbs free-energy profile.

Initially, we considered two scenarios regarding how we compute the geometry optimization of all intermediates and transition states. In the first case we carried out the geometry optimization in gas phase without any implicit solvation. Then, using the optimized geometry we calculate the potential energy using implicit solvation. Finally, we obtain the solvation energy calculating the energy difference of both potential energies as it can be seen in **Eq. 3.1**. After obtaining the solvation energy, by adding it the Gibbs free-energy term computed in the gas phase, we obtain the Gibbs free-energy in solution (see **Eq. 3.2**).

$$\Delta E_{solv} = E_{solution} - E_{gas} \quad \text{Eq. 3.1}$$

$$\Delta G_{solv} = \Delta E_{solv} + G_{gas} \quad \text{Eq. 3.2}$$

The second methodology is based on computing the geometry optimization and the vibrational frequencies in solution, obtaining  $\Delta G_{solv}$  directly. The main difference between these two approaches is the obtained structure after geometry optimization, since in the first case is optimized neglecting the dielectric effect of the solvent around the molecule. Therefore, in the case of high polar or charged molecules, major differences will be observed between the two methods. The reaction energy profile for the target reaction obtained using both methodologies is illustrated below in **Figure 3.5**.

Initially, we will describe the reaction mechanism using the *Opt Gas* profile, related to the first methodology described above. The first step of the reaction is the exergonic ( $-8.9 \text{ kcal}\cdot\text{mol}^{-1}$ ) coordination of the epoxide to the axial position of the  $[\text{Al}^{\text{Cl}}]$  complex, decoordinating the THF located in that position.

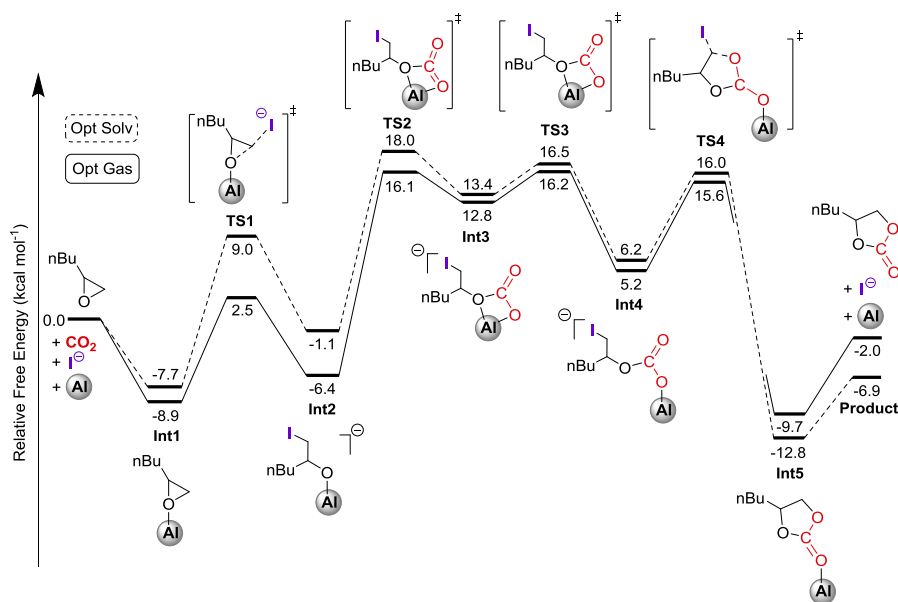


**Figure 3.5** Gibbs free-energy profile for the cyclic carbonate formation from  $\text{CO}_2$  and 1,2-epoxyhexane catalyzed by the  $[\text{Al}^{\text{Cl}}]/\text{TBAI}$  binary system, calculated at the B3LYP level. Energy profile for optimized geometries in solvent is depicted in dashed line.

The activation of the epoxide is crucial to facilitate the ring-opening process via the nucleophilic attack of iodide. The Gibbs free-energy relative barrier of this step is  $11.4 \text{ kcal}\cdot\text{mol}^{-1}$ , which has been computed as the free-energy difference from **TS1** to **Int1**. The formed intermediate from **TS1** is **Int2**, which is an alkoxide stabilized by the  $[\text{Al}^{\text{Cl}}]$  complex, but less stable than **Int1**. The nucleophilicity of **Int2** enhances the activation and insertion of  $\text{CO}_2$ , generating the C-O bond through **TS2** ( $16.1 \text{ kcal}\cdot\text{mol}^{-1}$ ) leading to a meta-stable octahedral carbonate named **Int3** ( $12.8 \text{ kcal}\cdot\text{mol}^{-1}$ ). The insertion of  $\text{CO}_2$  to the alkoxide intermediate presents a relative barrier of  $22.5 \text{ kcal}\cdot\text{mol}^{-1}$ . After **Int3** is formed, an isomerization process takes place, forming a linear hemi-carbonate (**Int4**) via **TS3**, which presents a Gibbs free-energy value of  $16.2 \text{ kcal}\cdot\text{mol}^{-1}$ , similar to **TS2**. The conformation of **Int4** facilitates the ring-closing step via the nucleophilic attack of the carbonyl oxygen to the electrophilic carbon bonded to the iodide substituent. This process occurs rapidly via **TS4**, which constitutes a relative barrier of  $10.4 \text{ kcal}\cdot\text{mol}^{-1}$  and leads to the final product still coordinated to  $[\text{Al}^{\text{Cl}}]$  (**Int5**) with a Gibbs free-energy of  $-9.7 \text{ kcal}\cdot\text{mol}^{-1}$ . Using iodide as nucleophile it is important because iodide is a good leaving group in comparison to other halides. Consequently, if we would consider bromide or chloride the ring-closing process would be more energetically demanding. The used halide can play a role in the chemoselectivity of the process, since using the same catalytic system we can obtain both the cyclic carbonate and the polycarbonate. We will discuss the chemoselectivity when the halide is changed in section 5.2 of this Thesis.

The last step after cyclic carbonate formation is the decoordination of the product through an endergonic process of  $7.7 \text{ kcal}\cdot\text{mol}^{-1}$ , indicating the high oxophilicity of aluminum already observed in the high stabilization of **Int1**. Therefore, the Gibbs free-energy of the reaction, computed as the energy difference between products and reactants, is  $-2.0 \text{ kcal}\cdot\text{mol}^{-1}$ , indicating the minor stabilization of the formed product respect to the reactant. This low reaction energy observed is caused by the high thermodynamic stability of  $\text{CO}_2$  that compensates the high internal

energy of the epoxide. The kinetic stability of CO<sub>2</sub> is also an important drawback to tackle in CO<sub>2</sub> fixation. In this mechanism, the insertion and isomerization steps are the most energetically demanding of the whole mechanism, hence constituting the TDTS. The absolute Gibbs free-energy of the reaction is computed as the energy difference from the TS with highest energy to the Int with lowest energy. In this case, **TS3** is the most energetically demanding TS, named TOF Determining Transition State (TDTS) and **Int1** is the most stable Int, named TOF Determining Intermediate (TDI), hence the absolute barrier of the reaction is 25.1 kcal·mol<sup>-1</sup>.

Considering the obtained Gibbs free-energy profile we would obtain a Turn-Over Frequency (TOF) of 7.12h<sup>-1</sup>, which is four orders of magnitude lower than the experimental TOF (3.6x10<sup>4</sup>h<sup>-1</sup>). After discounting other mechanistic possibilities, we considered some factors that may change the obtained Gibbs free-energy. First one was how we take into account the solvation effects in the Gibbs free-energy.

As we introduced previously, we considered an alternative approach to account the contribution of solvation to the Gibbs free-energy of the system, which consists in including implicit solvation to the molecule when we compute the geometry optimization calculation. Hence we will observe major differences respect the first method in charged intermediates or structures with high polarity. The obtained reaction energy profile is included in **Figure 3.5** (dashed line), where we can observe only major differences in the first step regarding epoxide ring-opening by the nucleophilic attack of iodide. As we expected, in this step where free iodide is incorporated to the system, the relative barrier increases by 5.3 kcal·mol<sup>-1</sup>, with respect to the previously calculated because we overestimate the stabilization of bonding free iodide during the geometry optimization in gas phase. This energy difference is only slightly observed in CO<sub>2</sub> insertion where the relative barrier decreases by 3.4 kcal·mol<sup>-1</sup> respect the previous methodology because the minor stabilization of **Int2**. If we compare both methodologies in other steps

like cyclic carbonate ring-closing, we see minor differences respect relative barriers, being the *Opt-Solv* barrier only  $0.6 \text{ kcal}\cdot\text{mol}^{-1}$  lower than *Opt-Gas*. Despite all we mentioned until now regarding the comparative between relative barriers, the absolute barrier of both reaction energy profiles is very similar, being  $25.1 \text{ kcal}\cdot\text{mol}^{-1}$  for *Opt-Gas* and  $25.7 \text{ kcal}\cdot\text{mol}^{-1}$  for *Opt-Solv*. Though *Opt-Gas* barrier is slightly lower than *Opt-Solv*, when we calculate the TOF using the AUTOF program, we obtain a higher TOF for *Opt-Solv* methodology, being  $7.24\text{h}^{-1}$  for *Opt-Solv* in comparison with  $7.12\text{h}^{-1}$  for *Opt-Gas*. We would not expect this inverse trend when using Eyring's equation because we would consider exclusively the absolute barrier. As we mentioned, using *Opt-Solv* methodology we obtained intermediates with higher Gibbs free-energy values, constituting lower relative barriers. Therefore, the "kinetic resistance" decreases, thus increasing the TOF value. Despite the variation between the two TOFs is not considerable, it is worth mentioning an example where it can be easily seen that the entire profile affects the resulting TOF, and not only the absolute barrier of the reaction.

In conclusion, how solvation contribution is included into the system it is not crucial in this case, observing minor differences in the shape of the Gibb free-energy profile and, consequently, in the calculated TOF. In order to enhance comprehension, all the results presented in this chapter will consider the *Opt-Solv* methodology.

### 3.2.3.b Evaluation of different DFT functionals. The key role of dispersion corrections

The major advance that DFT based-methods meant for computational chemistry in terms of accuracy ratio versus affordability are undeniable. However, choosing the proper DFT functional is always under discussion in the community because we can observe significant differences when we use different DFT functionals. In this case we considered four DFT functionals, being B3LYP,  $\omega$ B97XD, M06-2X and B97-D3. As we detailed in section 3.2.2, these four functionals are representative of

different groups commonly employed by the computational chemistry community. The resulting Gibbs free-energy profiles calculated for all DFT functionals are showed below in **Figure 3.6**.

The reaction profile related to B3LYP was already described in the previous section. The first trend that can be easily observed in **Figure 3.6** is the lower Gibbs free-energies accounted for all the other DFT functionals that include dispersion parameters to describe properly the van der Waals forces. In our system, these interactions are important because several reasons. First, the aminotriphenolate ligand of the  $[Al^{Cl}]$  complex is stabilized by  $\pi$ -stacking between the aromatic rings. Second, there is a significant interaction between the organic tail of the 1,2-epoxyhexane and the ligand of the Al complex. And last but not least, when the carbonate is formed after inserting the  $CO_2$  to the alkoxide (**TS2**), the system is more crowded around the catalyst, observing a major interaction between the coordinated moiety and the ligand, thus observing a stabilization when dispersion parameters are included. The insertion step was the TDTS in the previously presented results. If this step is stabilized respect B3LYP, we should expect lower absolute barriers for the functionals that include the attractive London interactions. Indeed, this is the trend observed that we will describe more in detail for each DFT functional.

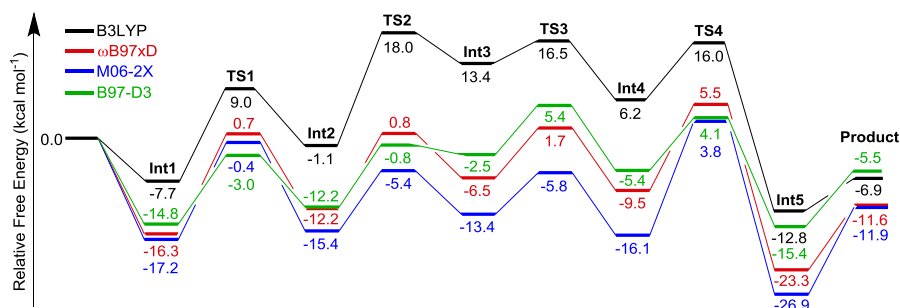


**Figure 3.6** Gibbs free-energy profile for the cyclic carbonate formation from  $CO_2$  and 1,2-epoxyhexane catalyzed by the  $[Al^{Cl}]/TBAI$  binary system, calculated at the B3LYP (black trace),  $\omega$ B97xD (red trace), M06-2X (blue trace) and B97-D3 (green trace) level. All reaction energy profiles depicted are computed by *Opt-Solv* methodology.



The relative barriers for all steps are collected in **Table 3.1**, in order to facilitate its visualization. The absolute barrier for all three dispersion-corrected functionals is 4 or 5 kcal·mol<sup>-1</sup> below B3LYP, which leads to higher TOFs. On the other hand, CO<sub>2</sub> insertion is the only relative barrier higher for B3LYP in comparison to dispersion-corrected functionals. We can see in these results that the more attractive we consider the van der Waals interactions, the more the absolute barrier decreases. The B97-D3 functional with Grimme's dispersion, presents the lowest absolute barrier and also considerably low relative barriers. On the other hand, using  $\omega$ B97XD and M06-2X, we obtained very similar results regarding absolute and relative barriers. Nevertheless, the trend for all functionals is very similar, being the isomerization the fastest process and CO<sub>2</sub> insertion and ring-closing the more energetically demanding. We can confirm this trend by analyzing which are the TDI and TDTS for each functional. In all cases, **Int1** is the lowest energy intermediate, thus constituting the resting state of the reaction (TDI). On the other hand, TDTS changes among each functional. For B3LYP, the TDTS is **TS2**, for  $\omega$ B97XD and M06-2X is **TS3** and for B97-D3 is **TS4**. The similar energy between **TS2**, **TS3** and **TS4** impede to determine which step is rate-determining of the reaction.

**Table 3.1** Relative and absolute barriers ( $\Delta G$ ) for the Al-catalyzed formation of cyclic carbonate from CO<sub>2</sub> and 1,2-epoxyhexane at B3LYP,  $\omega$ B97XD, M06-2X and B97-D3 level. TOF Determining Intermediate (TDI) and TOF Determining Transition State (TDTS) and the resulting TOF are indicated in the last columns. The experimental TOF is highlighted in bold.

DFT Functional	TS1	TS2	TS3	TS4	Product	$\Delta G^\ddagger$	TDI-TDTS	TOF (h <sup>-1</sup> )
B3LYP	16.7	19.1	3.1	9.8	5.9	25.7	Int1-TS2	7.24
$\omega$ B97XD	17.0	13.0	8.2	15.0	11.7	21.8	Int1-TS4	2.0x10 <sup>3</sup>
M06-2X	17.6	10.0	7.6	19.9	15.0	21.0	Int1-TS4	4.6x10 <sup>3</sup>
B97-D3	11.8	11.6	7.9	9.5	9.9	20.2	Int1-TS3	1.6x10 <sup>4</sup>
								<b>3.6 x 10<sup>4</sup></b>

Finally, if we compare the computationally obtained TOF with the experimental one, we determine that B3LYP is the less accurate method for this system, while B97-D3 computed TOF is the closest to the experimental reference ( $1.6 \times 10^4 \text{ h}^{-1}$ ).

The hybrid long-range corrected  $\omega$ B97XD ( $2.0 \times 10^3 \text{ h}^{-1}$ ) and the parametrized M06-2X ( $4.6 \times 10^3 \text{ h}^{-1}$ ) functionals presented more accurate results than B3LYP but less accurate than B97-D3.

### 3.2.3.c Realistic approximations to account the translational entropy in solution

Solvent-solvent and solute-solvent interactions play an important role in homogeneous catalysis.<sup>[53b, 94]</sup> An issue that has received much attention is the loss of translational entropy associated with the formation of one moiety from two molecules in solution. Normally, gas phase calculations overestimate translational entropy contributions in solution. Approaches for including entropy corrections have been proposed by several authors, which have been detailed in Chapter 2 of this Thesis. The simplest of these methods accounts only the vibrational and rotational terms in the calculation of the total entropy in solution, i.e., it neglects the translational entropy terms from the calculation of the gas-phase total entropy. The other two approaches employed in the present study are based on the fact that the equations used for calculating the thermodynamics of the reactions are applicable to a hypothetical ideal gas at concentrations (1/24.5 M) equivalent to standard state  $P=1 \text{ atm}$  and  $T=298.15 \text{ K}$ . However, concentration in our experiments is not 1/24.5 M, and therefore corrections are necessary to obtain results that can be applicable at the concentration of the system under study. Martin, Wertz and Cooper and Ziegler introduced some empirical method to correct such overestimation to the entropy in solution.

Taking into account these methodologies, we included entropy corrections for all the free-energy values in the reaction energy profile and

for the B3LYP,  $\omega$ B97XD, M06-2X and B97-D3 functionals. The results for B3LYP functional are shown in **Figure 3.7**.

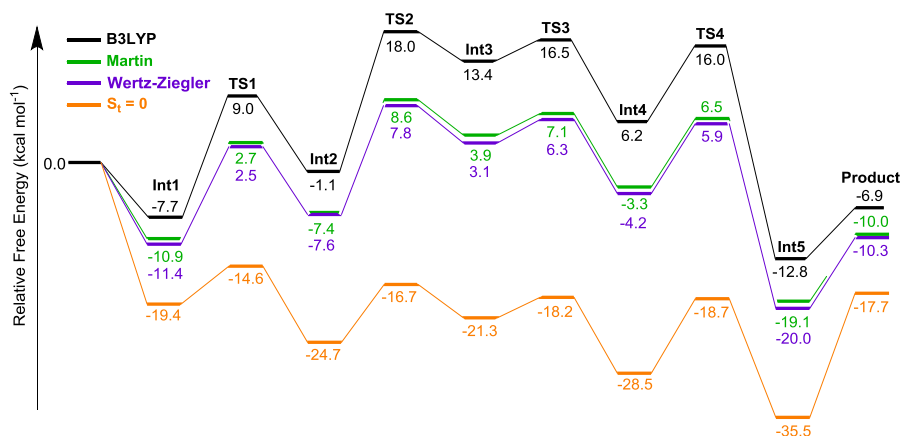


**Figure 3.7** Gibbs free-energy profile for the cyclic carbonate formation from CO<sub>2</sub> and 1,2-epoxyhexane catalyzed by the [Al<sup>Cl</sup>]/TBAI binary system, calculated at the B3LYP level (black trace). The orange line stands for the pathway including only the vibrational and rotational terms in the calculation of the total entropy in solution. Corrections by Martin, and Wertz/Ziegler appear in green and purple, respectively. All reaction energy profiles depicted are computed by *Opt-Solv* methodology.

Both Martin and Wertz/Ziegler (W/Z) corrections reduce moderately all relative Gibbs free-energy values. Alternatively, by neglecting the translational entropy ( $S_t$ ) we observe a much larger decrease. However, as we expected, the initial trend remains constant after accounting the entropic corrections except for  $S_t$  approximation, which will be described first due to its particularity. When neglecting the translational entropy to the Gibbs free-energy, we are overestimating the stabilizing effect of forming one body from two independent entities. Thus, we observe a very large stabilization after **TS2** when four independent bodies considered initially ([Al<sup>Cl</sup>], iodide, epoxide and CO<sub>2</sub>) are forming only one complex. This behavior leads to unusual results like **TS1** being the most energetically demanding step meanwhile in all other approximations, including the non-corrected results, the ring-opening of the epoxide is always the least energetically demanding step of the reaction profile.

Another significant difference is the TDI and TDTS of the Gibbs free-energy profile. Since taking away molecular bodies is so many disfavored, the rate-determining step is the decoordination of the cyclic carbonate from  $[Al^C]$ . The results obtained using this approximation proves the importance of taking care on the translational entropy when a significant number of entities are bonded or separated.

**Table 3.2** Relative and absolute barriers ( $\Delta G$ ) for the Al-catalyzed formation of cyclic carbonate from  $CO_2$  and 1,2-epoxyhexane considering no entropic corrections and using Martin, W/Z and  $S_t$  corrections. TOF Determining Intermediate (TDI) and TOF Determining Transition State (TDTS) and the resulting TOF are indicated in the last columns. The experimental TOF is highlighted in bold.

B3LYP	TS1	TS2	TS3	TS4	Product	$\Delta G^\ddagger$	TDI-TDTS	TOF ( $h^{-1}$ )
Uncorrected	16.7	19.1	3.1	9.8	5.9	25.7	Int1-TS2	7.24
Martin	13.6	16.0	3.2	9.8	9.1	19.5	Int1-TS2	$3.9 \times 10^4$
W/Z	13.9	15.4	3.2	10.1	9.7	19.2	Int1-TS2	$5.8 \times 10^4$
$S_t$	4.8	8.0	3.1	9.8	9.8	17.8	Int5-Product	$2.6 \times 10^5$
								<b><math>3.6 \times 10^4</math></b>

Using both Martin and W/Z corrections we obtained more realistic results than using  $S_t$  approximation. First, it is worth mentioning that despite both approximation tackle the problematic of correcting the translational entropy in solution from different mathematic perspectives, the obtained results are practically identical for all the employed DFT functionals.

In **Figure 3.7** it can be seen such similarity and also, the identical trend obtained comparing with the uncorrected profile. All the relative barriers, the TDI and TDTS with the absolute barrier and the consequent TOFs are collected above in **Table 3.2**, where we can observe also the different trend when considering  $S_t$  approximation.

Nevertheless, it is worth mentioning the relative barrier of  $S_t$  profile related to **TS3**, which is similar to the other reaction profiles because

there is no variation in the number of bodies involved in the previous and next step, hence maintaining the same translational entropy in the system. Consequently, the relative barrier for this step is identical to the other profiles, confirming the overestimation of the effect when neglecting the translational entropy. On the other hand, the absolute barrier and relative barriers for Martin and W/Z corrections are very similar, hence obtaining very similar TOFs. Both TOFs obtained with Martin and W/Z profiles present high correlation with the experimental reference, confirming the importance of including these entropic corrections when describing multicomponent systems in solution.

The absolute barriers and the related TOFs for all the considered DFT functionals and entropic corrections considering *Opt-Solv* methodology are collected in **Table 3.3** in the next page.

**Table 3.3** Absolute barriers ( $\Delta G$ ) and TOFs for the Al-catalyzed formation of cyclic carbonate from CO<sub>2</sub> and 1,2-epoxyhexane considering no entropic corrections and using Martin, W/Z and S<sub>t</sub> corrections. TOF Determining Intermediate (TDI) and TOF Determining Transition State (TDTS) are indicated in the last columns. The experimental TOF and the consequent barrier computed using Eyring's equation are highlighted in bold in the last row.

DFT Functional	$\Delta G^\ddagger$ (kcal·mol <sup>-1</sup> )	TOF (h <sup>-1</sup> )	TDI	TDTS
B3LYP	25.7	7.24	Int1	TS2
B3LYP (S <sub>t</sub> )	17.8	2.6 x 10 <sup>5</sup>	Int5	Product
B3LYP (M)	19.4	3.9 x 10 <sup>4</sup>	Int1	TS2
B3LYP (W/Z)	19.1	5.8 x 10 <sup>4</sup>	Int1	TS2
$\omega$ B97XD	21.8	2.0 x 10 <sup>3</sup>	Int1	TS4
$\omega$ B97XD (S <sub>t</sub> )	23.6	79.0	Int5	Product
$\omega$ B97XD (M)	15.5	4.9 x 10 <sup>6</sup>	Int1	TS4
$\omega$ B97XD (W/Z)	15.7	3.4 x 10 <sup>6</sup>	Int5	Product
M06-2X	21.1	4.6 x 10 <sup>3</sup>	Int1	TS3
M06-2X (S <sub>t</sub> )	28.0	0.15	Int4	Product
M06-2X (M)	19.9	2.4 x 10 <sup>4</sup>	Int4	TS4
M06-2X (W/Z)	19.2	4.0 x 10 <sup>4</sup>	Int4	TS4
B97-D3	20.2	1.6 x 10 <sup>4</sup>	Int1	TS3
B97-D3 (S <sub>t</sub> )	23.8	59	Int4	Product
B97-D3 (M)	14.4	2.9 x 10 <sup>7</sup>	Int2	TS3
B97-D3 (W/Z)	14.2	2.7 x 10 <sup>7</sup>	Int5	Product
<b>Experimental</b>	<b>19.7</b>	<b>3.6 x 10<sup>4</sup></b>		

As we already commented in the previous section when we compared the DFT functionals, the general trend is maintained for all functionals with the main difference observed between B3LYP and dispersion-corrected

functionals. After including the three entropic corrections, we can confirm the underestimation of Gibbs free-energy values for  $S_{\text{t}}$  approximation. In all cases, the decoordination step is rate-determining in the reaction profile obtaining irregular absolute barriers and TOFs.

Regarding Martin and W/Z corrections, we can see excessively low barriers for  $\omega$ B97XD and B97-D3 functionals, obtaining too high TOFs in comparison with the experimental reference. On the other hand, when M06-2X functional is considered, both Martin and W/Z TOFs correlate with the experimental value. In some cases like  $\omega$ B97XD and B97-D3 functionals accounting W/Z functional, the decoordination step was also rate-determining. Alternatively, more realistic results are obtained using Martin's approximation for all cases.

### 3.2.4 Conclusions

The formation of cyclic carbonate from  $\text{CO}_2$  and 1,2-epoxyhexane mediated by the  $[\text{Al}^{\text{Cl}}]/\text{TBAI}$  binary system was studied using several DFT functionals, solvation methodologies and entropic corrections. M06-2X,  $\omega$ B97XD and B97-D3 significantly reduced the values of the relative free-energy differences in comparison to those obtained at the B3LYP level. The ring-closing reaction is rate-determining for  $\omega$ B97XD dispersion-included free-energy profile, whereas the  $\text{CO}_2$  insertion step was found to be the rate-determining step with the hybrid B3LYP functional. Alternatively, the carbonate isomerization was the most energetically demanding step for M06-2X and B97-D3 functionals.

Different approaches for correcting entropies in solution were considered and showed dramatic effects on the free-energy values, which worth full determination and evaluation. Enthalpy and, consequently internal energy remains constant, so Gibbs free-energy changes because translational entropy correction. This free-energy variation was quantified for Martin correction as  $3.15 \text{ kcal}\cdot\text{mol}^{-1}$  by each bond formed between two bodies.

No definitive conclusions arise by neglecting the translational entropy contributions completely. For B3LYP cases, energy barriers are overestimated. Turnover frequencies for the reaction were estimated using the energetic span model. Compared to B3LYP results, a remarkable increment of three orders of magnitude in the TOF value was observed using the M06-2X and  $\omega$ B97XD functionals and four order of magnitude using B97-D3, thus in better agreement with the experiments. TOFs lying in the same order of magnitude as the optimal experiments were predicted for B3LYP, M06-2X and  $\omega$ B97XD profiles obtained using the Martin approach to entropy corrections in solution. The use of entropic corrections by the Wertz and Ziegler methodology leads to TOFs exceeding the highest value obtained experimentally.

The results from the current studies suggest that a proper combination of DFT and entropic corrections provide a method of great predictive use in catalyst selection and design, thus for contributing to advance the field of CO<sub>2</sub> catalysis more efficiently.

### 3.3 Epoxy-Alcohols as Building Blocks for Functionalized Cyclic Carbonates

#### 3.3.1 Goals and Motivation

The formation of cyclic carbonates from CO<sub>2</sub> and epoxides is discussed in many contributions of several groups. Moreover, the elucidation of the reaction mechanism catalyzed by the binary [Al<sup>R</sup>]/TBAI system was already published by our group and described in detail from a quantitative perspective in the previous section of this chapter. However, the use of functionalized substrates, and specifically alcohol- and amine-substituted epoxides present an interesting mechanistic change in CO<sub>2</sub> fixation processes. In particular, using our [Al<sup>R</sup>] catalyst and glycidol (GL) as substrate we observe high yields for glycidol carbonate (GC) without using the nucleophilic co-catalyst required in the previously studied



systems. In this case, the basicity of the phenolate ligand of  $[Al^R]$  leads to an acid-base reaction with the acidic proton of the alcohol group, hence forming a positively charged complex ( $[Al^R-H^+]$ ) and an alkoxide moiety that can initiate the  $CO_2$  fixation reaction. This new reactivity presents many aspects to be defined, which have been summarized in a schematic representation of the reaction (see **Figure 3.8**). In this case, methyl groups are present in the phenolate group of the ligand, increasing its basic character, which is a crucial feature in this mechanism.

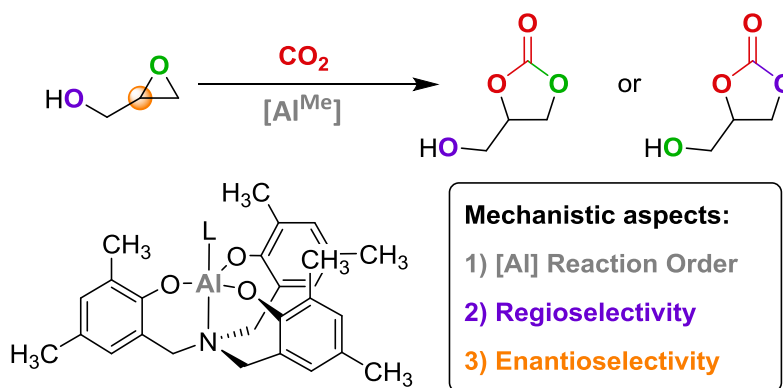


**Figure 3.8** Schematic representation of glycidol carbonate formation from glycidol and  $CO_2$  catalyzed by the Al aminotriphenolate complex.

The first factor that will be studied is the reaction order of the catalyst. Two reactive oxygen atoms are present in the system, epoxide and alcohol, so we could observe a 2:1 ( $[Al]:GL$ ) dependence, leading to a kinetic order of reaction of 2 for the catalyst respect to the substrate. The second factor to be considered is regioselectivity. The difference between the new reaction mechanism involving the functional group included to the epoxide and the previously reported mechanism via epoxide ring-opening process is the first aspect to be defined. The kinetic competition between these two mechanisms determines the regioselectivity of  $CO_2$  insertion.

Finally, GL and also glycidol derivatives are chiral substrates with at least one enantiomeric center, which has been highlighted in orange in **Figure 3.8**. Consequently, the elucidated mechanism has to explain the

experimentally obtained enantioselectivity. We have experimental evidence provided by Kleij and coworkers that facilitates the analysis of these mentioned mechanistic aspects by comparing the experimental and computational results. Consequently, during the description and discussion of our results, we will comment also the experimental data in parallel with our results.

### 3.3.2 Computational Details

All calculations in this study were carried out by using Gaussian 09 package.<sup>[86]</sup> Two type of dispersion-corrected DFT functionals were used to optimize geometries and evaluate energies: the  $\omega$ B97XD<sup>[44]</sup> and the B97-D3.<sup>[87b, 95]</sup> Noteworthy, both functionals give fully equivalent results in most of the cases, although for some weakly bound structures the different treatment of dispersion effects makes a difference. The standard 6-311G(d,p) basis set<sup>[89]</sup> was used to describe all atoms. Full geometry optimizations were performed without any constrain. The nature of the encountered stationary points was characterized either as minima or transition states by means of harmonic vibrational frequency analysis. Gibbs free-energies were calculated at experimental conditions (T=323.15 K, P=1 atm). Entropic corrections were included for all calculations in order to model the translational entropy in solvation.<sup>[56]</sup> For the sake of comparison with experimentally measured infrared spectra, several DFT functionals were used:  $\omega$ B97XD with scaling factor 0.957,<sup>[96]</sup> B3PW91<sup>[43, 97]</sup> with scaling factor 0.963,<sup>[96]</sup> and BP86<sup>[38]</sup> unscaled.

Solvent effects were accounted for in all calculations by using the Solvation Model based on Density (SMD) as implemented in Gaussian. The dielectric constant ( $\epsilon$ ) of the polarizable medium was set to the value reported for butanone ( $\epsilon=18.246$ ), which is the solvent used in the experiments.<sup>[91]</sup>

### 3.3.3 Results and Discussion

#### 3.3.3.a Catalyst reaction order

Glycidol (GL) contains two oxygen atoms in its structure, the epoxide oxygen ( $O_{Ep}$ ) and the hydroxyl oxygen ( $O_{OH}$ ). This difference with the typically studied epoxides that present only one oxygen atom leads to the possibility of having a double coordination of  $[Al^{Me}_c]$  to GL, hence having one Al bonded to  $O_{OH}$  and another Al bonded to  $O_{Ep}$ . Consequently, the reaction could occur through a monometallic or a bimetallic mechanism. In this section we will present the reaction mechanism related to the insertion of  $CO_2$  to the alcohol group considering one and two  $[Al^{Me}_c]$  (see **Figure 3.9**).

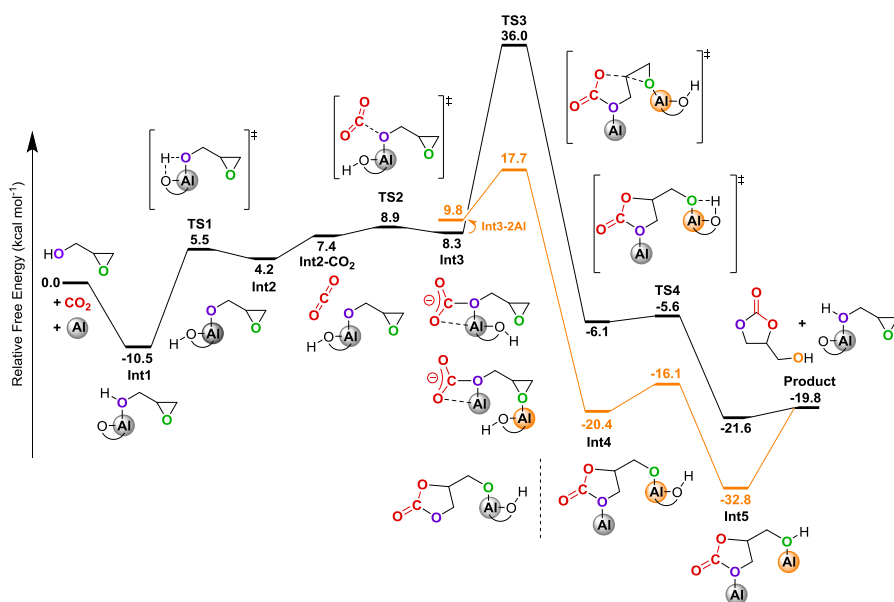


**Figure 3.9** Gibbs free-energy profile ( $\text{kcal}\cdot\text{mol}^{-1}$ ) of the monometallic (black line) and bimetallic (orange line) mechanisms for GC formation.

The first step of the reaction is the coordination of GL to  $[Al^{Me}_c]$  through the alcohol group, forming a stable intermediate at ( $-10.5 \text{ kcal}\cdot\text{mol}^{-1}$ ). The coordination via  $O_{Ep}$  is energetically similar ( $-10.2 \text{ kcal}\cdot\text{mol}^{-1}$ ). Therefore, both conformations may take place simultaneously. However, **Int1**,

where GL is bonded to Al metal from O<sub>OH</sub>, has been isolated and characterized by X-Ray crystallography, hence confirming this intermediate as resting state of the mechanism. The activation of the alcohol group facilitates the proton transfer from the substrate to the ligand of the catalyst through **TS1**, constituting a relative barrier of 11.0 kcal·mol<sup>-1</sup>.

The obtained alkoxide is energetically close to **TS1**, although is stabilized by [Al<sup>Me</sup>] (4.2 kcal·mol<sup>-1</sup>). An alkoxide intermediate, as we showed in the mechanism described in the previous section, is a reactive moiety for CO<sub>2</sub> insertion. Thus, after forming a meta-stable ensemble (**Int2-CO<sub>2</sub>**), the insertion reaction takes place via **TS2**. The relative barrier of this process is 4.5 kcal·mol<sup>-1</sup>, computed from **Int2**.

The formation of **Int3** is stabilized by the interaction of the carbonyl oxygen of the carbonate with Al metal, forming a chelate moiety that constitutes an [Al<sup>Me</sup>] octahedral structure. This carbonate intermediate may evolve towards ring-closing process through a monometallic route via **TS3** (36.0 kcal·mol<sup>-1</sup>) or following a bimetallic pathway forming first **Int3-2Al** (9.8 kcal·mol<sup>-1</sup>) to then overcome a more favourable TS of 17.7 kcal·mol<sup>-1</sup>. For both cases **TS3** constitutes the rate-determining step of the reaction, leading to a 46.5 and 28.2 kcal·mol<sup>-1</sup> absolute barrier for monometallic and bimetallic mechanisms, respectively. The large difference (18.3 kcal·mol<sup>-1</sup>) between absolute barriers of monometallic and bimetallic mechanisms is due to the activation of the epoxide moiety when [Al<sup>Me</sup>] is bonded to O<sub>Ep</sub>. The second Al metal bonded to GL stabilizes the formed alkoxide after the ring-closing step, hence having a more stable **Int4** when two Al are considered. After ring-closing step, the proton is rapidly transferred back to the substrate via **TS4**, leading to the desired product still bonded to [Al<sup>Me</sup>]. The obtained Gibbs free-energy of the reaction is -19.8 kcal·mol<sup>-1</sup>, constituting an exergonic reaction.

Considering the previous results, we could expect that two Al centres are crucial to facilitate the ring-closing step, so decreasing the absolute barrier of the reaction.

### 3.3.3.b Determination of CO<sub>2</sub> insertion selectivity

Considering a bimetallic mechanism, we studied an alternative reaction mechanism to the already presented in the previous section. In this case, **Int2** evolves through the nucleophilic attack to a coordinated epoxide, forming a new alkoxide. This step is described by **TS2'** in **Figure 3.10**. In this reaction pathway, **Int2** is used as a nucleophilic catalytic species, mimicking the iodide role in the mechanism described in section 3.2.3.a of this chapter. The main difference between the two presented mechanisms is where CO<sub>2</sub> is inserted (O<sub>Ep</sub> or O<sub>OH</sub>). In the mechanism previously depicted in **Figure 3.9**, CO<sub>2</sub> is inserted to O<sub>OH</sub>, while in this new mechanism CO<sub>2</sub> binds to O<sub>Ep</sub> of **Int3'**. Therefore, opposite regioselectivity concerning CO<sub>2</sub> insertion is observed between these mechanistic pathways.

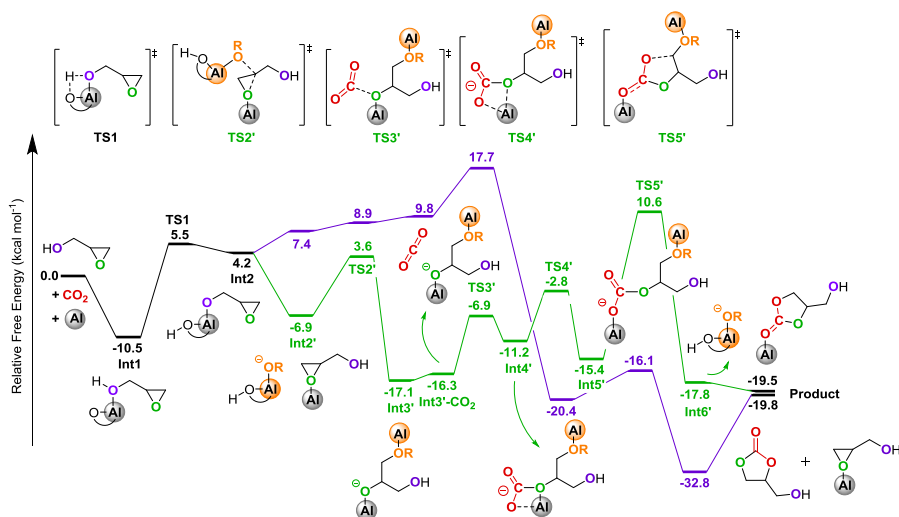


**Figure 3.10** Gibbs energy profile (kcal·mol<sup>-1</sup>) of the bimetallic mechanisms of GC formation concerning CO<sub>2</sub> insertion to O<sub>OH</sub> (purple line) and O<sub>Ep</sub> (green line).

After CO<sub>2</sub> insertion takes place through **TS3'**, **Int4'** is formed and the new reaction mechanism follows the same steps of isomerization towards hemi-carbonate and then ring-closing step, forming the cyclic carbonate as we presented above in the previously studied mechanism. As it can be seen in **Figure 3.10**, the ring-closing process (**TS5** and **TS5'**) is rate-

determining for both cases. The absolute barrier is also similar for both cases, being  $28.2 \text{ kcal}\cdot\text{mol}^{-1}$  for  $\text{CO}_2$  insertion to  $\text{O}_{\text{OH}}$  and  $27.7 \text{ kcal}\cdot\text{mol}^{-1}$  for  $\text{CO}_2$  insertion to  $\text{O}_{\text{Ep}}$ , so the presented mechanisms are kinetically competitive.

Summarizing, the reaction mechanism could take place through a bimetallic mechanism with an absolute barrier of approximately  $28 \text{ kcal}\cdot\text{mol}^{-1}$ , obtaining a mixture of  $\text{CO}_2$  insertion to  $\text{O}_{\text{OH}}$  and  $\text{O}_{\text{Ep}}$ . However, the experimental results show a different trend respect our computational results.

First, as we show in **Figure 3.11**, by using deuterated GL we observe exclusively the formation of GC with  $\text{CO}_2$  inserted to  $\text{O}_{\text{OH}}$ . Moreover, a kinetic study determined the absolute barrier at  $23.3 \text{ kcal}\cdot\text{mol}^{-1}$ , which is considerably lower than the computationally obtained. Finally, the  $[\text{Al}^{\text{Me}}]$  reaction order obtained by kinetic studies was one, thus the reaction mechanism should take place through a monometallic mechanism.

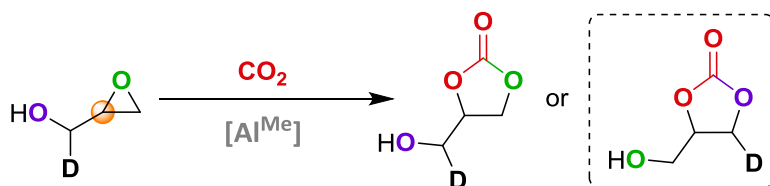


**Figure 3.11** Schematic representation of experimental results using deuterated GL to study the regioselectivity of  $\text{CO}_2$  insertion.

The disconnection between computational and experimental results prompted us to explore other mechanistic possibilities considering only one  $[\text{Al}^{\text{Me}}]$  and  $\text{CO}_2$  insertion to hydroxyl group. The crucial role of the second  $[\text{Al}^{\text{Me}}]$  activating the epoxide of GL was taken into account to look for a more favourable monometallic mechanism than the already studied.

### 3.3.3.c Revealing the crucial role of water as proton shuttle

The importance of including an additional  $[\text{Al}^{\text{Me}}]$  is to activate both oxygen atoms present in the substrate. In literature there are many examples where this effect could be also accounted by other species

through hydrogen bonding (HB) interactions.<sup>[98]</sup> In our case, GL contains a hydroxyl group that is a potential HB actor. Moreover, there are high possibilities that small amounts of water are present in our system because the high solubility of water in glycidol and butanone. Actually, water can hydrolyze epoxides at relatively high temperatures forming diols or even triols when epoxy alcohols are considered. Nevertheless, no hydrolysis has been observed in our system at the given conditions.

Intermolecular HB interactions between glycidol, water and  $[Al^{Me}]$  structure could be crucial in the reaction mechanism, particularly in the ring-closing process described by **TS3**. The water molecule can activate  $O_{Ep}$  through HB while at the same time interacting with the proton attached to the phenolate of  $[Al^{Me}]$ . Consequently, water would act equally as a co-catalyst activating the epoxide and as proton shuttle facilitating the protonation of the oxygen after ring-closing of GC. The computed mechanism using water is depicted below in **Figure 3.12**.

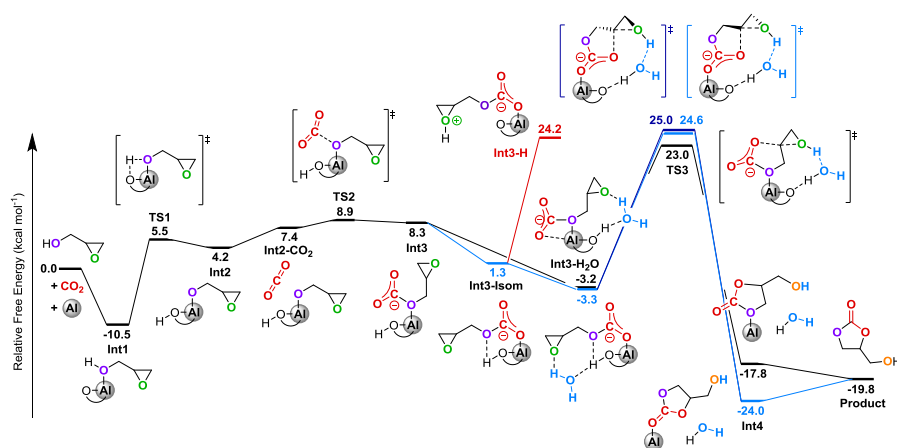


**Figure 3.12** Gibbs energy profile (kcal·mol<sup>-1</sup>) of the S<sub>N</sub>1 type mechanism (blue lines) and S<sub>N</sub>2 type mechanism (black line) for the GC formation co-catalyzed by water. An unfeasible process regarding protonation of  $O_{Ep}$  is illustrated in *Int3-H* (red line).

Until **Int3**, the presented mechanism is identical to the mechanism already showed in **Figure 3.9**. Incorporating a water molecule to the system, the Gibbs free-energy of **Int3** dramatically decreases from 8.3 kcal·mol<sup>-1</sup> to -3.2 kcal·mol<sup>-1</sup> (**Int3-H<sub>2</sub>O**) because the stabilizing effect of

two HB interactions between the water molecule and both  $O_{Ep}$  and the proton bonded to the phenolate ligand. The resulting **TS3** after **Int3-H<sub>2</sub>O** is  $13.0 \text{ kcal}\cdot\text{mol}^{-1}$  lower than **TS3** of **Figure 3.9**, hence confirming the importance of activating  $O_{Ep}$ . Another significant difference is **TS3** leads directly to the formation of GC bonded to the catalyst (**Int4**), since the protonation of  $O_{Ep}$  occurs in parallel to ring-closing process in a concerted TS.

An alternative reaction mechanism can take place through the isomerization of **Int3** to a linear hemi-carbonate (**Int3-Isom**) similar to **Int5'** in **Figure 3.10**. This isomerization increases the flexibility of the coordinated moiety, allowing a  $S_N1$  type reaction mechanism. Therefore, through this reaction pathway depicted in **Figure 3.12**, we could obtain both enantiomers depending on the orientation of the nucleophilic attack of the carbonate to the epoxide. The obtained absolute barrier ( $35.1$  or  $35.5 \text{ kcal}\cdot\text{mol}^{-1}$ ) is close to the absolute barrier of the enantioselective mechanism presented before ( $33.5 \text{ kcal}\cdot\text{mol}^{-1}$ ). Consequently, one would expect that both reaction mechanisms,  $S_N2$  type and  $S_N1$  type, could occur simultaneously leading to low enantioselectivity. Actually, the experimentally obtained enantiomeric excess is approximately 50%, which means a 75:25 ratio between the enantiomers of GC. These experimental results coincide with the elucidated mechanisms because  $S_N2$  type mechanism leads to full inversion after **TS3**, while  $S_N1$  type path forms both enantiomers in the same proportion.

The role of water as co-catalyst indicated by these computational findings was later on reaffirmed by experiments carried out in anhydrous conditions. Using the same experimental conditions of catalyst loading, time of reaction, temperature and  $\text{CO}_2$  pressure, half of the yield was obtained respect to normal conditions when the solvent and the substrate were dried. Conversion is observed because GL can also play the same role as water does. Therefore, the reaction could be autocatalyzed by the substrate. Though  $[Al^{Me}]$  reaction order, regioselectivity and enantioselectivity coincide with the experimental data, the Gibbs free-



energy barrier for these mechanisms is too high for a reaction that occurs at mild conditions of temperature and CO<sub>2</sub> pressure. Actually, as we indicated above, the activation energy obtained from the kinetic experiments is 23.3 kcal·mol<sup>-1</sup>, which is 11.2 kcal·mol<sup>-1</sup> lower than S<sub>N</sub>2 type mechanism.

### 3.3.3.d CO<sub>2</sub> insertion and ring-closing in one step

The high barrier of the reaction mechanism presented above prompted us to look for a new mechanistic pathway keeping water as co-catalyst of the process. The reaction mechanism presented below in **Figure 3.13** allowed us to explain the first order dependence on both reactant and catalyst, the regioselectivity of CO<sub>2</sub> insertion towards O<sub>Ep</sub> and the enantioselectivity observed experimentally.

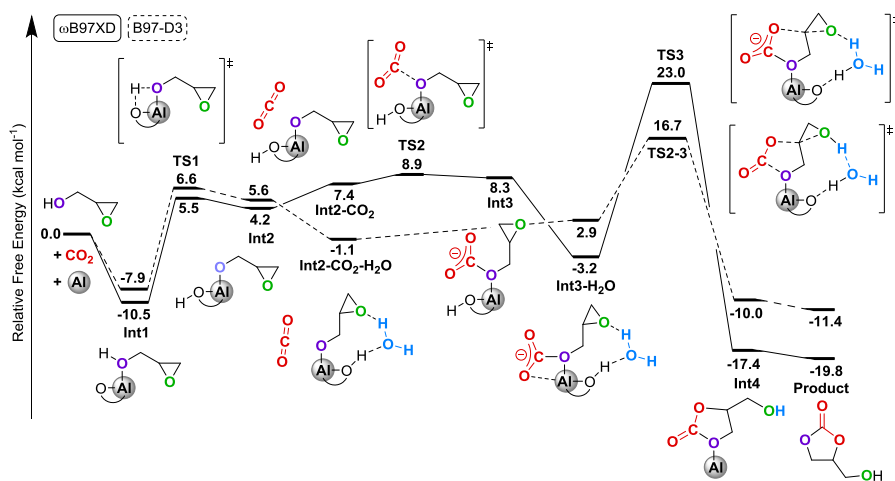


**Figure 3.13** Gibbs free-energy profile for the concerted (dashed line) and stepwise (solid line) mechanisms of GC formation from GL and CO<sub>2</sub> catalyzed by [Al]<sup>Me</sup>.

A concerted mechanism regarding CO<sub>2</sub> insertion and ring-closing step occurring at the same time was elucidated using B97-D3 functional. The different treatment of dispersion interactions with respect to the previously used ωB97XD functional, led to a different **TS3** (named **TS2-3**) with longer bond distance between the carbon atom of CO<sub>2</sub> moiety

and  $O_{OH}$  of the substrate, thus having the  $CO_2$  insertion and the nucleophilic attack of the oxygen of  $CO_2$  to the epoxide at the same time.

Another important difference between the two mechanisms in **Figure 3.13** is the distance between  $O_{Ep}$  and the proton of water that it is transferred to GC. In the concerted mechanism,  $O_{Ep}$ -H distance is shorter, facilitating the epoxide opening process because the oxygen atom of  $CO_2$  is less nucleophilic than the same oxygen when the  $CO_2$  moiety is bonded to the substrate forming a carbonate.

The resulting absolute barrier of the concerted mechanism is  $24.6 \text{ kcal}\cdot\text{mol}^{-1}$ , which is  $8.9 \text{ kcal}\cdot\text{mol}^{-1}$  lower than stepwise barrier. Moreover, the concerted mechanism barrier is closer to the experimentally determined ( $23.3 \text{ kcal}\cdot\text{mol}^{-1}$ ), which reaffirms its feasibility. One could wonder how this reaction mechanism describes the obtained enantiomeric excess in the experiments, since it should be expected an absolute enantioselectivity for the opposite enantiomer to the initial GL substrate, as occurs in the  $S_N2$  type mechanism. We discussed this issue in the next section of this chapter.

Despite the complete description of the reaction mechanism supported by experimental data, we could not consider both reaction mechanisms using the same DFT functional. This matter prompted us to compute the intermediate and TS involved in the absolute barrier using different DFT functionals and different dispersion corrections. The obtained results for eleven different DFT functionals are collected in **Table 3.4**.

As it can be seen in the table depicted in the next page, a general trend in favour of the concerted mechanism is observed. Nevertheless, different absolute barriers and structural parameters regarding angle of  $CO_2$ ,  $C_{CO_2}$ - $O_{OH}$  distance and epoxide distance were obtained for the considered DFT functionals. Therefore, we moved forward to higher level of theory in order to shed some light to the mechanism elucidation.

**Table 3.4** DFT functional benchmark regarding *TS3* of GC formation from GL and CO<sub>2</sub> catalyzed by [Al<sup>Me</sup>]. Structure parameters are collected for *TS3* like CO<sub>2</sub> angle, distance between C of CO<sub>2</sub> and O of GL and angle of epoxide functional group of GL. The absolute Gibbs free-energy barrier is included with a clarification about the nature of *TS3* regarding concerted or stepwise mechanism.

DFT Functional	$\alpha$ CO <sub>2</sub>	d(C <sub>CO2</sub> -O <sub>OH</sub> )	$\alpha$ Epox	$\Delta G^\ddagger$ (kcal·mol <sup>-1</sup> )	Concerted vs Stepwise
<b>B97-D3BJ</b>	<b>150</b>	<b>1.9</b>	<b>90</b>	<b>24.7</b>	<b>Concerted</b>
B97-D3	151	2	91	25.3	Concerted
B3LYP-D3BJ	139	1.6	80	26.2	Concerted
B3LYP-D3	140	1.6	80	27.5	Concerted
PBE	142	1.7	78	31.1	Concerted
BP86	145	1.8	81	33.7	Concerted
BP86-D3	140	1.7	80	18.3	Concerted
M06	160	2.2	101	31.5	Concerted
M06-2X	136	1.5	76	32.0	Stepwise
<b><math>\omega</math>B97XD</b>	<b>136</b>	<b>1.5</b>	<b>74</b>	<b>33.5</b>	<b>Stepwise</b>
<b>B2PLYP</b>	<b>139</b>	<b>1.6</b>	<b>79</b>	<b>28.0</b>	<b>Concerted</b>

Double-hybrid DFT methods that include MP2 correlation factors were used to recalculate the intermediate and TS responsible of the absolute barrier of the mechanism. Therefore, B2PLYP functional with Grimme's dispersion correction was used for this purpose. The obtained TS was **TS2-3** (concerted mechanism) and the calculated barrier was 28.0 kcal·mol<sup>-1</sup> (see last row of **Table 3.4**). These very similar results to B3LYP-D3 or B3LYP-D3BJ indicate that hybrid DFT functionals describe accurately the studied system.

In conclusion, an unusual concerted mechanism is observed for epoxy-alcohol reaction with CO<sub>2</sub>. It is worth mentioning the double reactive character of CO<sub>2</sub> in the very same step. On one hand, electrophilic character of the carbon atom interacts with the nucleophilic oxygen of

the alkoxide. On the other hand, one oxygen of CO<sub>2</sub> undergoes nucleophilic addition to the epoxide group.

### 3.3.3.e Racemization of Glycidol Carbonate

The enantioselectivity of the process has been studied computationally to shed light on the enantiomeric excess obtained experimentally. The ring-opening of the epoxide by the nucleophilic attack of the carbonate (**TS3**) is the reaction step that determines the enantioselectivity. An S<sub>N</sub>1 type mechanism leads to racemization and S<sub>N</sub>2 type mechanism to inversion of the configuration. Our computational results show a small difference between S<sub>N</sub>2 (black line) and S<sub>N</sub>1 (blue lines) absolute barriers in **Figure 3.12**, which agrees with the experimental enantiomeric excess. However, the experimental conditions are too mild to overcome the high absolute barriers of both processes. Consequently, the enantiomeric excess could not be explained by those results.

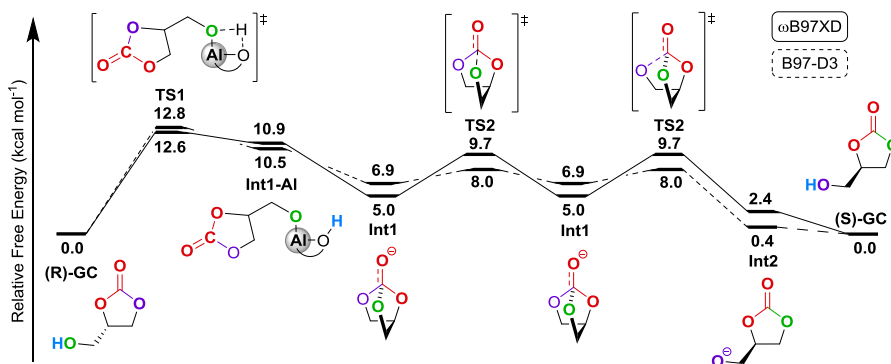


**Figure 3.14** Gibbs free-energy profile of the acid-base racemization mechanism computed with B97-D3 (dashed line) and ωB97XD (solid line).

The characterization of the product carried out by the experimentalists to determine the enantioselectivity goes through an aminolysis reaction to produce a chiral amide. The amine used to open the cyclic carbonate can also deprotonate the alcohol group present in the product through **TS1** (12.8 kcal·mol<sup>-1</sup> for dashed line) depicted in **Figure 3.14**. After the alkoxide is obtained (**Int1-Al**), it can rapidly go through **TS2** to a stable

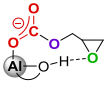
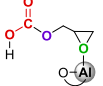


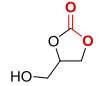
symmetric intermediate (**Int1**). Due to the described process is symmetric, the same **TS2** leads to the final product (**S-GC**), which could invert or retain the configuration.

A detailed study on this racemization process is carried out by QM/MM metadynamic simulations in Chapter 6 of this Thesis.

### 3.3.3.f Vibrational Frequencies Analysis: IR *in operando*

IR *in operando* is a complex characterization technique that our collaborators, Urakawa et. al, used to identify crucial intermediates of the reaction mechanism by observing how particular IR signals were appearing and disappearing during the reaction. By adding sequentially CO<sub>2</sub> and the catalyst to the system they detected how specific IR signs were changing after the additions.

**Table 3.5** DFT-computed structures for several intermediates, carbonate C=O vibrational frequency, and relative Gibbs free-energy. Experimental observed structures are highlighted in bold. Calculated vibrational frequency for B3PW91 and  $\omega$ B97XD are scaled by 0.963 and 0.957, respectively.

IR					
BP86 (cm <sup>-1</sup> )	1779	1783	1758	<b>1835</b>	<b>1805</b>
B3PW91 (cm <sup>-1</sup> )	1770	1792	1765	<b>1825</b>	<b>1812</b>
$\omega$ B97XD (cm <sup>-1</sup> )	1777	1805	1795	<b>1830</b>	<b>1825</b>
$\Delta G^\ddagger$ (kcal·mol <sup>-1</sup> )	<b>1.3</b>	<b>2.2</b>	<b>4.6</b>	<b>-3.2</b>	<b>-19.8</b>
Experiment (cm <sup>-1</sup> )	<b>1837</b>			<b>1790</b>	

Aimed at identifying species responsible of the infrared signal experimentally observed at 1837 cm<sup>-1</sup>, we considered several candidates and computed the harmonic vibrational frequencies using some DFT methods. CO<sub>2</sub> interacts with the glycidol alkoxide as well as with the aluminum metal center, forming a stable intermediate with a relative Gibbs energy of -3.2 kcal·mol<sup>-1</sup>. This species highlighted in bold in

**Table 3.5** presents a vibration corresponding to the carbonate C=O stretching in the closest agreement with the experimental value. The vibration of C=O for GC is also included in **Table 3.5** as a reference.

### 3.3.4 Conclusions

Elucidating and describing in detail the mechanistic aspects of CO<sub>2</sub> fixation to form cyclic carbonates is crucial to improve the activity of the catalytic systems used for this important process. In this section, we elucidated the reaction mechanism of CO<sub>2</sub> fixation using functionalized epoxides, particularly epoxy alcohols. The singular reactivity of epoxy alcohols led to a complex reaction mechanism based on hydrogen bond interactions.

First, we studied the catalyst reaction order considering monometallic and bimetallic mechanisms. The bimetallic mechanism was found more favorable because the stabilizing effect of the second aluminum to the oxygen of the epoxide, thus facilitating the ring-closing process to form the cyclic carbonate.

Second, we compared two bimetallic mechanisms with opposite regioselectivity towards CO<sub>2</sub> fixation. In one hand, the already presented mechanism where CO<sub>2</sub> is inserted to the hydroxyl oxygen. On the other hand, the conventional mechanism with CO<sub>2</sub> insertion to the epoxide group. Both mechanisms were found kinetically similar.

We substituted the effect of the second Al complex of bimetallic systems by a water molecule, which additionally facilitated the recovery of the proton from the phenolate ligand. Hence, water was involved as co-catalyst playing a crucial role in the insertion of CO<sub>2</sub> and the cyclic carbonate closing process and as proton-shuttle to protonate the formed alkoxide after epoxide is opened.

The insertion of CO<sub>2</sub> happening at the same time with the nucleophilic attack to open the epoxide group and the protonation of the epoxide oxygen is rate-determining of the glycidol carbonate formation with an

absolute barrier of  $24.6 \text{ kcal}\cdot\text{mol}^{-1}$ , close to the experimental reference ( $23.3 \text{ kcal}\cdot\text{mol}^{-1}$ ). We confirmed the preference of the concerted mechanism over the stepwise mechanism using a double-hybrid functional.

The experimentally observed enantioselectivity was explained by a racemization process that occurs after glycidol carbonate is formed.

Experimental procedures like IR *in operando*, X-ray crystallography, deuterium labelling or kinetic experiments were combined with DFT based methods to confirm key aspects of the mechanism, hence we present a detailed study of the system that may be extrapolated to similar processes for the formation of heterocyclic products.

UNIVERSITAT ROVIRA I VIRGILI

Computational Design of Catalysts for Carbon Dioxide Recycling

Joan González Fabra



*"Everything should be made as  
simple as possible, but not simpler."  
Albert Einstein*

# Chapter 4

## N-Aryl Carbamates

### 4.1 Organocatalyzed N-Aryl Carbamates from Cyclic Carbonates

#### 4.1.1 Introduction

The valorization of CO<sub>2</sub> is important to create value from waste material. Currently efforts have already shown great potential towards the use of CO<sub>2</sub> to store energy,<sup>[14-15]</sup> and as a synthon for the creation of new polymers<sup>[33b, 99]</sup> and fine-chemicals.<sup>[20c, 100]</sup> Regarding the synthesis of fine-chemicals, cyclic carbonates (CyCs) present interesting versatility on its reactivity towards many high value products.<sup>[101]</sup> In the previous chapter of this Thesis we presented two computational studies regarding the elucidation of reaction mechanisms to create CyCs from CO<sub>2</sub> fixation with epoxides. In this chapter we focus on aminolysis of CyCs, which is one of the most representative reactions of CyCs due to its flexibility, high

activity and selectivity.<sup>[102]</sup> Nevertheless, in **Figure 4.1** we show other reactions based on the electrophilic character of CyCs. As it can be seen, a wide variety of nucleophilic reactants can transform CyCs to functionalized moieties that present high potential as polymerization blocks or synthons for complex molecular structures. Aminolysis reaction using aromatic substrates is highlighted in green in **Figure 4.1**. The aminolysis of CyCs using aromatic amines leads to decarboxylation processes because harsh reaction conditions are used to overcome the high kinetic barrier. Alternatively to aromatic amines, aliphatic amines can lead to the formation of N-alkyl carbamates due to its higher nucleophilic character. Consequently, milder reaction conditions can be used, hence preventing the decarboxylation of the carbonate.

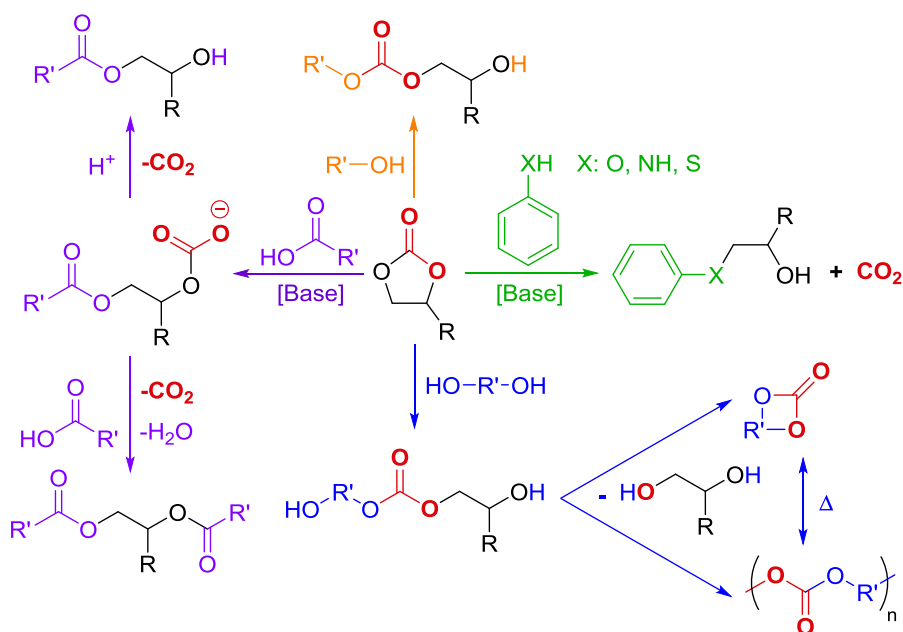


**Figure 4.1** Summary of CyC reactivity regarding nucleophilic attack to carbonyl carbon or  $\alpha$ -carbon to carbonate group.

The reaction mechanism of aminolysis of CyCs using aliphatic amines is depicted in detail in **Figure 4.2**. The nucleophilic attack of the amine usually occurs in a regioselective manner to the carbonyl carbon of the

substrate. The nitrogen atom of the amine has a high electron density, which attacks preferably (Pearson theory) to the hard electrophilic center of CyC, which is the carbonyl carbon. After the amine is bonded to the carbonyl carbon a zwitterionic intermediate is formed, which is deprotonated by an external amine forming an anionic structure (alkoxide) and an ammonium cation. Then, the alkoxide can evolve to two different paths depending which C-O bond is broken to open the five-member ring. Both possible pathways, which lead to different isomers, are illustrated in **Figure 4.2**. The last step of aminolysis is the protonation of the alkoxide, by the ammonium previously formed, to generate the corresponding alcohol.

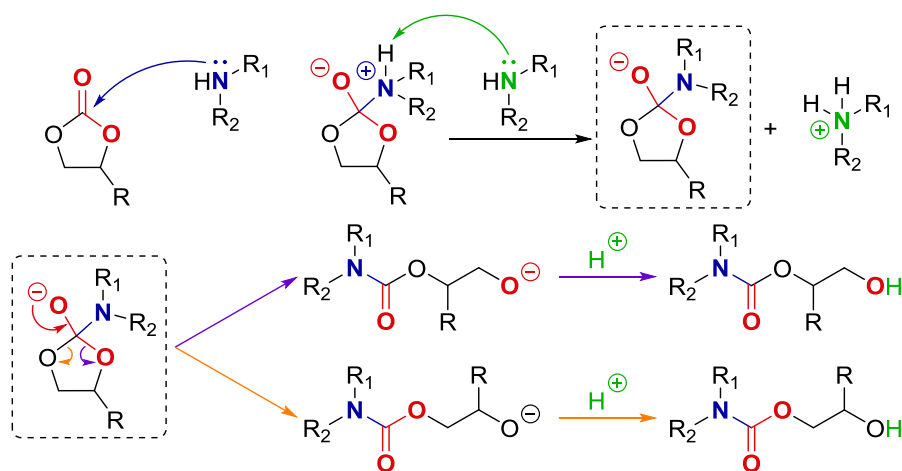


**Figure 4.2** Schematic representation of the aminolysis reaction mechanism considering an aliphatic amine and a generic CyC.

The aminolysis reaction can lead to multiple products when changing the nucleophilic character of the amine, the functional groups present in the CyC or even the reaction conditions. As it can be seen below in **Figure 4.3**, using a functionalized CyC we can observe a double aminolysis reaction (A and B pathways) after the first amine addition. The amine can attack the ester group (A) or the carbamate group (B) forming a carbamate and an amide (A) or an ester and urea (B), respectively. In both

cases, alcohol groups are formed after the protonation of the generated alkoxide, as we described above.

An alternative pathway is the thermal decomposition of the carbamate (C) forming a five-member cyclic carbamate (oxazolidinone). Oxazolidinones are useful substrates in chiral synthesis as Evans auxiliaries in aldol reactions.<sup>[103]</sup>

The last route depicted in **Figure 4.3** (D) is already presented in **Figure 4.1** for aromatic amines, where nucleophilic attack takes place at the  $\alpha$ -carbon to the carbonate group. After nucleophilic attack to  $\alpha$ -carbon,  $\text{CO}_2$  and an amine are formed. The formed amine can react with the carbonyl carbon of the first amine, or even with itself, thus forming a wide variety of amides. Consequently, constituting a process with very low chemoselectivity, which is one of the main issues to tackle when designing new catalysts for aminolysis.

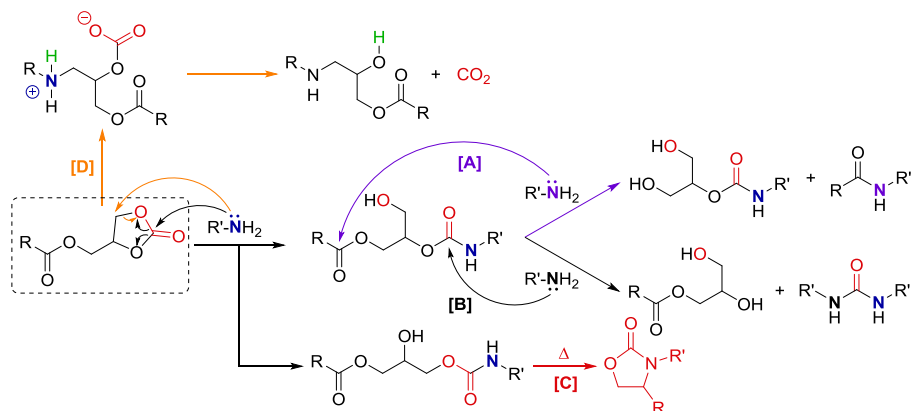


**Figure 4.3** Schematic representation of cyclic carbonate aminolysis reactions. **A:** amide and carbamate formation (purple). **B:** urea formation (black). **C:** thermal decomposition to produce oxazolidinones (red). **D:** decarboxylative aminolysis (orange).

As we mentioned previously, CyCs are widely used as precursors for polymer synthesis,<sup>[104]</sup> particularly in polyurethane production via aminolysis reaction. In **Figure 4.4**, we show a synthetic route to produce polyhydroxyurethanes using CyCs, amines and methacrylic anhydride.<sup>[105]</sup>

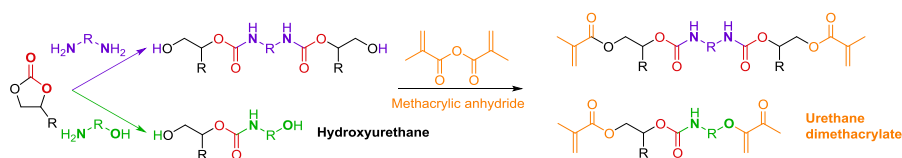


**Figure 4.4** Reaction of CyC, amines and methacrylic anhydride to form polyhydroxyurethane via aminolysis reaction.

Three different moieties are incorporated to the highly functionalized polymer using this technology that enable us to start from waste (CO<sub>2</sub>) and easily accessible substrates (epoxides and amines) to produce high valuable polymers.

Herein, we report a computational study on the reaction mechanism of arylamines with CyCs to produce chemoselectively N-aryl carbamates (ACs) using triazabicyclodecene (TBD) as catalyst.

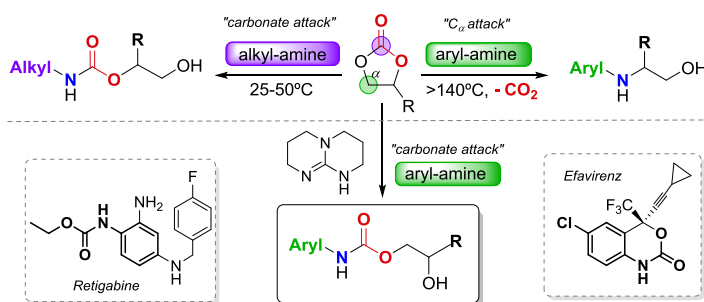


**Figure 4.5.** Reaction manifold of CyC with amines and new reactivity towards AC formation under mild conditions.

TBD is an organic and cheap strong guanidine base (see **Figure 4.5**). Guanidine based catalyst are used in many base-mediated organic reactions like Michael,<sup>[106]</sup> Wittig,<sup>[107]</sup> nitroaldol reactions<sup>[108]</sup> or ring opening polymerization (ROP) of cyclic esters.<sup>[109]</sup> While the formation of organic carbamates from aliphatic amines is well defined, it still remains highly challenging to selectively prepare ACs through a site-specific aminolysis reaction using aromatic amines under mild reaction conditions. These AC compounds are particularly attractive scaffolds as they are key moieties of some pharmaceutical compounds such as

*Efavirenz*<sup>[110]</sup> and *Retigabine*<sup>[111]</sup> (see **Figure 4.5**). This interesting reaction has been previously accomplished in a chemoselective manner using metal-based catalysts that require harsh reaction conditions<sup>[112]</sup> or the conventional synthetic route using isocyanates.<sup>[113]</sup>

Also, thermolysis of ACs offers a useful, phosgene-free route towards aryl isocyanates which are key reagents in the synthesis of polyurethane polymers.<sup>[114]</sup> Inspired by this unresolved challenge, we explored the reaction mechanism towards ACs through hydrogen-bond activation of CyCs, which could offer a viable substrate conversion strategy as recently demonstrated for aminolysis reactions involving alkylamines.<sup>[112a]</sup>

#### 4.1.2 Goals

The organocatalyzed reaction mechanism for aminolysis of CyC using arylamines is still unknown. In this chapter we aim to elucidate such reaction mechanism catalyzed by guanidine based organocatalysts.

Aiming at unravel the mechanism of the organocatalyzed reaction, we will study firstly the uncatalyzed reaction of aliphatic and aromatic amines to produce alkyl and aryl amines. We expect that the reaction will be facilitated by HB agents like water, which we will study later together with the true organocatalyst TBD.

We will evaluate the description of this organic system by DFT based methods considering a post-HF method like CCSD(T) as reference. The detailed computational study in the description accuracy of the system corroborates the viability of the proposed catalyzed mechanism.

Finally, the activity of arylamines and alkylamines will be compared for all mechanistic situations, contrasting our computational results with the experimental observations, thus corroborating both evidence.

#### 4.1.3 Computational Details

All calculations reported in the manuscript were carried out by using the Gaussian 09 package.<sup>[115]</sup> The Becke gradient corrected hybrid exchange-

correlation functional<sup>[116]</sup> was used with the inclusion of Grimme's<sup>[41-42]</sup> third generation empirical dispersion energy corrections (B97-D3). The Pople<sup>[117]</sup> 6-311G(d,p) standard basis set was used to describe the whole system where all geometries were fully optimized without constraints. Moreover, stationary points were characterized as minima or transition states through the calculation of harmonic vibrational frequencies. Gibbs free-energies were computed at standard conditions of temperature (T=298.15 K) and pressure (P=1 atm). Entropic corrections have been used following the model of Martin and coworkers<sup>[56]</sup> in order to account for the effects of solvent pressure on the entropy of the system. All geometries have been optimized with a polarizable continuum solvent using SMD model developed by Truhlar et. al.<sup>[52]</sup> The default dielectric constants ( $\epsilon$ ) were employed in the calculation using the reactants butylamine ( $\epsilon=4.62$ ) and aniline ( $\epsilon=6.89$ ) as the implicit solvent media in their respective reactions, since the reaction occurs in neat condition.<sup>[91]</sup>

The Coupled cluster<sup>[118]</sup> post-HF method was employed including single, double and non-iterative triple excitations<sup>[119]</sup> on the stationary points obtained using DFT based methods. The same basis set was used (6-311G(d,p)) as in the DFT based calculations. Free-energy estimates were then computed adding the vibrational, rotational and translational contributions obtained from the previous B97-D3 runs.

## 4.1.4 Results and Discussion

### 4.1.4.a Uncatalyzed Reaction Mechanism

Before we study the catalyzed reaction mechanism for ACs formation we elucidated the uncatalyzed mechanism in order to have better insight on the system. In this first section we present our results about propene cyclic carbonate (PC) reaction with two different amines; aniline and butylamine. As we introduced before, butylamine is an aliphatic amine, so a more nucleophilic reagent than aniline, which is an aromatic amine. Consequently, we should observe lower kinetic barriers towards

aminolysis when butylamine is considered. The obtained Gibbs free-energy profiles are depicted in **Figure 4.6**. The first step of the reaction is the ensemble of PC and the amine (**Int0**) through the hydrogen-interaction of a proton of the amine with the carbonyl oxygen of PC.

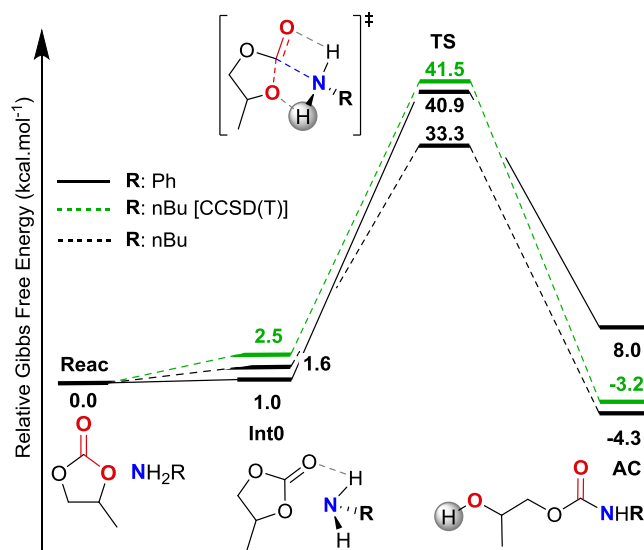


**Figure 4.6** Gibbs free-energy profiles for aniline (solid black line) and butylamine (dashed black line) attack on PC to form AC products. For all profiles, B97D3/6-311G(d,p) was used whereas CCSD(T)/6-311G(d,p) - B97D3/6-311G(d,p) (green dashed line) was applied only for the non-catalyzed reaction with butylamine.

This slightly endergonic process leads to the **TS** of the reaction, where a proton of the amine is transferred to a carbonate oxygen while C-N bond is formed in a concerted manner. The obtained product is more stable than the reactant for butylamine but not for aniline, in agreement with experimental observations. Nevertheless, this is not a highly exergonic process. In the case of butylamine  $\Delta G_r$  is  $-4.3 \text{ kcal}\cdot\text{mol}^{-1}$ . As we expected, the activation energy of aniline profile (solid black line) is considerably higher than butylamine (dashed black line) by  $8.5 \text{ kcal}\cdot\text{mol}^{-1}$ . Still, both reactions are kinetically unfavorable and unfeasible at room temperature.



In order to confirm the accuracy of DFT based methods describing this system, we computed the potential energy of all the optimized structures using the reference method CCSD(T). The Gibbs free-energy contribution obtained by DFT was used to calculate the final Gibbs free-energy indicated in the green dashed line in **Figure 4.6**. The obtained barrier using CCSD(T) is  $41.5 \text{ kcal}\cdot\text{mol}^{-1}$ , which is slightly higher than DFT but observing the same trend in the Gibbs free-energy profile and also similar relative values. Consequently, we can confirm that DFT based methods present appropriate accuracy describing this system.

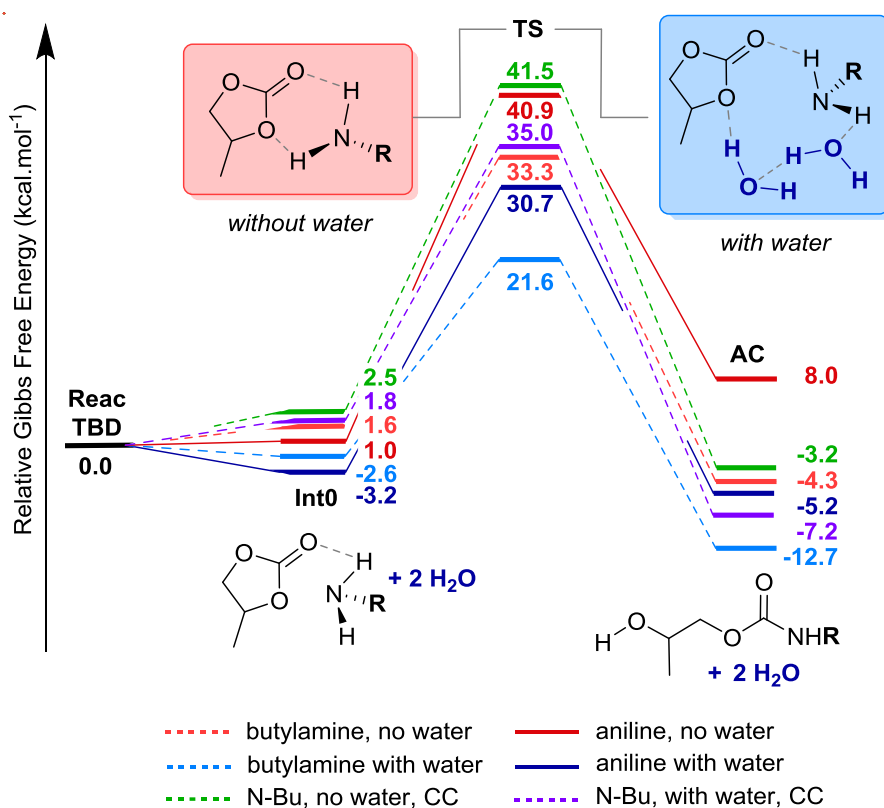


**Figure 4.7** Gibbs free-energy profiles for aniline (solid lines) and butylamine (dashed lines) attack on PC to form AC products. Two mechanisms were considered: direct nucleophilic attack (red lines) and a water catalyzed pathway (blue lines). For all profiles, B97D3/6-311G(d,p) (red and blue) was used, whereas CCSD(T)/6-311G(d,p) - B97D3/6-311G(d,p) was applied only for the non-catalyzed (dashed green line) and water-catalyzed (dashed purple line) reaction with butylamine.

The presented calculations point out that a direct butylamine attack is not kinetically favored at room temperature. Therefore, our results do not explain the high yield observed experimentally when aliphatic amines are used in aminolysis reaction. As we already proved in the previous chapter of this Thesis, water can be present in the reaction media forming HB interactions that facilitate the proton transfer process. The presence of water acting as a proton-relay catalyst was considered as the reactions are not performed under anhydrous conditions. The obtained results, in conjunction with the previously presented, are depicted above in **Figure 4.7**.

This new mechanism indeed decreases significantly the barrier for the aniline pathway from 40.9 to 33.9 kcal mol<sup>-1</sup>, though this value still remains considerably high for the reaction to occur under ambient conditions. For the butylamine case, the barrier was also effectively lowered to 24.2 kcal mol<sup>-1</sup> confirming the experimental observation that the reaction proceeds smoothly at room temperature. The obtained absolute barrier using water as co-catalyst was determined at 35.0 kcal mol<sup>-1</sup> by means of CCSD(T) (dashed purple line), decreasing the energetic span by 6.5 kcal·mol<sup>-1</sup> respect non-catalyzed barrier, thereby unequivocally demonstrating that the presence of water is crucial for the process to occur and also revealing that B97-D3 functional, at most, only slightly underestimates the barriers.

#### 4.1.4.b N-aryl carbamate formation catalyzed by TBD

The detailed study on the uncatalyzed and water-catalyzed mechanism presented in the previous section provides crucial information to facilitate the TBD-catalyzed mechanism elucidation. The key role of water acting as proton-shuttle was established. In particular, two water molecules improved the carbamate formation due to a more relaxed structure in comparison to a one-water transition state. The conformation of the TS when two water molecules are used is similar to TBD, which presents also two nitrogen atoms that can bind one proton each.

The results for the TBD-mediated reactions (depicted in **Figure 4.8**) show that the mechanism for the transformation of butylamine and aniline involves several steps. Both reactions have remarkably similar barriers, 18.1 and 17.5 kcal·mol<sup>-1</sup> for aniline and butylamine, respectively. These values are consistent with the reactions taking place at room temperature. Noteworthy, both are very similar, thus the nucleophilic character of the used amine is no longer of any importance when TBD is used as catalyst.

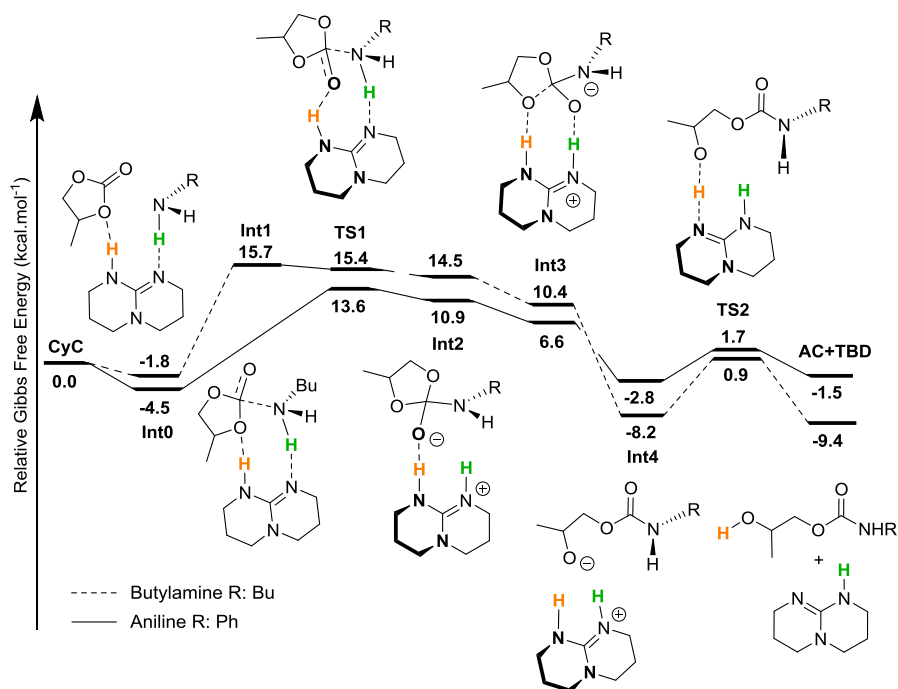


**Figure 4.8** Gibbs free-energy profile for the TBD-catalyzed reaction mechanism of PC with aniline (solid line) and butylamine (dashed line). The proton relay is highlighted as the original TBD proton (orange) adds formally to the carbonate structure, and the amine proton (green) is incorporated into the catalyst structure.

The mechanistic pathways are slightly different for each substrate. The first intermediate (**Int0**) could only be optimized for the butylamine pathway. In this step, the amine approaches the carbonate group, with the carbon center adopting a tetrahedral geometry. Next, **TS1** is a mutual step and rate-determining for both reaction pathways. This transition state constitutes an ion pair comprising of a protonated TBDH<sup>+</sup> and an

alkoxide (**Int1**). The formation of **Int2** is characterized by an elongated C–O bond (1.66 Å) in the cyclic species and is stabilized by two hydrogen bonds with the TBDH<sup>+</sup> species. In the subsequent step, **Int3** is produced and the substrate is now linear, retaining still an alkoxide character. The final step is the proton transfer from TBDH<sup>+</sup> to the substrate through **TS2**.

Compared with the reaction assisted by water, TBD is a much more effective proton-relay catalyst providing significantly lower kinetic barriers. Also, when MTBD (methylated TBD) was used, much poorer catalysis behavior was noted (26% conversion for MTBD, 75% conversion for TBD) clearly indicating that H-bonding stabilization is also crucial in this reaction.

#### 4.1.5 Conclusions

Herein, we present a detailed study on the uncatalyzed reaction of CyC aminolysis and the reaction mechanism of a new and highly attractive route towards the challenging formation of N-aryl carbamates from CyCs that can be obtained by CO<sub>2</sub> addition to epoxides, and aromatic amines under solvent-free and metal-free conditions.

TBD is shown to be an effective organocatalyst for the site-selective and chemo-selective formation of the N-aryl carbamate products. Our computational results demonstrated the inefficient aminolysis considering the direct amine attack to the CyC, which is overtook by water effect acting as proton-relay. Nevertheless, water-catalyzed process is not efficient enough to overcome the low nucleophilic character of aniline, hence obtaining a kinetic barrier too high for ambient conditions.

Last but not least, CCSD(T) methods were used to validate DFT based methods in this system, proving the good accuracy-affordability compromise of DFT based methods, despite barriers were slightly underestimated in comparison to CCSD(T).

*"Nature works with five polymers.  
Only five polymers. In the natural  
world, life builds from the bottom up,  
and it builds in resilience and  
multiple uses." Janine Benyus*

# Chapter 5

## Polycarbonates

### 5.1 Introduction

The chemical fixation of carbon dioxide (CO<sub>2</sub>) to reduce the expulsion of CO<sub>2</sub> to the atmosphere may be accomplished by many chemical routes that need catalytic strategies to overcome the high kinetic and thermodynamic stability of CO<sub>2</sub>.<sup>[8, 69c, 69e]</sup> According to this goal, in this Thesis we presented a detailed study on the transformation of CO<sub>2</sub> to cyclic carbonates (CyC), which is a widely studied process in the community because its versatility and the high value of the obtained product.<sup>[71c, 79b, 80d, 84b]</sup> Nevertheless, the copolymerization of CO<sub>2</sub> with epoxides using similar catalysts and synthetic strategies than those used for CyC synthesis has been extensively investigated<sup>[29b, 30a, 30c, 120]</sup> because its importance in industrial processes to substitute phosgene, which is a toxic and hazardous reagent, for CO<sub>2</sub>.

Aliphatic polycarbonates formed from CO<sub>2</sub> and oxiranes are biodegradable and renewable polymers with useful properties that might become a potential alternative to conventional polymers. Moreover, the wide variety of epoxides that can be used in the copolymerization with CO<sub>2</sub> can lead to the formation of functionalized polycarbonates, which are used to build nanostructures or high value functionalized polymers from biorenewable substrates.<sup>[121]</sup>

Polycarbonates can be synthesized either from dienes or epoxides. Regarding diene copolymerization, the first process was based on lactone synthesis by telomerization of butadiene including CO<sub>2</sub> published by Braunstein in 1988.<sup>[122]</sup> The formation of a lactone may lead through Ring-Opening Polymerization (ROP) to the formation of alternating copolymers incorporating CO<sub>2</sub> to its structure.<sup>[120b]</sup> In this line, many authors have designed catalytically active Lewis acid complexes based on zinc,<sup>[123]</sup> sodium,<sup>[124]</sup> aluminum or titanium.<sup>[125]</sup> In addition, some examples of metal-free ROP processes have been investigated too.<sup>[126]</sup> One of the most relevant advances in the ROP of dienes and CO<sub>2</sub> was achieved by Nozaki et al. in 2014 using a mixture of two catalysts based on palladium and vanadium in a one-pot/two-step process where polycarbonate was formed directly from butadiene and CO<sub>2</sub> via a lactone intermediate.<sup>[126b]</sup>

On the other hand, polycarbonates can be formed by alternating copolymerization of epoxides and CO<sub>2</sub>, using similar catalytic systems as in CyC synthesis, and consequently, following similar reaction mechanisms to already presented in Chapter 3 of this Thesis.

In **Figure 5.1** we collected the most relevant catalytic systems for copolymerization between epoxides and CO<sub>2</sub>. As it can be seen in **Figure 5.1**, all catalysts have metals that present low electronic density, thus acting as Lewis acids that activate the epoxide and CO<sub>2</sub>. The first example of a metal-complex catalytically active towards CO<sub>2</sub> copolymerization with epoxides was reported by Inoue in 1986, which is an Al-metalloporphyrin complex that enabled the formation of polycarbonate from propylene oxide and CO<sub>2</sub>.<sup>[29b, 127]</sup>

After this achievement many other catalysts based on a metalloporphyrin-type structure but changing Al by other metals have been investigated.<sup>[23a, 25a, 128]</sup> Later on, the so called salen ligand, also used in CyC synthesis, is probably the most widely used ligand to design catalysts for polycarbonate formation from epoxides and CO<sub>2</sub>. Salen ligand is used in combination with many metals, but is usually combined with chromium or cobalt and present high catalytic activities and chemoselectivities.<sup>[129]</sup>

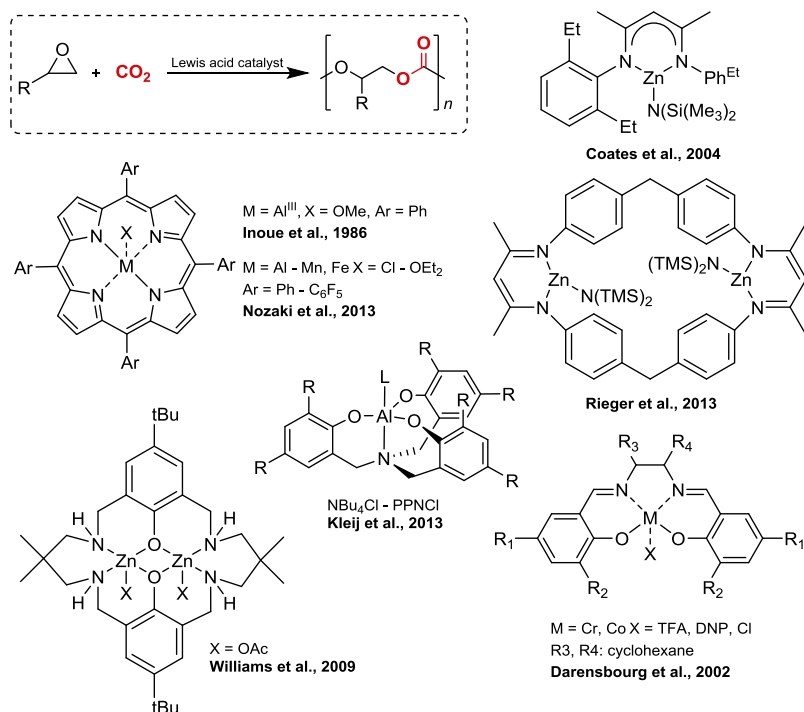


**Figure 5.1** Several reported catalysts for the copolymerization of epoxides and CO<sub>2</sub> to produce polycarbonates.

The reaction mechanism catalyzed by the Cr-salen system was reported by Darensbourg et al. in 2002<sup>[30b]</sup> and studied in detail by many authors considering several modifications in the catalyst structure, the used epoxide or the reaction conditions. Darensbourg and coworkers have exhaustively investigated the activity and selectivity of different salen complexes via the elucidation of the reaction mechanism using computational and experimental techniques.<sup>[99b, 130]</sup> In addition, they have

also contributed to study the variation in chemoselectivity when different epoxides are used.<sup>[131]</sup> In this line, Rieger et al. have investigated, from an experimental and computational point of view, the resulting selectivity and activity when a wide scope of epoxides are used,<sup>[132]</sup> focusing in the differences of propylene oxide and cyclohexene oxide (CHO),<sup>[133]</sup> which are the most commonly used epoxides in this process. Additionally, Nozaki et al. proposed a predictive method to estimate the performance of coordination complexes to be used as catalysts for propylene oxide copolymerization without the need of computing the TSs of the reaction mechanism.<sup>[134]</sup>

Many other catalysts have been used in copolymerization of epoxides and CO<sub>2</sub>, like Zn-azephenol by Wang et al.,<sup>[135]</sup> Cr-hydroxyquinoline by Müller et al.,<sup>[24b]</sup> Co-salicy by Coates et al.<sup>[136]</sup> or Co with a Schiff-base ligand by Niu et al.,<sup>[137]</sup> presenting all these structures very high catalytic activities. However, it is worth mentioning the remarkable results obtained using the combination of Zn with nitrogenated ligands. The dimeric Robson-type<sup>[138]</sup> complex used by Williams et al. showed extraordinary catalytic performance in the copolymerization of CHO and CO<sub>2</sub>.<sup>[26a]</sup> The reaction mechanism elucidated by Williams and Rzepa demonstrated that having two metal centers in the catalytic system is crucial to overcome the high kinetic barriers and consequently design efficient catalytic systems for CO<sub>2</sub> copolymerization. Having a bimetallic system, a pendulum-type mechanism is enhanced, where CO<sub>2</sub> and CHO monomers are incorporated sequentially to the copolymer chain.<sup>[35a]</sup> Williams and coworkers have also reported the synthesis of polyols from CHO and CO<sub>2</sub> using a Mg-based catalyst with similar structure to the presented in **Figure 5.1**.<sup>[27a]</sup>

Another example of highly active dimeric Zn-based catalyst is reported by Rieger et al. in 2013. Rieger and coworkers used a dimeric  $\beta$ -diketiminato zinc catalyst (see **Figure 5.1**) that presented the highest activity at the moment for the copolymerization of CHO and CO<sub>2</sub>.<sup>[139]</sup> Rieger and coworkers elucidated by means of DFT-based methods the



reaction mechanism using their dimeric Zn catalyst, which confirmed the pendulum-type mechanism reported by Williams et al. in 2012.<sup>[35b]</sup>

Some of the complexes catalytically active for CO<sub>2</sub> copolymerization with epoxides are also used in other copolymerization processes where different cyclic ethers in combination with lactones or cyclic anhydrides are used to perform alternating copolymerization reactions.<sup>[140]</sup> The β-diiminate zinc complex is an example of these systems that present high catalytic activity in multiple reactions regarding epoxide copolymerization.<sup>[120a]</sup> Coates et al. reported the high activity presented by β-diiminate Zn complex in the copolymerization of CO<sub>2</sub> with internal epoxides like CHO or limonene oxide.<sup>[141]</sup>

In our group, we have studied computationally the reaction mechanism of copolymerization of CO<sub>2</sub> with CHO<sup>[142]</sup> or LO<sup>[33b]</sup> catalyzed by the Al-aminotriphenolate complex [Al<sup>R</sup>] reported by Kleij et al. as highly active catalyst for CO<sub>2</sub> fixation with epoxides.<sup>[25b]</sup>

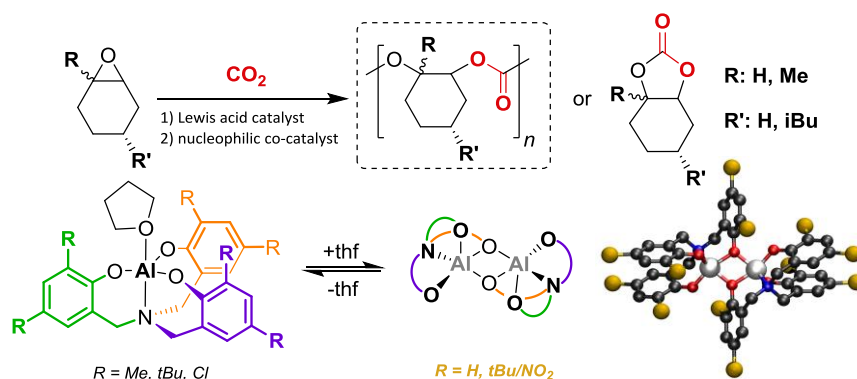


**Figure 5.2** Schematic representation of the reaction catalyzed by the Al-aminotriphenolate complex. The aromatic positions of the aminotriphenolate ligand may include different substituents in the ortho/para positions of the phenol, which may lead to the dimerization of the Al complex. A ball-and-stick model of the dimeric structure is depicted.

The well-known reaction mechanism for CyC synthesis from epoxides and CO<sub>2</sub> catalyzed by [Al<sup>R</sup>] facilitated us the elucidation of the reaction mechanism for polycarbonate formation using CHO and LO and

considering either mono- or bimetallic structures (see **Figure 5.2**). The reaction is catalyzed by the  $[Al^R]/PPNX$  binary system that presented high activity and selectivity in the experiments carried out by Kleij et al.

In this chapter, we divided our results in two parts, presenting first a general and exhaustive mechanistic study using CHO as epoxide and considering several mechanistic pathways. Noteworthy the Al-complex can dimerize *in situ* forming the first reported non-covalent dimeric structure that may present catalytic activity towards copolymerization of epoxides and  $CO_2$ . We also focused on the origin of the chemoselectivity by comparing the rate of CyC formation respect the copolymerization rate. Finally, we explore computationally two key modifications on the binary catalytic system to improve the catalytic efficiency for copolymerization reaction.

In the second part of this chapter we present our results for a particular reaction studied in collaboration with Kleij and coworkers. We elucidated the reaction mechanism of LO copolymerization with  $CO_2$  catalyzed by the  $[Al^{Me}]/PPNCl$  binary system. We focused on unraveling computationally the origin of the stereoselectivity. In addition, we have also compared the kinetic profile of the copolymerization of LO and  $CO_2$  with the limonene CyC formation mechanism.

### 5.1.1 Previous Mechanistic Studies

In our previous studies concerning the  $[Al^Cl]/TBAI$  (tetrabutylammonium iodide) mediated conversion of  $CO_2$  and epoxides to CyCs, we elucidated the reaction mechanism by using DFT-based methods. The first mechanistic steps of the CyC formation and the copolymerization reaction have found to be the same. These common steps, which are related to the epoxide ring-opening and the  $CO_2$  insertion have been highlighted in a dashed box in **Figure 5.3**, which showed below.

The reaction mechanism starts with the coordination of the epoxide to the axial position of the catalytic complex (after decoordination of THF).

This intermediate may not be the most stable assembly of the entire copolymerization mechanism, unlike CyC mechanism where the epoxide coordinated to  $[Al^R]$  is always the resting state of the reaction. The nucleophilic attack of a halide to open the epoxide towards an alkoxide moiety is identical to CyC mechanism, constituting a fast process because the high reactivity of both substrates and the stabilization of the formed alkoxide by the aluminum center.

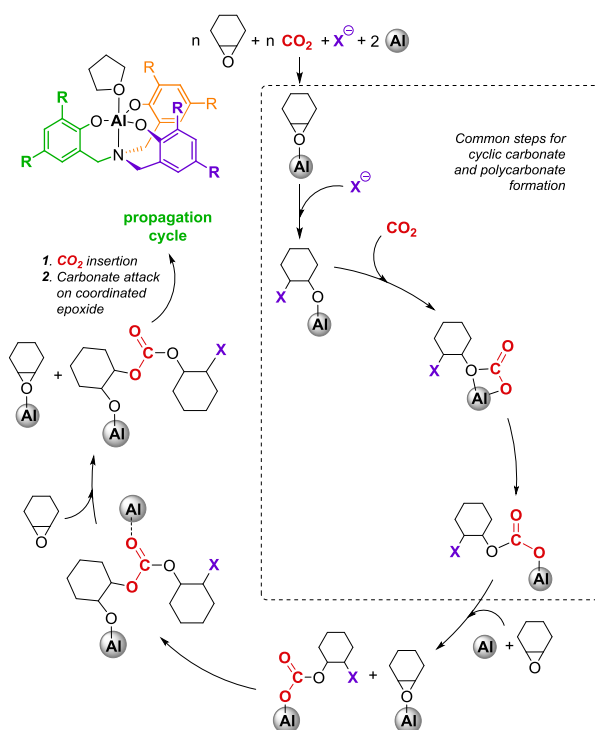


**Figure 5.3** Catalytic cycle for the ring-expansion addition of  $CO_2$  to epoxides catalyzed by Al-aminotriphenolate complex and co-catalyzed by a halide. All intermediates and transition states are illustrated. The steps in common between CyC and copolymerization mechanisms are collected within a dashed box.

The formation of the linear hemi-carbonate, firstly through  $CO_2$  insertion and secondly through isomerization, occurs identically to the CyC mechanism. In the next step lies the difference between CyCs and polycarbonates mechanisms. In CyC reaction mechanism the carbonyl

oxygen binds to the electrophilic carbon bonded to the halide, expelling the halide and constituting the ring-closing step. Alternatively, in the copolymerization reaction mechanism, the carbonate does not undergo intramolecular nucleophilic attack but intermolecular nucleophilic attack to a new epoxide forming an alkoxide.

This new epoxide may be coordinated to a second  $[Al^R]$  (bimetallic mechanism) or not (monometallic mechanism). After the new alkoxide is formed, the first  $[Al^R]$  initially bonded to the carbonate group is liberated, generating a coordinative vacancy in the Al center that will be saturated by a new epoxide. Therefore, the propagation step of copolymerization is constituted by two sub-steps:  $CO_2$  insertion to the alkoxide forming a carbonate, and after that, the nucleophilic attack of the carbonate to a new epoxide generating again an alkoxide moiety.

It is worth mentioning the different role of the halide in the copolymerization and the cyclic carbonate mechanisms. In CyC mechanism the halide was recovered after ring-closing step, hence acting as a co-catalyst of the reaction. Alternatively, in the copolymerization mechanism, the halide is included into the structure in the first step of the reaction where the epoxide is opened and remains in the same position during the propagation of the polymer chain. Consequently, the halide is the initiator of the polymerization process that facilitates the formation of the first alkoxide.

## 5.2 Mechanistic Study on Copolymerization Reactions

### 5.2.1 Goals and Motivation

The reaction mechanism for CHO copolymerization with CO<sub>2</sub> catalyzed by the [Al<sup>Cl</sup>]/TBAI was previously elucidated by our group.

The characterization of a non-covalent dimeric structure of the catalyst generated *in situ* in the reaction media, combined with the intrinsic complexity of copolymerization mechanisms prompted us to carry out a more exhaustive mechanistic study considering the non-covalent dimeric structure of the Al-aminotriphenolate complex as potential catalytically active species taking into account the previous studies carried out by Williams and Rzepa<sup>[35a]</sup> and Rieger.<sup>[35b]</sup>

Moreover, a detailed comparison between the Gibbs free-energy profiles of cyclic carbonates and copolymerization was an unresolved matter when identical systems were considered.

In addition, we aim to study the effect of changing the aromatic substituents of the aminotriphenolate ligand in the activity and selectivity of the catalytic system. We are also interested in describing the variation in the kinetics when changing the halide in the nucleophilic initiator.

Consequently, we present an exhaustive mechanistic study on the copolymerization reaction between CHO and CO<sub>2</sub> catalyzed by the binary catalytic system [Al<sup>Cl</sup>]/TBAI, which will be modified after elucidating the most feasible mechanism, to predict higher activity and selectivity.

### 5.2.2 Computational Details

All calculations in this study were performed by using the Gaussian 09 package.<sup>[86]</sup> The B97-D3 dispersion-corrected functional<sup>[87b, 97]</sup> was employed. The standard 6-311G(d,p) basis set<sup>[89]</sup> was used to describe the H, C, N and O atoms. The LANL2DZ<sup>[90]</sup> basis sets and associated

relativistic effective core pseudopotential were used for Al, Cl, and I atoms. Full geometry optimizations were performed without constraints. The nature of the encountered stationary points was characterized either as minima or transition states by means of harmonic vibrational frequencies analysis. Gibbs free-energies were calculated at standard conditions ( $T=298.15$  K,  $P=1$  atm).

Solvent effects were accounted for the gas-phase optimized structures by using the polarizable continuum model (PCM). Solvent effects have been included during the optimization of the structures using the PCM model in the last part of our results regarding the modification of the catalyst. The dielectric constant ( $\epsilon$ ) of the polarizable medium was set to the value reported for the simplest epoxide, ethylene oxide ( $\epsilon=12.42$ ),<sup>[91]</sup> as the reaction takes place in epoxide rich phase. Parameters for 1-hexanol were used for this purpose ( $\epsilon=12.51$ ), as implemented in the Gaussian09 package.

## 5.2.3 Results and Discussion

### 5.2.3.a Initiation of polymerization and CO<sub>2</sub> insertion

Herein, the reaction mechanism of copolymerization between CO<sub>2</sub> and CHO catalyzed by [Al<sup>Cl</sup>]/TBAI has been investigated. We first considered this binary catalytic system because we aimed to compare the new findings presented in this chapter with previous results obtained by our group regarding copolymerization of CHO and CO<sub>2</sub>. The first mechanistic steps of the CyC formation and the copolymerization reaction regarding ring-opening of CHO and CO<sub>2</sub> insertion have found to be the same (see **Figure 5.4**).

These first steps start with the coordination of CHO to [Al<sup>Cl</sup>] leading to a stable intermediate (**Int1**) with a relative free-energy of  $-16.5$  kcal·mol<sup>-1</sup>. After the formation of **Int1**, the nucleophilic initiator (TBAI) attacks the electrophilic carbon center of the epoxide through a ring-opening step, which leads to a metal alkoxide (**Int2**) that is more stable than the

previous intermediate by  $1.8 \text{ kcal}\cdot\text{mol}^{-1}$ . This process is the initiation step of the copolymerization, which has to overcome a transition state (**TS1**) that constitutes a Gibbs free-energy barrier of  $7.7 \text{ kcal}\cdot\text{mol}^{-1}$  computed from **Int1**.

After the initiation step, a  $\text{CO}_2$  molecule is inserted into the Al-O bond forming a chelating carbonate (**Int3**) bonded to the Al center with a relative free-energy of  $0.8 \text{ kcal}\cdot\text{mol}^{-1}$ . This step presents a relative barrier of  $21.1 \text{ kcal}\cdot\text{mol}^{-1}$ , since the computed Gibbs free-energy of **TS2** is  $2.8 \text{ kcal}\cdot\text{mol}^{-1}$ . As it occurs in CyC mechanism, the second part of the  $\text{CO}_2$  insertion is the isomerization of the chelate carbonate to form a linear hemi-carbonate (**Int4**) through a relatively high energy demanding transition state (**TS3** at  $11.3 \text{ kcal}\cdot\text{mol}^{-1}$ ). From **Int4** ( $-2.2 \text{ kcal}\cdot\text{mol}^{-1}$ ), different reaction pathways may emerge, which have been illustrated in **Figure 5.4**.

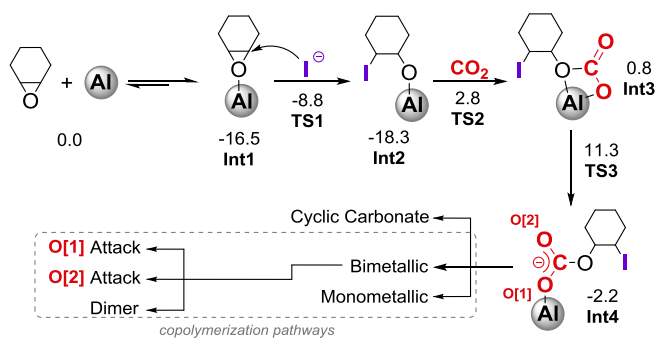


**Figure 5.4** Schematic representation of the reaction mechanism  $\text{CO}_2$  and CHO until the formation of the hemi-carbonate, which can go through several mechanistic possibilities.

On one hand, to produce cyclic carbonate the O[2] atom attacks the electrophilic carbon bonded to the iodide. On the other hand, the propagation of the polymer occurs by the nucleophilic attack of O[1] or O[2] to a new epoxide.

The copolymerization pathway can take place directly from **Int4** involving only one  $[\text{Al}^{\text{Cl}}]$  (monometallic mechanism) or two  $[\text{Al}^{\text{Cl}}]$  (bimetallic mechanism). Furthermore, in the case of a bimetallic

mechanism, both O[1] and O[2] oxygen atoms of the carbonate may be involved in the attack onto the second epoxide monomer.

An alternative mechanistic pathway is based on a dimeric species previously characterized by Kleij et al.,<sup>[80d,142]</sup> the potential catalytic activity of that arises from the dimerization of two  $[Al^{Cl}]$  through two  $\mu$ -oxo bridges. Therefore, we have computed the Gibbs free-energy profiles of all these mono- and bimetallic pathways.

### 5.2.3.b The propagation step through bimetallic mechanisms

Multiple reaction pathways may take place after **Int4**. In order to compare all of them, we present the Gibbs free-energy profiles of all the considered reaction mechanisms in **Figure 5.5** depicted below. Moreover, in **Figure 5.6** a detailed comparison between the bimetallic and dimeric mechanisms is illustrated.

As we explained in Chapter 3 of this Thesis, the reaction pathway related to the formation of CyCs (orange) goes through the nucleophilic attack of O[2] to the electrophilic carbon center bonded to the iodide. This step has to overcome a relative barrier of  $11.0 \text{ kcal}\cdot\text{mol}^{-1}$  associated to the difference between **Int4** ( $-2.2 \text{ kcal}\cdot\text{mol}^{-1}$ ) and **TS4-cc** ( $8.8 \text{ kcal}\cdot\text{mol}^{-1}$ ). Hereafter, a stable intermediate named **Int6-cc** is formed ( $-11.0 \text{ kcal}\cdot\text{mol}^{-1}$ ), which has the CyC still bonded to  $[Al^{Cl}]$  through O[1]. Finally, the product is released and a new CHO molecule coordinates to  $[Al^{Cl}]$ . This final step presents a relative free-energy of  $-16.5 \text{ kcal}\cdot\text{mol}^{-1}$ , which is effectively the Gibbs free-energy of the formation of the CyC ( $\Delta G_r$ ).

The least favorable copolymerization pathway is the monometallic mechanism (red profile in **Figure 5.5**) that has to overcome an absolute barrier of  $46.8 \text{ kcal}\cdot\text{mol}^{-1}$ . This mechanism starts with the coordination of CHO to a penta-coordinated Al species (**Int5-p**) occupying an equatorial coordination site, leading to an octahedral structure with a relative energy of  $0.8 \text{ kcal}\cdot\text{mol}^{-1}$ . Thus, the coordination of an extra epoxide to the already saturated coordination sphere of Al is not a favorable process. Then, the coordinated linear carbonate attacks the CHO through a transition state



(**TS4-p**), with a high relative barrier of 27.7 kcal·mol<sup>-1</sup> with respect to the intermediate **Int5-p**. Once passing through **TS5-p**, the obtained alkoxide coordinated to the equatorial position of the catalyst (**Int6-p**) has a relative free-energy of 3.8 kcal·mol<sup>-1</sup>.

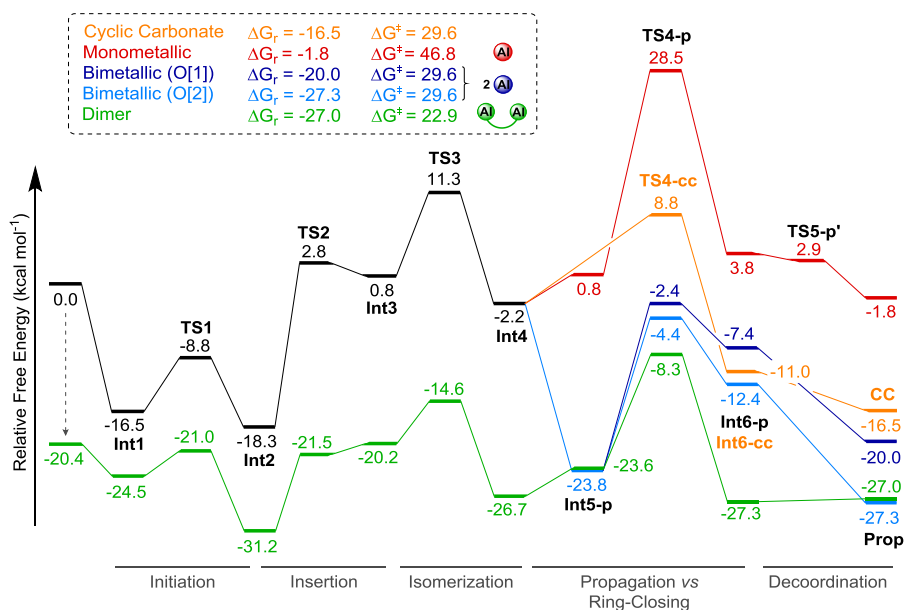


**Figure 5.5** Gibbs free-energy profiles for the four copolymerization mechanisms and the cyclic carbonate formation (orange trace). The copolymerization reaction catalyzed by one [Al<sup>Cl</sup>] is depicted in red after **Int3**. The dark and light blue traces refer to the propagation steps of the free-energy profiles for the different bimetallic mechanisms when O[1] and O[2] act as nucleophilic centers. The green profile represents the Gibbs free-energy pathway for the dimeric structure of [Al<sup>Cl</sup>].

The next step is a barrierless and exergonic isomerization through **TS6-p** (2.9 kcal·mol<sup>-1</sup>) to obtain an alkoxide coordinated to the axial position of [Al<sup>Cl</sup>] (-1.8 kcal·mol<sup>-1</sup>) that can continue propagation towards a polycarbonate by alternating CHO coordination and CO<sub>2</sub> insertion.

As an alternative to the monometallic mechanism, the second CHO monomer could be coordinated to an extra [Al<sup>Cl</sup>], the same way as occurs in **Int1**. Therefore, we have **Int1** and **Int4** together, constituting a stable intermediate named **Int5-p** (-23.8 kcal·mol<sup>-1</sup>). This would imply two aluminum complexes, one in the form of **Int1**, which activates a second

CHO molecule, and the other complex stabilizing the growing chain (**Int4**). This combination of events is related to a bimetallic mechanism similar to the bimetallic mechanism presented in glycidol carbonate (GC) formation in Chapter 3 where two oxygen centers had to be activated.

Once **Int5-p** is formed, both oxygen atoms of the carbonate group (O[1] and O[2], see **Figure 5.4**) can open the CHO monomer coordinated to the second  $[Al^{Cl}]$ . In case of O[1] attack, the **TS4-p** is  $2.0 \text{ kcal}\cdot\text{mol}^{-1}$  higher in energy ( $-2.4 \text{ kcal}\cdot\text{mol}^{-1}$ ) than the transition state obtained by O[2] attack ( $-4.4 \text{ kcal}\cdot\text{mol}^{-1}$ ). After **TS4-p**, a new alkoxide species is formed (**Int6-p**) having a relative free-energy of  $-7.4 \text{ kcal}\cdot\text{mol}^{-1}$  and  $-12.4 \text{ kcal}\cdot\text{mol}^{-1}$  for the O[1] and O[2] pathways, respectively.

The origin of the difference in stability between the nucleophilic attack through O[1] and O[2] relies in the larger steric hindrance generated by the aminotriphenolate ligand of  $[Al^{Cl}]$  in the pathway through O[1] attack, being the O[2] attack a more favorable process to open the CHO. After the alkoxide is formed, the first  $[Al^{Cl}]$  is separated from the carbonate group through a barrierless process that leads to an alkoxide bonded to a single  $[Al^{Cl}]$  (**Prop**).

In **Figure 5.6** it can be visualized that **Prop** is the active species that enables the continuation of the propagation cycle by the insertion of a new  $CO_2$  molecule forming a new carbonate moiety. The difference in stability between **Prop** intermediates of the two bimetallic pathways becomes even larger compared to the energy difference observed for **Int6-p**. The reason is the less hindered conformation of **Prop** for O[2] ( $-7.3 \text{ kcal}\cdot\text{mol}^{-1}$ ) route respect the O[1].

In addition to the bimetallic pathways presented above, there is yet another possible mechanistic description to the CHO/ $CO_2$  copolymerization process. This alternative route is made feasible by the formation of a non-covalent dimeric Al complex (**Figure 5.2**). This dimerization process occurs *in situ* and has been previously studied experimentally for aluminum and iron aminotriphenolate complexes.<sup>[25b]</sup>

The dimerization of  $[\text{Al}^{\text{Cl}}]$  is an exergonic process by  $-20.4 \text{ kcal}\cdot\text{mol}^{-1}$  (**Figure 5.5**), thus providing high stabilization with respect to two monomeric  $[\text{Al}^{\text{Cl}}]$ . Therefore, the energy reference of the dimeric profile is  $20.4 \text{ kcal}\cdot\text{mol}^{-1}$  lower than the zero set for the previous profiles. The spontaneous formation of this dimer can be a huge advantage in new catalyst design if it allows for an energetically more favorable copolymerization pathway. Therefore, we also computed the free-energy profile of this latter pathway represented in green in **Figure 5.5**.

The mechanistic steps for the dimer-mediated pathway are very similar to the already presented above for the bimetallic mechanism. First, a CHO molecule is bonded to the axial position of one of the two aluminum centers of the dimer forming **Int1** with a relative free-energy of  $-24.5 \text{ kcal}\cdot\text{mol}^{-1}$ . The epoxide ring-opening step is also similar, which is represented by **TS1** and has a low relative barrier of  $3.5 \text{ kcal}\cdot\text{mol}^{-1}$ . The structure of **TS1** evolves into **Int2**, constituting the most stable intermediate ( $-31.2 \text{ kcal}\cdot\text{mol}^{-1}$ ) of the entire reaction pathway. Once this alkoxide is generated, the  $\text{CO}_2$  insertion takes place through **TS2**, having a relative free-energy of  $-21.5 \text{ kcal}\cdot\text{mol}^{-1}$  establishing a relative Gibbs free-energy barrier of  $9.7 \text{ kcal}\cdot\text{mol}^{-1}$ .

The barrier for the  $\text{CO}_2$  insertion step is  $11.4 \text{ kcal}\cdot\text{mol}^{-1}$  lower than that computed in the bimetallic mechanism (black trace in **Figure 5.5**). Hence, the insertion process is much faster when considering the non-covalent dimer.

The next intermediate in the energy profile of the dimeric catalyst is a chelated carbonate, whose structure shows a slight structural difference with those of the other mechanisms where only one  $[\text{Al}^{\text{Cl}}]$  was present during the insertion of  $\text{CO}_2$  (see **Figure 5.6**). In the bimetallic cases where only one Al center was involved in the  $\text{CO}_2$  insertion, the chelated carbonate comprises two Al-O bonds involving the same Al center. Instead, in the **Int3** of the dimer-mediated mechanism one oxygen atom is bonded to each Al center, observing a stabilizing effect. After **Int3**, an isomerization process takes place with a relative free-energy (**TS3**) of

-14.6 kcal·mol<sup>-1</sup> resulting in a linear hemi-carbonate species (**Int4**) with a free-energy of -26.7 kcal·mol<sup>-1</sup>.

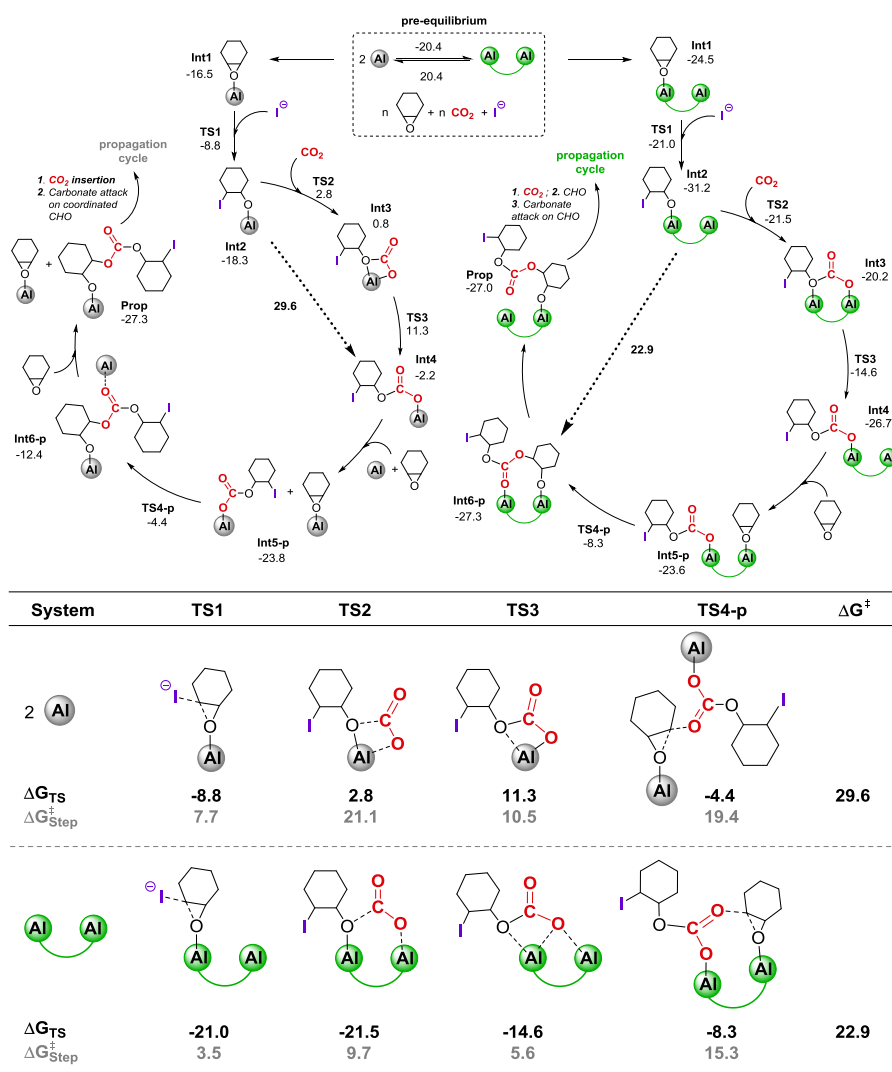


**Figure 5.6** Catalytic cycles showing the relative Gibbs free-energy values for the bimetallic and dimer-mediated copolymerization pathways. The absolute barrier of both the bimetallic (O[2] attack) and dimer-mediated pathway are shown in bold beside a dashed arrow connecting the most stable intermediate and the highest energy TS. The formation energy of the dimer is shown at the top in the pre-equilibrium box. Below, a table collecting all TSs and the respective relative barriers for each step of both mechanisms is presented.

The coordination of a new CHO monomer to the free Al center is endergonic (**Int5-p** at  $-23.6 \text{ kcal}\cdot\text{mol}^{-1}$ ) with respect to **Int4**. This pre-organization allows the carbonate to attack the coordinated CHO unit through **TS4-p** related to the propagation step of the process, which is the rate-determining step in this mechanism with a barrier of  $22.9 \text{ kcal}\cdot\text{mol}^{-1}$ , computed from **Int2**. The intermediate formed after **TS4-p** (**Int6-p**) with each oxygen atom of the carbonate and epoxide moieties bonded to each Al of the dimer has a relative free-energy of  $-27.3 \text{ kcal}\cdot\text{mol}^{-1}$ .

Afterward, the alkoxide (**Prop** at  $-27.0 \text{ kcal}\cdot\text{mol}^{-1}$ ) is finally generated and the propagation cycle can continue through repeating  $\text{CO}_2$  insertion, the coordination of a new CHO monomer to the other Al center and attack of the linear carbonate onto the activated CHO monomer.

The lowest absolute barrier is found in the dimeric mechanism with a value of  $22.9 \text{ kcal}\cdot\text{mol}^{-1}$ , and the only mechanism that seems unlikely is the monometallic one since the absolute barrier is too high ( $46.8 \text{ kcal}\cdot\text{mol}^{-1}$ ). The key transition states, their relative energies and relative barriers with respect to the preceding intermediates are collected in a table in the lower part of **Figure 5.6** for both the bimetallic (O[2] pathway) and the dimer-mediated copolymerization mechanisms. These mechanisms appear to be very similar, but the dimer-mediated pathway shows significantly lower relative barriers (see **Figure 5.7**).

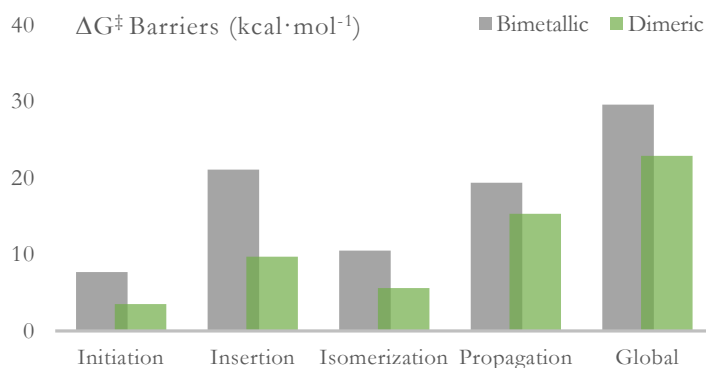


**Figure 5.7** Relative and absolute Gibbs free-energy barriers for the bimetallic (gray) and dimer-mediated (green) mechanisms.

The absolute barrier of the dimeric mechanism, up to formation of the intermediate **Prop** that is the starting point for further propagation, is 6.7 kcal·mol<sup>-1</sup> lower than the bimetallic one. Additionally, all the relative barriers are also significantly lower, particularly the CO<sub>2</sub> insertion. Thus, the copolymerization catalyzed by the dimeric complex is favored over the bimetallic one.

### 5.2.3.c Evaluation of the catalytic activity via modification of the ligand

After having determined that the dimeric species enables the copolymerization of CHO and CO<sub>2</sub> most efficiently than two separated [Al<sup>Ct</sup>], we explored the effect of several variations in the structure of the binary catalytic system. Our efforts focused on two variables: the peripheral substituents of the aminotriphenolate ligand and the type of halide used as nucleophilic agent. We chose different aromatic substituents and nucleophiles, which were used in other studies by Kleij et al.

The obtained reaction free-energy profiles are collected in **Figure 5.8**, in which the results for the system already calculated ([Al<sup>Ct</sup>]/TBAI) are the reference profile (green trace). However, for these calculations we have included the solvent effects in the geometry optimization of the structures. Therefore, the results for the reference profile in **Figure 5.8** are different from the results presented in **Figure 5.5**. Moreover, in **Figure 5.8** the dimeric structure of [Al<sup>R</sup>], in conjunction with all the other actors of the reaction, are considered in the energy zero. Consequently, all Gibbs free-energy values are shifted approximately twenty kcal·mol<sup>-1</sup> upwards.

The highest free-energy profile depicted in purple corresponds to the pathway using the [Al<sup>M<sub>c</sub></sup>]/TBAI binary catalyst, where both the most stable intermediate (**Int2**) and the highest transition state structures (**TS4-p**) are found to be the same as those computed for the reference profile. The copolymerization pathway mediated by [Al<sup>M<sub>c</sub></sup>]/TBAI is endergonic

by  $12.5 \text{ kcal}\cdot\text{mol}^{-1}$  (non-spontaneous) and the absolute barrier of this pathway is the highest observed ( $34.1 \text{ kcal}\cdot\text{mol}^{-1}$ ) being  $14.0 \text{ kcal}\cdot\text{mol}^{-1}$  higher than observed for the reference system  $[\text{Al}^{\text{Cl}}]/\text{TBAI}$  ( $20.1 \text{ kcal}\cdot\text{mol}^{-1}$ ). This means that the catalytic system  $[\text{Al}^{\text{Me}}]/\text{TBAI}$  is the least efficient among the five considered here.

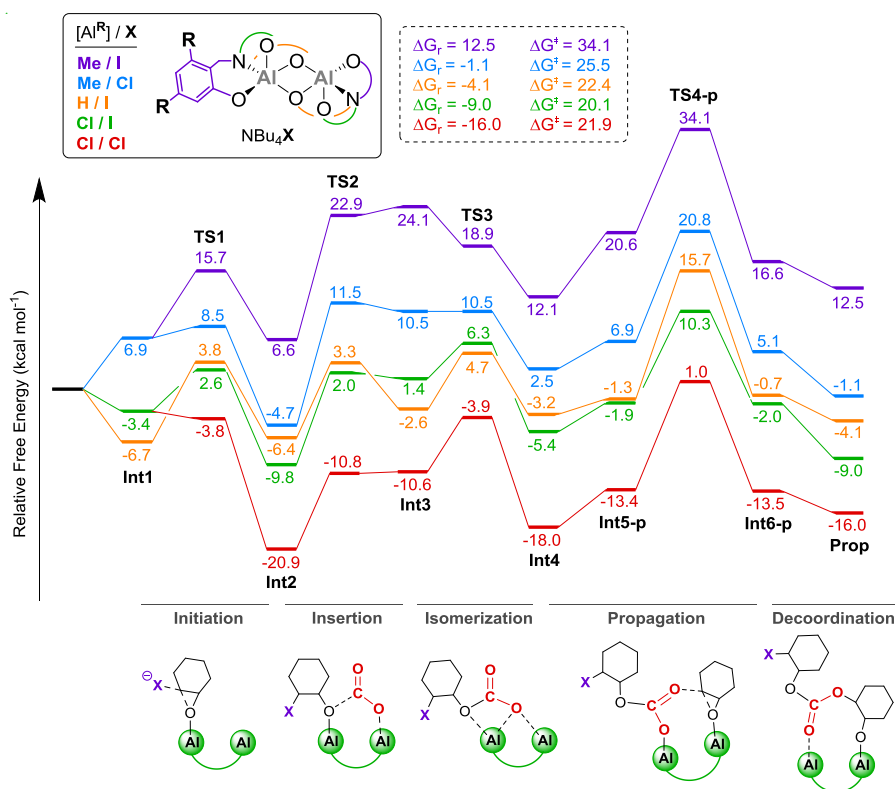


**Figure 5.8** Gibbs free-energy profiles for the copolymerization reaction of CHO and  $\text{CO}_2$  catalyzed by binary catalysts derived from  $[\text{Al}^{\text{R}}]$  and either using TBACl or TBAI as nucleophilic additive. Schematic representations of the TS structures related to all steps of the mechanism are shown below.

For the binary system composed of  $[\text{Al}^{\text{Me}}]/\text{TBACl}$ , similar trends to the previous case are observed but with lower relative free-energies for intermediates and TSs. The absolute barrier compared to the reference system  $[\text{Al}^{\text{Cl}}]/\text{TBAI}$  is moderately higher by  $5.4 \text{ kcal}\cdot\text{mol}^{-1}$ , but much lower than for the  $[\text{Al}^{\text{Me}}]/\text{TBAI}$  catalyst (25.5 versus  $34.1 \text{ kcal}\cdot\text{mol}^{-1}$ ). The reaction free-energy also decreases with respect to the  $[\text{Al}^{\text{Me}}]/\text{TBAI}$  by

13.6 kcal·mol<sup>-1</sup> but higher than noted for the reference catalyst by 7.9 kcal·mol<sup>-1</sup>. Therefore, when considering electron-donating methyl groups in [Al<sup>R</sup>] ligands, the copolymerization efficiency of the binary catalyst decreases. On the other hand, when considering the same peripheral substituents but different halide (iodide vs chloride), we observe a higher stabilization of the growing chain when a worse leaving group like chloride is considered. Additionally, a good leaving group like iodide favors the cyclic carbonate formation path because the ring-closing step is enhanced.

Replacing the methyl groups for hydrogen atoms ([Al<sup>H</sup>]) maintaining iodide as nucleophile (TBAI) gives a binary system with slightly higher absolute barrier (2.3 kcal·mol<sup>-1</sup>) and a Gibbs free-energy reaction 4.9 kcal·mol<sup>-1</sup> higher than computed for the reference system [Al<sup>Cl</sup>]/TBAI.

The [Al<sup>Cl</sup>]/TBACl catalyst system shows the lowest relative energy values, which suggests that it should be the most efficient binary combination. However, the absolute barrier is slightly higher than the reference system by 1.8 kcal·mol<sup>-1</sup> but, on the other hand, the reaction free-energy (-16.0 kcal·mol<sup>-1</sup>) is 7.0 kcal·mol<sup>-1</sup> lower. Hence, while the kinetic resistance observed for the catalyst [Al<sup>Cl</sup>]/TBACl is comparable to the reference, the thermodynamic driving force is more significant, making [Al<sup>Cl</sup>]/TBACl combination the most efficient binary catalyst for CHO/CO<sub>2</sub> copolymerization among the investigated systems.

## 5.2.4 Conclusions

In this study we have analyzed several possible reaction mechanisms for the copolymerization reaction of CHO and CO<sub>2</sub>, catalyzed by binary [Al<sup>R</sup>]/TBAX systems. The mechanism involving a dimeric [Al<sup>R</sup>]<sub>2</sub> species, which is able to be formed *in situ* in the reaction media, was found to give the most efficient copolymerization route among all the mono-metallic and bimetallic mechanistic routes. This complex is the first non-covalent bimetallic complex catalytically active for the copolymerization reaction between epoxides and CO<sub>2</sub>. This dimeric complex facilitates the



formation of an initial carbonate complex through relative low energetic barriers and faster overall reaction rates compared to the other bimetallic pathways. The computed mechanism involving this dimer species is compatible with the chemoselectivity of the process towards polycarbonate, since is kinetically and thermodynamically favored over the cyclic carbonate pathway.

The effects of the substituents in the ligand and the nucleophile on the catalytic activity were analyzed, showing that the electron-withdrawing groups in the aminotriphenolate ligand ( $\text{Al}^{\text{R}}$ :  $\text{R} = \text{Cl}$ ) increase the Lewis acidity of the Al complex and the potential to activate the epoxide. On the other hand, when using nucleophiles with poorer leaving group character, the stability of the formed carbonate species (**Int5-p**) increases, enhancing the probability of the attack onto a coordinated CHO monomer to the second Al center, and increasing the stability of the resultant alkoxide. The use of TBACl also decreases the probability of CyC formation. The intramolecular ring-closing of the carbonate group is suppressed, in line with the good chemoselectivity towards the copolymer observed experimentally when chloride is used.

## 5.3 Origin of the Stereoregularity of Poly(limonene)-carbonate

### 5.3.1 Goals and Motivation

In this section of the Thesis we aim to study the reaction mechanism of copolymerization between CO<sub>2</sub> and limonene oxide (LO) catalyzed by the [Al<sup>Me</sup>]/PPNX binary system.

Limonene oxide, which is the monomer of the copolymerization reaction, presents several stereocenters in its structure, which leads to multiple routes obtaining different conformations of the produced polycarbonate. Therefore, the main goal that we set in this study is determining the stereoselectivity of the copolymerization process analyzing key steps in the course of the reaction mechanism.

The nucleophilic attack to the epoxide can occur on two different carbon centers of the epoxide, inverting the conformation when a stereogenic center is attacked. However, the stereoselectivity determining part of the copolymerization is the propagation step. Consequently, we will study exhaustively the thermodynamic stability of the formed growing-chain and the kinetic barriers of the propagation process in order to determine the most plausible conformations.

### 5.3.2 Computational Details

All calculations were carried out by using the Gaussian 09 package.<sup>[86]</sup> The B97D3<sup>[97]</sup> functional was employed, which includes empirical dispersion energy corrections as introduced by Grimme.<sup>[87b]</sup> The standard 6-311G(d,p) basis set was used to describe the H, C, N and O atoms.<sup>[89]</sup> The relativistic effective core pseudo potential LANL2DZ<sup>[90]</sup> was used for Al, Br and Cl atoms together with its associated basis set. Full geometry optimizations were performed without constrains. All stationary points were characterized either as minima or transition states by means of harmonic vibrational frequencies analysis. Gibbs free-energies were

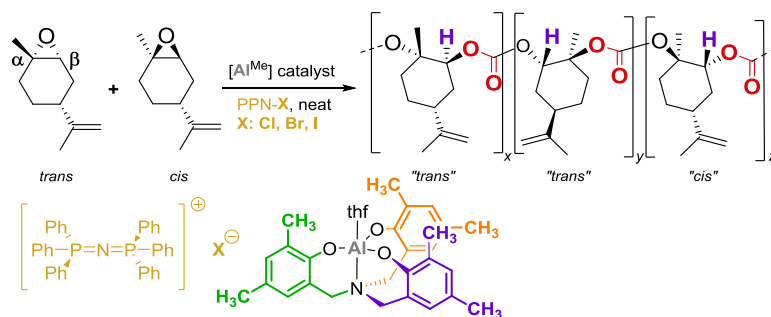
calculated at standard conditions ( $T=298.15$  K,  $P=1$  atm). In order to introduce solvent effects, single point calculations were performed on the gas-phase optimized structures by using the polarizable continuum model (PCM). The dielectric constant ( $\epsilon$ ) of the polarizable medium was set to the value reported for the simplest epoxide, ethylene oxide ( $\epsilon=12.42$ )<sup>[91]</sup> as the reaction takes place in the limonene oxide rich phase. The 1-hexanol solvent was used for this purpose ( $\epsilon=12.51$ ), as implemented in Gaussian.

### 5.3.3 Results and Discussion

#### 5.3.3.a The effect of the nucleophile in the initiation step

The copolymerization reaction of  $\text{CO}_2$  and LO presented in this section is an interesting process from an environmental, economic and academic perspective. First, the used monomers for the copolymerization reaction are  $\text{CO}_2$  and LO, which both can be obtained from renewable routes. Limonene oxide is produced from the oxidation of limonene, which is a natural terpene extracted from citric fruits.<sup>[143]</sup> Additionally, both substrates and the catalytic system are cheap and easily accessible. Last but not least, LO presents a complex structure with three different chiral centers. As it can be seen below in **Figure 5.9**, the epoxide group of LO has two differently substituted carbon centers, a methyl-substituted ( $\alpha$ ) and a hydrogen-substituted ( $\beta$ ). Noteworthy, when the  $\alpha$ -carbon undergoes nucleophilic attack by PPNX, through a  $\text{S}_{\text{N}}2$ -type route, the *cis/trans* conformation respect the isobutylene group is inverted from *trans* to *cis* and vice versa.

As we introduced in section 5.1.2, the copolymerization mechanism starts similarly to the CyC formation via the nucleophilic attack of a co-catalyst (in copolymerization named initiator) to convert the epoxide to an alkoxide.

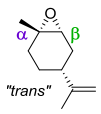
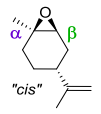


**Figure 5.9** Schematic structures of the (R)-LO *trans* and *cis* isomers, the initiator PPN-X and the aminotriphenolate metal complex  $[Al^{Me}]$  used in this work. A schematic model of the obtained copolymer is also included to show different *trans/cis* like conformations.

The ring opening of the *trans* and *cis* (R)-LO was first evaluated using chloride or bromide as nucleophiles (see **Table 5.1**). This ring-opening step involves a concerted transition state (**TS1** in **Figure 5.10**) characterized by the breaking of the  $C_{\alpha\beta}$ -O epoxide bond and the simultaneous formation of a  $C_{\alpha\beta}$ -Cl/Br, leading to the formation of an alkoxide intermediate (**Int2**). The nucleophilic attack can occur at the  $\alpha$  carbon (most substituted carbon) or the  $\beta$  carbon (least substituted carbon) atoms of the *cis/trans* LO, and therefore eight possible ways of epoxide ring-opening should be considered. The fourth and fifth columns of **Table 5.1** collect the relative Gibbs free-energy barriers calculated for this step.

Consequently, the nucleophile is crucial to determine the regioselectivity of the initiation step, since two different active carbon centers are present in the epoxide moiety. When  $\beta$ -carbon is attacked, the conformation of the alkoxide would be the same that previous to the ring-opening. Alternatively, if nucleophilic attack to  $\alpha$ -carbon is preferred over the  $\beta$  one, the obtained moiety would undergo inversion of configuration.

**Table 5.1** NBO population analysis for  $\alpha$  and  $\beta$  carbon atoms of LO. The charge of both centers is shown when LO is bonded to  $[Al^{Me}]$  (in parenthesis) and when is free. The activation Gibbs free-energies (in  $\text{kcal}\cdot\text{mol}^{-1}$ ) for the epoxide ring-opening step using chloride and bromide are showed in the last column.

Substrate	Carbon	NBO population analysis	TS ring-opening	
			Cl <sup>-</sup>	Br <sup>-</sup>
 "trans"	$\alpha$	0.27 (0.31)	2.8	8.9
	$\beta$	0.10 (0.12)	4.7	10.2
 "cis"	$\alpha$	0.27 (0.31)	0.7	6.1
	$\beta$	0.11 (0.13)	3.8	9.1

In general, the relative barriers for the nucleophilic attack when chloride anion is considered are much lower than those obtained for the bromide attack. In all the cases, the  $\alpha$  attack is favored over the  $\beta$  one, as supported by the NBO population analysis included in **Table 5.1**, which shows higher electrophilic character for the most substituted carbon center. It is commonly thought that the most substituted carbon ( $\alpha$ ) is less reactive than the least hindered because of the electronic and steric effects induced by the methyl group. In contrast, the  $\alpha$  attack was found to be more feasible, with the *cis* conformation being the preferred way over the *trans* substrate by  $2.1 \text{ kcal}\cdot\text{mol}^{-1}$ . Alternatively, for the  $\beta$  attack, this energy difference is less marked ( $0.9 \text{ kcal}\cdot\text{mol}^{-1}$ ) although the *cis* isomer still remains favored over the *trans*. Because of the better results obtained using chloride, this species was selected as initiator for the alternating copolymerization, and thus decreasing the number of possible pathways to study.

### 5.3.3.b Insertion of $\text{CO}_2$ and ring-closing to LO-CyC

In **Figure 5.10**, we illustrate the Gibbs free-energy profiles for the  $[Al^{Me}]/\text{Cl}$  catalyzed initiation of the copolymerization of *cis/trans*-(R)-LO and  $\text{CO}_2$ , taking into account the nucleophilic attack by chloride on  $\alpha$  and

$\beta$  positions of both epoxides. In addition, the insertion of  $\text{CO}_2$  and the following cyclization of the carbonate are also included in the profile, in order to compare the relative and absolute barriers of cyclization mechanism and the copolymerization mechanism.

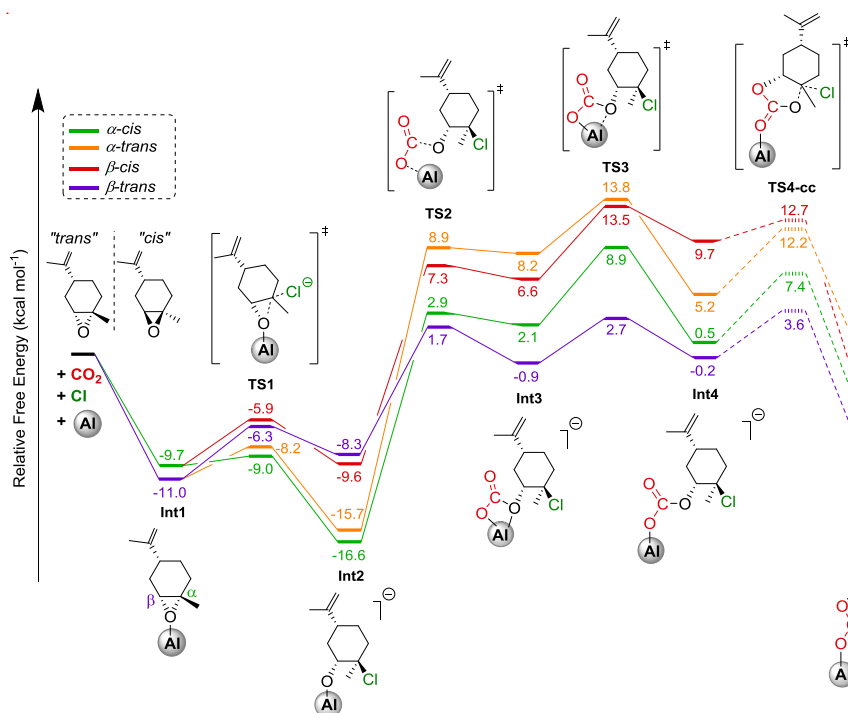


**Figure 5.10** Gibbs free-energy profiles for the copolymerization reaction of *cis/trans*-LO and  $\text{CO}_2$  catalyzed by  $[\text{Al}^{\text{Me}}]$  and initiated by PPNCl. The CyC reaction mechanism is shown in dashed lines after **Int4**. Schematic representations of the intermediates and TS structures related all steps of the  $\alpha$ -*trans* mechanism are shown.

First, LO is coordinated to the Al center of  $[\text{Al}^{\text{Me}}]$ , activating the epoxide and yielding to two different **Int1** (*cis* and *trans*). This process is exergonic by  $9.7 \text{ kcal}\cdot\text{mol}^{-1}$  for the *cis*-coordinated (green line) complex and  $11.0 \text{ kcal}\cdot\text{mol}^{-1}$  for the *trans* one (purple line), showing a slight preference towards the formation of the *trans* **Int1**.

The ring-opening step leads to formation of the alkoxide **Int2**. It can be observed that the intermediates obtained by nucleophilic attack on the  $\alpha$  position (green and orange lines) are energetically more stable than those

involving the  $\beta$  attack because the  $\alpha$  carbon is more electrophilic than the  $\beta$  one, as explained before by the NBO population analysis collected in **Table 5.1**. It is worth noting that the  $\alpha$  carbon is a stereogenic center, thus the nucleophilic attack of chloride on this carbon center evolves with inversion of configuration. Hence, the *cis*-coordinated epoxide evolves into the most stable *trans*-product **Int2** (trace in green) and the *trans* substrate is converted into the *cis* intermediate (trace in orange). For the  $\beta$  attack, retention of configuration occurs because the nucleophilic attack does not involve a stereocenter.

After epoxide ring-opening by chloride, CO<sub>2</sub> is inserted into the Al-O alkoxide bond of **Int2** via transition state **TS2**. The intermolecular CO<sub>2</sub> insertion was located to be less energetically demanding for the  $\beta$ -*trans* and  $\alpha$ -*cis* pathways, with relative Gibbs free-energy values for **TS2** of 1.7 and 2.9 kcal·mol<sup>-1</sup>, respectively. Nevertheless,  $\beta$ -*trans* and  $\alpha$ -*cis* relative barriers depend on the stabilization of **Int2**, hence obtaining relative barriers of 10.0 and 19.5 kcal·mol<sup>-1</sup>, respectively. The highest barrier was calculated for the  $\alpha$ -*trans* pathway, having an activation energy of 24.6 kcal·mol<sup>-1</sup>.

The CO<sub>2</sub> insertion step leads to the chelate carbonate **Int3**, which is coordinated by two oxygen atoms to the Al center. This intermediate follows the same stability trend as the preceding **TS2**, and could suffer isomerization (through **TS3**) to form the linear hemi-carbonate **Int4**. In this case, the  $\beta$ -*trans* and  $\alpha$ -*cis* pathways still lead to the most stable intermediates. The isomerization of **Int3** is rate-determining for the  $\alpha$ -*trans*,  $\beta$ -*cis* and  $\alpha$ -*cis* profiles, with activation barriers (calculated from the Int2) of 29.5, 23.1 and 25.5 kcal·mol<sup>-1</sup>, respectively. In the case of the  $\beta$ -*trans* profile, this is valid if the reaction is evaluated only until the formation of **Int4** (rather than taking into account the subsequent backbiting reaction) involving an activation barrier of 13.7 kcal·mol<sup>-1</sup>, which is calculated from the most stable state (**Int1**).

When **Int4** is formed, two possible routes can be followed by this intermediate. On one side, the hemi-carbonate oxygen of **Int4** can attack the electrophilic carbon bonded to chloride (backbiting step) to produce the already known CyC, which is the undesired product in this case. On the other side, the consecutive addition of new epoxide and CO<sub>2</sub> monomers lead to the formation of polycarbonate through the propagation step. The backbiting step shown in **Figure 5.10** goes through **TS4-cc**, leading to the CyC already coordinated to [Al<sup>Me</sup>] (**Int5-cc**). This step requires slightly lower barriers than the involved in the isomerization reaction, with the  $\beta$ -*trans* profile being the only exception with a relative barrier of 3.8 kcal·mol<sup>-1</sup>. The alternating propagation reaction is separately discussed in the next section where we will explain why there is a preference for polycarbonate from LO and CO<sub>2</sub> catalyzed by [Al<sup>Me</sup>]/PPNCl.

### 5.3.3.c Propagation of the LO-CO<sub>2</sub> copolymer

Once the linear hemi-carbonate **Int4** is formed in the initiation process, several propagation routes can be followed. The carbonyl oxygen of the four resulting **Int4** species acts as nucleophile attacking two different epoxides (*cis* or *trans*) on two different carbon atoms ( $\alpha$  or  $\beta$ ). This situation generates sixteen possible profiles to investigate. In order to decrease the computational efforts, we decided to study the most feasible pathways, based on the previous results on the initiation step.

Therefore, the number of pathways was reduced to four by considering the attack by the most stable hemi-carbonates ( $\alpha$ -*cis* and  $\beta$ -*trans*) on the  $\alpha$  carbon of the *cis* and *trans* epoxides. The Gibbs free-energy profiles for the alternating propagation step of *cis/trans*-(R)-LO and CO<sub>2</sub>, taking into account the previous considerations, are illustrated in **Figure 5.11**.

The propagation process, as we proved in the previous section and other groups have also reported, requires two aluminum centers (bimetallic mechanism) to be feasible.<sup>[35]</sup>



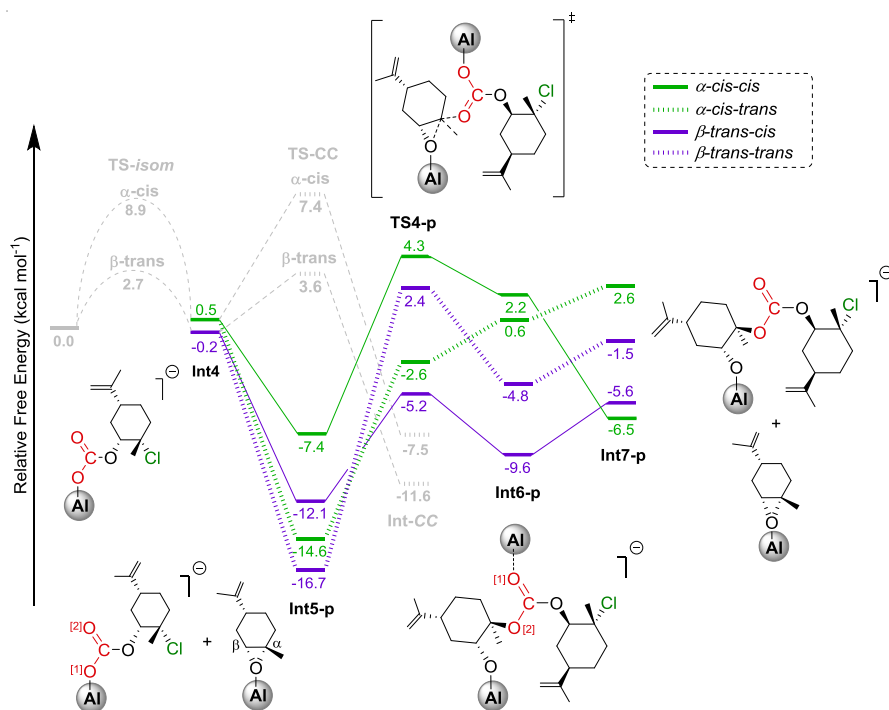


**Figure 5.11** Gibbs free-energy profiles for the propagation step of the copolymerization reaction of  $\alpha$ -*cis* (green lines) and  $\beta$ -*trans* (purple lines) routes, catalyzed by  $[Al^{Me}]$  and initiated by PPNCl. Both *cis* (solid lines) and *trans* (dashed lines) epoxides were considered as monomers in the propagation process. Schematic representations of the intermediates and TS structures related to all steps of the  $\alpha$ -*cis*-*trans* mechanism (green dashed line) are shown.

In this reaction, it can be firstly observed the formation of a very stable ensemble (**Int5-p**) between **Int4** and the complex having a new epoxide substrate coordinated to another  $[Al^{Me}]$  (**Int1**). Natural bond orbital (NBO) population analysis on this complex shows small difference in the value of the charge assigned to the oxygen atoms of the carbonate group of **Int4**. The oxygen atom labeled O[1] bound to the Al center in **Figure 5.11** exhibits a charge of -0.83; whereas for the carbonyl oxygen (O[2]), a value of -0.69 was obtained. Although the oxygen O[1] is slightly more nucleophilic than the carbonyl oxygen O[2], when the reaction goes through O[1] leads to higher barriers of the free-energy profile (see **Figure 5.12** in page 135).

This stabilization of O[2] attack over O[1] is due to a less steric hindrance between the **Int1** and **Int4** moieties that constitute **Int5-p** and **TS4-p**. When O[1] is considered the two  $[Al^{Me}]$  are closer, obstructing the nucleophilic attack of the carbonate to the epoxide.

In all cases, lower relative energy values were found between the formed **Int5-p** and the transition state of the backbiting reaction (**TS4-cc**; **Figure 5.10** and grey traces in **Figure 5.11**). For instance, the resulting **Int5-p** from  $\alpha$ -*cis* **Int4** considering both *cis* and *trans* LO ( $\alpha$ -*cis-cis* and  $\alpha$ -*cis-trans* in **Figure 5.10**) were found to be more stable than their corresponding **TS4-cc** ( $7.4 \text{ kcal}\cdot\text{mol}^{-1}$ ) by 14.8 and 22.0  $\text{kcal}\cdot\text{mol}^{-1}$ , respectively. In the case of the  $\beta$ -*trans* **Int4** forming an initial ensemble with each coordinated substrate attached to a second  $[Al^{Me}]$ , this energy difference becomes 15.7  $\text{kcal}\cdot\text{mol}^{-1}$  combining with the *cis*-epoxide ( $\alpha$ -*trans-cis*) and 20.3  $\text{kcal}\cdot\text{mol}^{-1}$  with the *trans* one ( $\alpha$ -*trans-trans*).

Following the reaction coordinate, the next step is the epoxide ring-opening, which is undertaken by nucleophilic attack of the carbonyl oxygen labeled O[2] on the most substituted carbon ( $\alpha$ ) of each epoxide isomer (*trans* or *cis*) bound to  $[Al^{Me}]$  in **Int5-p**. Similar as for the initiation process, in the propagation reaction the epoxide ring-opening is characterized by a concerted transition state **TS4-p**. The  $\alpha$ -*cis-cis* profile shows the highest activation barrier being 20.9  $\text{kcal}\cdot\text{mol}^{-1}$  (having a relative energy of 4.3  $\text{kcal}\cdot\text{mol}^{-1}$ ), calculated from the most stable intermediate of the initiation process **Int2** with a relative energy of -16.6  $\text{kcal}\cdot\text{mol}^{-1}$  (see **Figure 5.10**). In contrast, the **TS4-p** for the  $\beta$ -*trans-cis* pathway involves an activation barrier of only 6.9  $\text{kcal}\cdot\text{mol}^{-1}$  (calculated from **Int5-p**). In the case of the  $\beta$ -*trans-trans* and  $\alpha$ -*cis-trans* profiles, these barriers were obtained in a similar way as described for the previous pathways, and lead to values of 19.1 and 14.0  $\text{kcal}\cdot\text{mol}^{-1}$ , respectively.

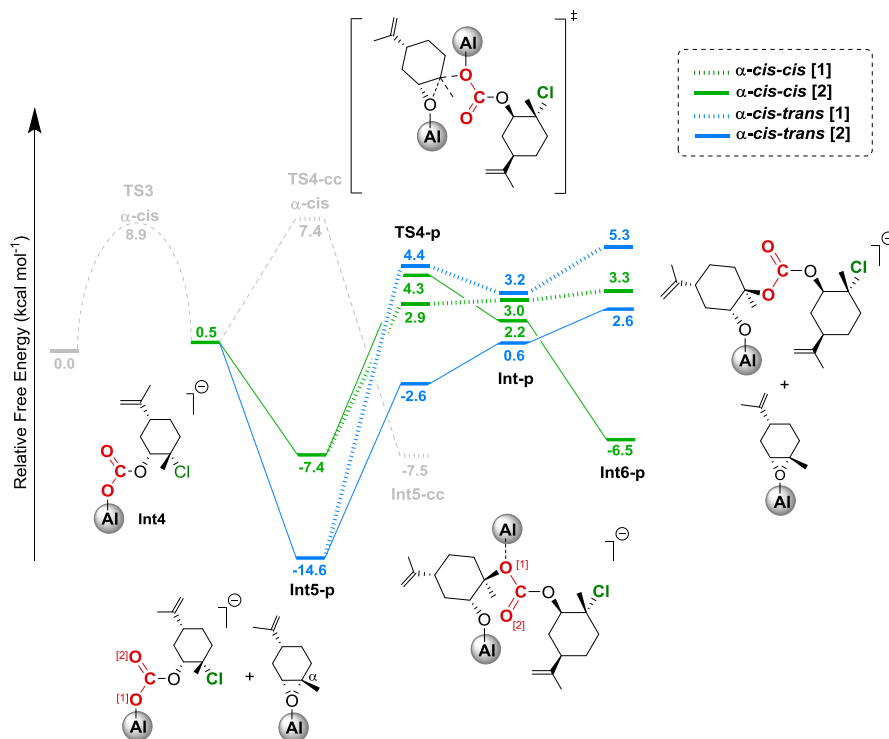


**Figure 5.12** Gibbs free-energy profiles for the propagation step of the copolymerization reaction of  $\alpha$ -*cis* moiety catalyzed by  $[Al^{Me}]$  and initiated by PPNCl. Both *cis* (green lines) and *trans* (blue lines) epoxides were considered as monomers in the propagation process. A comparative of the relative Gibbs free-energy considering both O[1] (dashed lines) and O[2] (solid lines) is illustrated. Schematic representations of the intermediates and TS structures related all steps of the  $\alpha$ -*cis-trans* [1] mechanism (blue dashed line) are shown.

After passing through the **TS4-p** barrier, the formation of the intermediate **Int5-p** occurs. This intermediate has both  $[Al^{Me}]$  still coordinated. However, the strength of interaction between the oxygen from the alkoxide moiety and the Al center is much stronger than that observed for the oxygen O[1] of the coordinated carbonate and the Al center from **Int4**. Hence, it is proposed that **Int5-p** can evolve into **Int6-p** by releasing the Al complex from the carbonate and allowing for coordination of a new *trans*-(R)-LO monomer to the generated coordinative vacancy. This reaction is endergonic by 2.6 kcal·mol<sup>-1</sup> for the  $\alpha$ -*cis-trans* profile. The remaining processes are slightly exergonic, with a

release of -1.5, -5.6 and -6.5 kcal·mol<sup>-1</sup> in the case of the  $\beta$ -*trans-trans*,  $\beta$ -*trans-cis* and  $\alpha$ -*cis-cis* pathways, respectively. Interestingly, both the energetically most stable **Int6-p** resulting from the  $\beta$ -*trans-cis* and  $\alpha$ -*cis-cis* profiles will contain exclusively *trans* units in the growing chain, which is in line with the experimental findings. The current catalytic process based on [Al<sup>Me</sup>]/PPNCl shows two main features. First, a clear preference for the faster conversion of *cis*-LO, and secondly, the resulting copolymers contain a significant higher amount of *trans* versus *cis* units (up to 98:2 in the experimental results) where the use of pure *cis*-limonene oxide will result in the formation of a nearly stereo-regular *trans* polycarbonate.

### 5.3.4 Conclusions

Herein, we report the elucidation of the LO-CO<sub>2</sub> copolymerization mechanism catalyzed by the Al-aminotriphenolate/PPNCl system. The study on the stereoregularity of the obtained polycarbonate has been the main goal set in this project because the high number of reactive centers and possible conformations presented by LO.

In order to tackle this problematic, we studied both the thermodynamic stability of the growing chain and the kinetic preference of the nucleophilic attack to the two different carbon centers of the epoxide scaffold.

First, a detailed investigation on the initiation step was carried out, analyzing the preference of the nucleophilic attack of chloride over bromide to the most substituted respect least substituted carbon centers of the epoxide. An NBO population analysis was also included in the results in order to confirm the higher electrophilic character of  $\alpha$  in comparison to  $\beta$  carbon.

Using the results obtained in the first part we selected the most feasible routes to study the mechanistic insights of the propagation process. We confirmed the preference of the carbonyl oxygen to act as nucleophile, in comparison to the other oxygen of the carbonate group bonded to the Al

center, due to steric effects. Moreover, we observed a higher stabilization for those growing chains with *trans* conformation, being the nucleophilic attack to the  $\alpha$  carbon of a *cis* epoxide the most favorable route from both a kinetic and thermodynamic point of view. The copolymerization pathway was found to be more feasible than the cyclization route for all cases using the  $[Al^{Mc}]/PPNCl$  binary system, which is in line with the experimental findings.

UNIVERSITAT ROVIRA I VIRGILI

Computational Design of Catalysts for Carbon Dioxide Recycling

Joan González Fabra

*“Our nature consists in motion;  
complete rest is death.” Blaise Pascal*

# Chapter 6

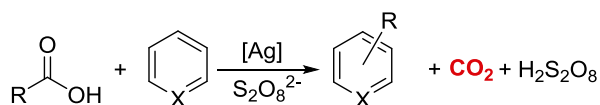
## Effect of CO<sub>2</sub> Pressure

### 6.1 Multiscale Metadynamics as Exploring Tool for Reactivity

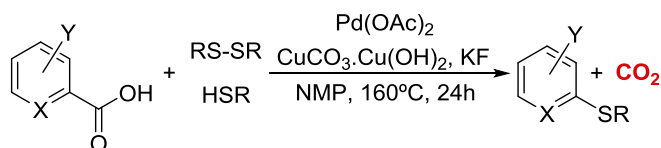
#### 6.1.1 Introduction

In the previous chapters of this Thesis, the main goal was to elucidate mechanistic routes to describe the formation of valuable products through the fixation of CO<sub>2</sub>. In this chapter we focus on the study of the reverse process to investigate the stability of the formed carbonates, and more interestingly, the effect of CO<sub>2</sub> pressure towards decarboxylation or isomerization of carbonates. The reaction of isomerization of carbonates was first studied through static standard DFT-based methods in section 3.3 of this Thesis. The racemization of cyclic carbonates is particularly relevant for those obtained from substituted glycidol derivatives that present an enantiomeric center. On the other hand, the decarboxylation reaction is an important counter-process of CO<sub>2</sub> fixation that should be taken into account. Moreover, decarboxylation of carboxylic acids and

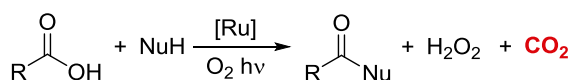
organic carbonates is an interesting tool in many synthetic routes to obtain valuable products. In **Figure 6.1** we collected some representative reactions of decarboxylation of carboxylic acids. In recent years, the catalyzed photochemical decarboxylation reaction has been widely investigated due to its wide scope of reactivity and selectivity. The high stability of CO<sub>2</sub> drives the reaction towards no thermodynamically favored products when starting from relatively stable reactants. However, in order to overcome the kinetic barrier of the reaction it is necessary to use a catalytic active species, usually a transition metal complex based on silver,<sup>[144]</sup> palladium,<sup>[145]</sup> ruthenium<sup>[146]</sup> or nickel.<sup>[147]</sup> By using different conditions, reagents and catalysts, decarboxylation can lead to a wide variety of chemical transformations from very similar reagents, thus constituting a very powerful synthetic tool.



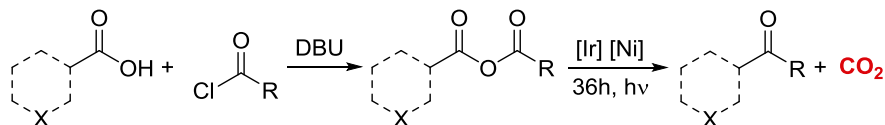
**Minisci et al., 1971** R = Alk, X = N    **Su et al., 2015** R = Ar, X = C, N



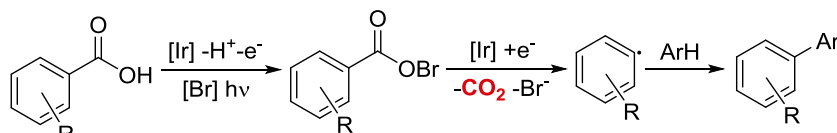
**Liu et al., 2009** X = C, N Y = H, NO<sub>2</sub>, COCH<sub>3</sub>, CHO, CN



**Lei et al., 2014**



**MacMillan et al., 2014** X = C, N, O



**Glorius et al., 2017**

**Figure 6.1** Several representative examples of carboxylic acid decarboxylation reactions.



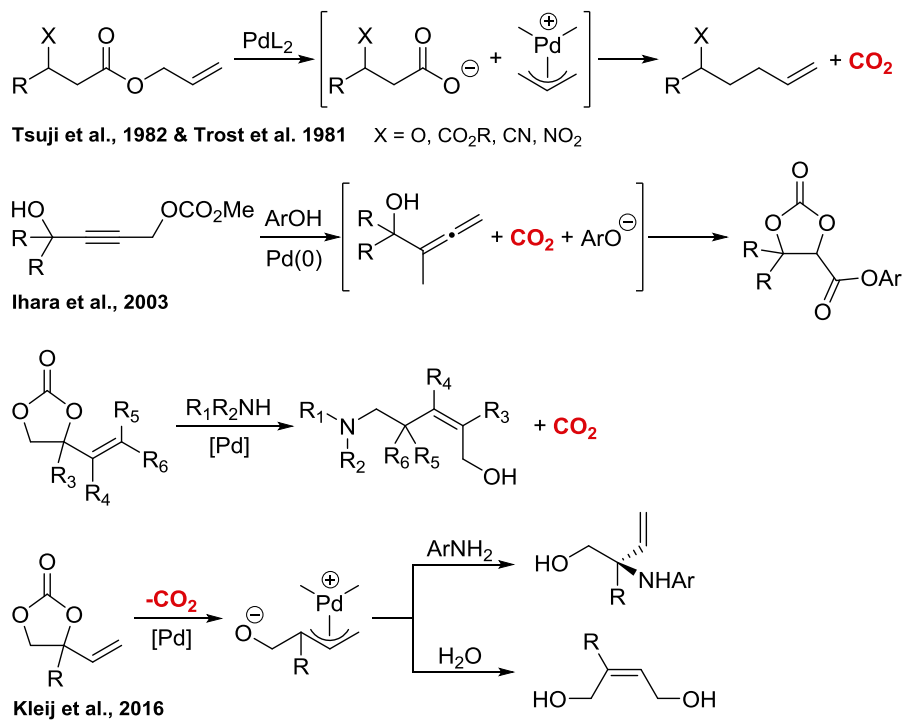


**Figure 6.2** Several representative examples of organic carbonates decarboxylation reactions.

In addition to decarboxylation of carboxylic acids, which is the most usual reactant, decarboxylation process can take place using organic carbonates as well. In this chapter we are mainly interested in these transformations, which some examples are illustrated above in **Figure 6.2**. The first example of carbonates decarboxylation catalyzed by palladium was proposed by Trost,<sup>[148]</sup> and later on, developed by Tsuji.<sup>[149]</sup> The reaction mechanism is based in the palladium-allylic intermediate showed within brackets in the first reaction of **Figure 6.2**. The allylic intermediate reactivity is versatile and flexible because its zwitterionic character. Many variations of the Tsuji-Trost reaction have been developed in recent years,<sup>[150]</sup> like the formation of cyclic carbonates from linear acetylenic carbonates through CO<sub>2</sub> relaxation.<sup>[151]</sup> An example of CO<sub>2</sub> relaxation is showed in the second reaction of **Figure 6.2**, where a CO<sub>2</sub> moiety is expelled from the substrate to later on be inserted again in a different position forming a different product. In this example an aryl substituent

has been included in the carboxylic position forming an aromatic ester from an aliphatic ester. CO<sub>2</sub> relaxation is an interesting strategy to reorganize a molecule that contains several functional groups, opening the possibility to include additional moieties to the product. The last example presented by Kleij and coworkers,<sup>[102d, 152]</sup> involves cyclic carbonates. In the first case, secondary aromatic or aliphatic amines can generate tri- and tetrasubstituted allylic amines from cyclic vinyl carbonates with high stereoselectivity.<sup>[102d]</sup> In the next case, after generating the palladium-allylic intermediate, two examples of different reactivity are showed. First, the allylic amination using primary amines to form  $\alpha,\alpha$ -disubstituted allylic N-arylamines. It is worth noting that different regioselectivity is obtained respect the previous example.<sup>[152a]</sup> The last reaction using water as nucleophile leads to the formation of (*Z*)-1,4-but-2-ene diols with high stereoselectivity.<sup>[152b]</sup>

Summarizing, decarboxylation of carboxylic acids and organic carbonates presents high interest to study it in detail because two reasons. First, we can use decarboxylation as synthetic tool for many products, hence it is important to know in detail what factors, like CO<sub>2</sub> pressure, can interfere in the reaction mechanism. Second, aiming to improve the efficiency of CO<sub>2</sub> fixation reactions we want to prevent decarboxylation to guarantee high activity and selectivity.

The partial pressure of CO<sub>2</sub> applied at the system is one of the main factors of carbonate stability towards decarboxylation or isomerization via CO<sub>2</sub> relaxation. In order to study this effect in the reaction, we aim to use QM/MM metadynamics simulation<sup>[57, 61, 153]</sup> to elucidate the reaction mechanism of decarboxylation and racemization of cyclic carbonates obtained from glycidol and CO<sub>2</sub>. This multiscale approach has been used in many reaction mechanisms like propagation and termination steps of polymerization reactions<sup>[154]</sup> or enantioselective palladium-catalyzed hydrosilylation,<sup>[155]</sup> among other reaction catalyzed by homogeneous catalysts.<sup>[156]</sup> Metadynamics simulations have been also used to study chemical reactions using heterogeneous catalysts,<sup>[58]</sup> biological

processes<sup>[59, 157]</sup> or even decarboxylation reactions catalyzed by enzymes.<sup>[158]</sup> By using adaptive QM/MM metadynamics simulations, we can modify the size of the active site computed at QM level on the fly by defining a region of a given size around the reactive moieties. Consequently, the amount of molecules within the QM region will change while the molecules diffuse inside and outside the defined QM region. Considering the region around the reactive event at the QM level is crucial in many catalyzed reaction where the solvent plays a key role in the mechanism.<sup>[66, 159]</sup>

Herein, we report a detailed QM/MM adaptive metadynamics study on the effect of the partial pressure of CO<sub>2</sub> to the decarboxylation and racemization reactions of cyclic carbonates.

### 6.1.2 Goals

Our main goal in this chapter is to elucidate the reaction mechanism of racemization of glycidol carbonate and the decarboxylation of cyclic carbonates by using molecular metadynamics simulations. Then, we plan to unravel the effect of CO<sub>2</sub> pressure in the rate of these two different reactions. Racemization reaction do not generate CO<sub>2</sub> or any other sub-product. On the other hand, cyclic carbonate decarboxylation reaction produces the original epoxide and CO<sub>2</sub>. Hence, we hypothesize that we will observe the rate affected in a different way when pressure changes.

In order to tackle this investigation, a molecular metadynamics simulation method seems an adequate approach, since it allows simulating a realistic system including the relative concentrations of all species and the total pressure applied to the system. Standard static DFT-based methods used in the previous studies of this Thesis are not appropriate to describe in detail the effect of CO<sub>2</sub> pressure. By changing the pressure of CO<sub>2</sub>, we change both the solubility and the total pressure of the system. Therefore, the ratio of CO<sub>2</sub> molecules per molecule of solvent and reactant increases by increasing the CO<sub>2</sub> pressure. Instead, the simulation box size decreases by increasing the total pressure.

Summarizing, we plan to evaluate the effect of the CO<sub>2</sub> partial pressure in the rate of decarboxylation and racemization reactions of cyclic carbonates produced from CO<sub>2</sub> fixation.

### 6.1.3 Computational Details

All calculations have been carried out by using the FlexMD module included in ADF package (<https://www.scm.com>).<sup>[67, 159b, 160]</sup> FlexMD is a python library for flexible multiscale (IMOM-type<sup>[65]</sup>) molecular dynamics simulations.<sup>[161]</sup> The QM region was described using the semiempirical PM6-DH<sup>+</sup><sup>[160]</sup> Hamiltonian, which includes empirical dispersion corrections, as implemented in MOPAC program.<sup>[162]</sup> The force field for the MM region was CHARMM-TIP3P<sup>[163]</sup>, and we used NAMD<sup>[164]</sup> for computing the classical energy and gradients. The model system for the reaction media is a periodic simulation box that contains 86 molecules of solvent (butanone), 8 molecules of trimethylamine (TMA), 8 molecules of water, 8 molecules of glycidol carbonate and  $n$  ( $n=1, 14, 28, 74$ ) additional molecules of CO<sub>2</sub> depending on the CO<sub>2</sub> pressure ( $P=1, 10, 20, 50$  bar). The periodic simulation box oscillates between 25Å and 28Å also depending on the CO<sub>2</sub> pressure. Independent metadynamics simulations runs of 100ps long (0.5 fs/step, up to 5 runs) were considered for each trajectory, which were initiated using different initial velocity seeds. All these simulations included one or two Collective Variables (CVs) to explore the reaction energy surface, depending on the studied reaction: 1 CV for the decarboxylation and 2 CVs for the racemization. The chosen CVs will be presented in more detail in the next section. These CVs have been explored placing Gaussian functions of 1.0 kcal·mol<sup>-1</sup> height and 0.1 Å width, thus guaranteeing the affordability of the calculation and ensuring the required precision to map the free-energy surface. One Gaussian function has been added each 500 steps of simulation, hence safeguarding the stability of the simulation. A region of 4Å around each one of the two QM-centers has been set to describe, at QM level, all the nearby molecules. No transition region has been set between the QM and the MM regions. Quadratic walls have been used to

constrain some coordinates in order to facilitate the description of the reaction avoiding unreactive conformers. A Langevin thermostat has been used at 300 K with a friction of  $0.5 \text{ ps}^{-1}$  to control the temperature.

#### 6.1.4 Groundwork

Before start running molecular dynamics simulations and obtaining trustworthy results, some care has to be taken for preparing data and building the system. Therefore, in this first section we plan to expose what elements do we need to run the metadynamics with FlexMD and how do we prepare it.

First, it is worth noticing that FlexMD serves as a wrapper for several molecular program packages, each providing the required QM or MM energies and forces. In this project we used MOPAC to calculate the QM region and NAMD for the MM region. FlexMD uses the Atomistic Simulation Environment (ASE) as propagator for the molecular dynamics. FlexMD defines the geometry of the molecular system using either PDB or XYZ files. After calculating the energies of both QM and MM regions, by MOPAC and NAMD respectively, the resulting forces are used by ASE to perform the dynamics step. Internally, the propagator sets up the required ASE objects, passes the forces to them, and retrieves the new positions and velocities. An additional protagonist, a manager class instance, coordinates the MD simulation by running the MD steps with the ASE propagator and writing trajectory information.

We considered a periodic system as depicted schematically in **Figure 6.3**, with two regions named active (A) and environment (E). First one, which is usually the smallest, is calculated by QM methods, and second one by MM methods. It is possible to include an intermediate transition region (T) between QM and MM. The molecules located in T region are calculated by both QM and MM methods. Then, the QM-MM ratio is pondered depending on the distance to QM region. The closer to QM region, the higher will be the QM contribution. In this project we did not

consider a transition region, since it was not necessary because the transition between QM and MM was smooth enough.

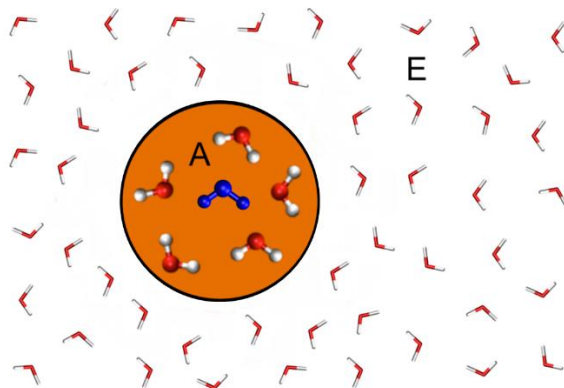


**Figure 6.3** Model representation of a QM calculated water molecule (blue) surrounded by QM calculated water molecules (A-region). The other solvent molecules (E-region) are calculated by MM methods. This figure is adapted from J. Chem. Theory Comput. 2016, 12, 3441–3448.

The total energy of this model system can be calculated using **Eq. 6.1** showed below.

$$E^{QM/MM} = E_A^{QM} + E_{A+E}^{MM} - E_A^{MM} \quad \text{Eq. 6.1}$$

As it can be seen in the equation, the entire system is calculated by MM methods, so we need a force field to describe the entire system and not only the MM region exclusively. In our system, formed by organic molecules, the CHARMM-TIP3P force field includes all parameters required to calculate the entire system at the MM level. Consequently, the initial set-up for the system was carried out using exclusively the CHARMM-TIP3P force field with NAMD program.

The first step was building the periodic simulation box using the Packmol program<sup>[165]</sup> with a tolerance (minimum distance) of 2Å between each molecule. Using this initial simulation box an energy minimization calculation was run for 100,000 steps including periodic boundary

conditions. After taking the resulting structure, we run a NPT simulation of 250ps to optimize the box size according to the number of atoms included in the simulation box and the total pressure applied to the system. In this NPT simulation, the temperature was increased by 5K each 1000 steps from 0K to 300K. The resulting box size is maintained fixed during the next simulation step, which is a NVT of 500ps to equilibrate the system. In the case of the racemization reaction, which will be explained in section 6.1.5.a, a reactive conformer previously optimized by DFT-based methods, was constrained during all these preparatory simulations.

The optimized and equilibrated structure by MM methods was then used as initial structure for a QM/MM molecular dynamics to equilibrate the system using the multiscale methodology indicated in the previous section. We noticed that this additional equilibration is not necessary because we observed minor variations in the structure with respect to the full MM simulation. Therefore, the description by the force field is accurate enough to describe our system in an unreactive scenario.

## 6.1.5 Results and Discussion

### 6.1.5.a Racemization of Cyclic Carbonates

The thermodynamic stability of a molecule is usually measured as the difference in Gibbs free-energy between its resting state and the product of a degradation or a reverse reaction. We can also study the stability of a molecule towards its isomerization. In the case of enantiomerically pure species, racemization is an important process to take into account, since one reaction mechanism can be 100% enantioselective but a favorable side-reaction could lead to racemization of the product, thus producing a racemic mixture. A particular case of racemization regarding cyclic carbonates obtained from epoxy alcohols and CO<sub>2</sub> is illustrated below in **Figure 6.4**, and it was presented in Chapter 3 of this Thesis.

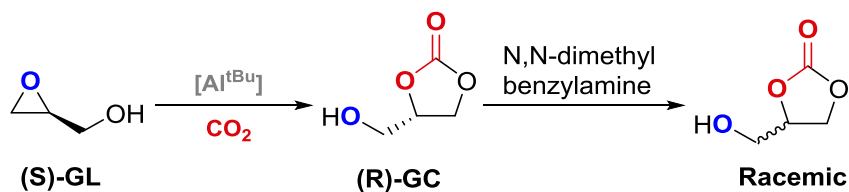


**Figure 6.4** Schematic representation of glycidol carbonate formation from glycidol and its consecutive racemization catalyzed by N,N-dimethylbenzylamine.

The racemization process of glycidol carbonate (GC) is based in an acid-base reaction between GC and a base. The base used by the experimentalists to characterize the GC was N,N-dimethylbenzylamine. Note that the phenolate groups in the ligand of the aluminum catalyst present in the solution can also catalyze the racemization reaction. Actually, this reaction was studied by means of DFT-based methods and presented in section 3.3 of this Thesis. We elucidated the reaction mechanism considering one phenolate of  $[Al^{Me}]$  as the basic center to undergo deprotonation and initiate the racemization reaction (see **Figure 6.5**).

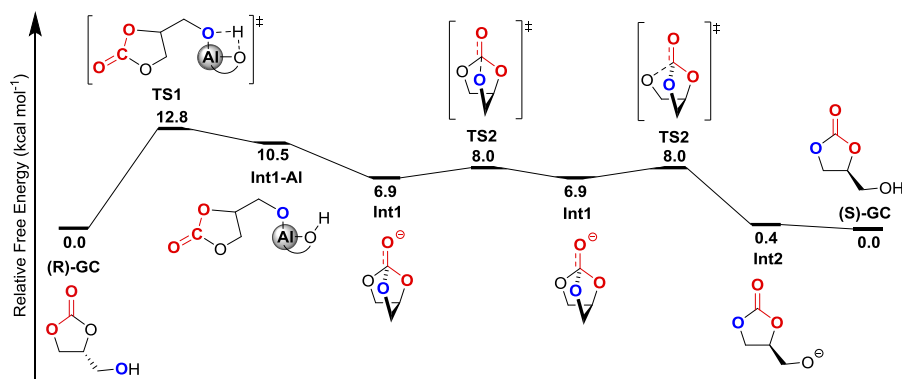


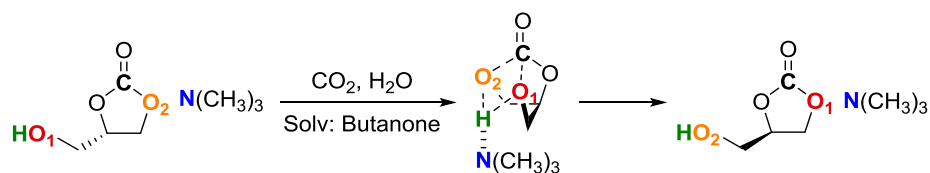
**Figure 6.5** Gibbs free-energy profile for racemization of GC catalyzed by the phenolate group present in the ligand of  $[Al^{Me}]$  catalyst.

The proposed mechanism presents an activation barrier of 12.8 kcal·mol<sup>-1</sup>, leading to an equilibrium between both enantiomers. It is worth mentioning that the most energetically demanding step is the deprotonation of GC to generate an alkoxide (**Int1-Al**). After



deprotonation step, the reaction moves forward almost spontaneously to the GC enantiomer via a symmetric meta-stable intermediate (**Int1**). We expect to spot that intermediate in the course of the metadynamics simulation.

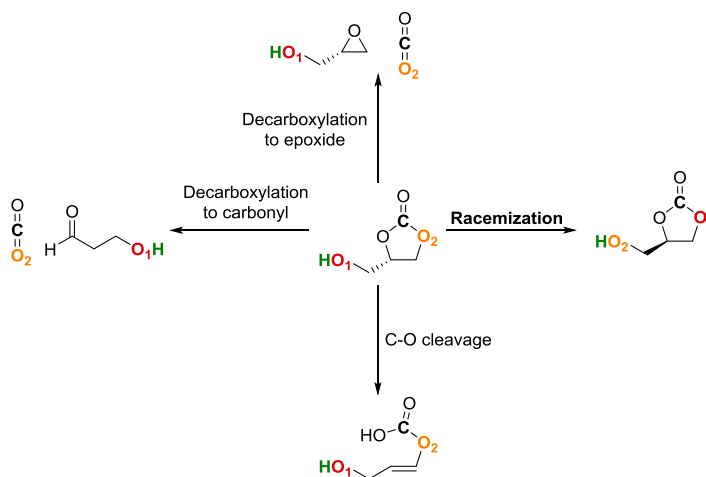
The previous static study eased the selection of the Collective Variables (CVs), which is not a straight-forward procedure in metadynamics simulations.<sup>[166]</sup> It is worth noticing that we choose an amine base for this study in order to reduce the size of the system and, consequently, the computational cost of the calculations. Instead of using the entire aluminum coordination complex, we considered trimethylamine (TMA) as a model of the N,N-dimethylbenzylamine. Additionally, the periodic simulation box contained CO<sub>2</sub>, water, GC and butanone, which is the solvent of the reaction. All these molecules were present in the simulation box and no glycidol at all because we considered a 100% conversion scenario of the GC formation from glycidol and CO<sub>2</sub>. The reaction occurs involving two molecules: GC and TMA. GC is both the reactant and product, while TMA acts as a catalyst, which consequently is recovered after the reaction finishes (see **Figure 6.6**). Therefore, CO<sub>2</sub>, water and butanone were not actively involved in the reaction, a priori. It is worth mentioning that 8 GCs and 8 TMAs were included in the simulation box but we considered only one of each to study the reaction, hence the other 7 GCs and TMAs molecules remained in the environment region acting as spectators.



**Figure 6.6** Schematic representation of glycidol carbonate racemization reaction catalyzed by trimethylamine. A tentative structure of the transition state is included.

The CVs have to describe the reaction pathway from reactants to products. Therefore, chemical intuition is probably the most important

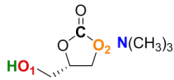
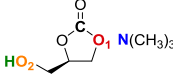
requirement to choose the correct set of CVs. Taking into account the DFT based results showed previously, the goal of the CVs should be describing the deprotonation process, thus forming the **Int1-A1** intermediate, which is the most energetically demanding process. After reaching **Int1-A1** intermediate, the reaction will evolve to the desired product. Then, one CV has to describe the formation of N-H bond and consequently, O<sub>1</sub>-H bond breaking. Another bond that has to be formed is C-O<sub>1</sub>, breaking simultaneously the C-O<sub>2</sub> bond. One would think that 4 CVs are required, one CV for each bond. On the contrary, many processes like bond breaking and forming are not independent, so we can select the CV thinking on how “filling” a coordinate will affect to others. In an ideal situation one would consider only one CV, which reduces the simulation time in comparison to use two or three CVs. However, more than one CV is compulsory to explore the reaction sometimes. In **Figure 6.7** depicted below we show all the side-products that could be obtained by using either inadequate CVs or excluding one of the two CVs used in the metadynamics simulations. See **Table 6.1** for the definition of the CVs.



**Figure 6.7** Schematic representation of all side-reactions observed when choosing the CVs to obtain the reaction. Racemization reaction is highlighted in bold. Decarboxylation to epoxide will be studied in the next section.

The three distances C-O<sub>1</sub>, O<sub>1</sub>-H and N-H have been considered in the CVs. C-O<sub>1</sub> and N-H have to decrease, forming the new bonds necessary to form **Int1-Al**, while H-O<sub>1</sub>-H has to increase, thus deprotonating the alcohol. Once the intermediate is formed, C-O<sub>1</sub> and O<sub>1</sub>-H have to keep the same trend: C-O<sub>1</sub> has to decrease and O<sub>1</sub>-H has to increase, but H-N has to invert its trend, now increasing to deprotonate TMA and consequently, protonate the new alcohol forming O<sub>2</sub>-H bond. This behavior is the reason of using two CVs instead of one. If we used just CV<sub>1</sub>, we would not describe N-H distance, which is a crucial coordinate to obtain the alkoxide. On the other hand, if we just consider CV<sub>2</sub>, we would not describe C-O<sub>1</sub> bond that is required to obtain the final product. Finally, O<sub>1</sub>-H has to be included in both CVs.

**Table 6.1** Definition of the CVs used for metadynamics simulations. Both CVs are obtained from the difference of atom distances (D<sub>1</sub>, D<sub>2</sub> and D<sub>3</sub>) that are indicated in the first rows for both enantiomers, being (R)-GC the reactant and (S)-GC the product, and the **Int1-Al** intermediate. The two CVs used to explore the reaction are highlighted in bold.

	<b>(R)-GC</b> (Reactant)	<b>Int1-Al</b> (Alkoxide)	<b>(S)-GC</b> (Product)	
D <sub>1</sub> : d(C-O <sub>1</sub> )	2.5	2.0	1.5	D <sub>1</sub> : d(C-O <sub>1</sub> )
D <sub>2</sub> : d(O <sub>1</sub> -H)	1.0	2.5	3.0	D <sub>2</sub> : d(O <sub>1</sub> -H)
D <sub>3</sub> : d(N-H)	2.0	1.0	2.0	D <sub>3</sub> : d(N-H)
<b>CV<sub>1</sub>: D<sub>1</sub>-D<sub>2</sub></b>	<b>1.5</b>	<b>-0.5</b>	<b>-1.5</b>	<b>CV<sub>1</sub>: D<sub>1</sub>-D<sub>2</sub></b>
<b>CV<sub>2</sub>: D<sub>3</sub>-D<sub>2</sub></b>	<b>1.0</b>	<b>-1.5</b>	<b>-1.0</b>	<b>CV<sub>2</sub>: D<sub>3</sub>-D<sub>2</sub></b>

After choosing the proper set of CVs, another crucial aspect that had to be taken into account was the C-O<sub>1</sub> orientation, which has to facilitate the bond formation by rotating a dihedral angle  $\delta$  (O<sub>1</sub>-C-C-O) to face O<sub>1</sub> with C, as depicted in **Figure 6.8**. The most stable conformer of GC is **A**, which has a dihedral angle  $\delta$  of 180°. On the other hand, the reactive conformer is **B**, which has a  $\delta$  of 40°. Therefore, we optimized by DFT based-methods conformer **B** including constraints to prevent it to be back to **A**. The optimized structure **B** is constrained during the set-up

defined in section 6.1.4. Finally, we placed a quadratic wall to prevent C-O<sub>1</sub> distance to become larger than 2.5Å, so preventing the formation of conformer **A**. A second quadratic wall is necessary in the metadynamics simulation because there is a low probability of encountering TMA and GC within the simulation box. Additionally, the solvent of the reaction (butanone) can interact with GC via hydrogen bonding. The reactive proton of the alcohol group of GC interacts with the carbonylic oxygen of MEK blocking the interaction with TMA, which is the required interaction previous to GC deprotonation. Consequently, we placed a quadratic wall on the O<sub>1</sub>-N distance to avoid becoming larger than 2.5Å. In conclusion, we facilitated the formation of the optimal conformer to undergo the racemization reaction. Both quadratic walls were crucial to obtain the reaction in reasonable simulation times.

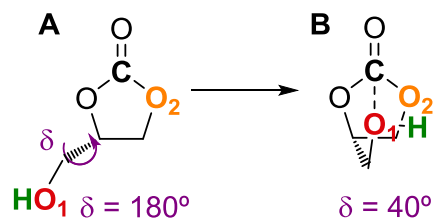


**Figure 6.8** Schematic representation of two structural conformers of GC by rotating dihedral angle  $\delta$  (O<sub>1</sub>-C-C-O).

In all metadynamics simulations, the reaction took place in 70-90ps depending on two factors: the orientation of GC and TMA and the number of Gaussian functions placed into the free-energy well. Hence, the more steps we run, the more Gaussian functions we place, and so the more probable is a reactive conformer of GC to escape from the free-energy well. A detailed tracking of the significant bond lengths in the reaction is shown in **Figure 6.9**, which plots the time evolution of the C-O<sub>1</sub>, N-H, C-O<sub>2</sub> and O<sub>2</sub>-H distances. As it can be seen in **Figure 6.9**, N-H (blue line) is the first distance that suffers a big change at 87.2ps. In this moment the deprotonation takes place, N-H distance increases till 1Å at 89.25ps, when the proton is transferred to O<sub>2</sub>. The O<sub>2</sub>-H distance

(green line), which initially is the largest one (2.5Å), gradually decreases until 1.5Å at 88.7ps when the product is formed. Additionally, C-O<sub>1</sub> (red line) distance starts at 2.2Å and smoothly decreases until 1.4 Å, at the same time that O<sub>1</sub> is deprotonated first by TMA, and later the proton is transferred to O<sub>2</sub>. Finally, the C-O<sub>2</sub> (orange line) distance is kept constant until 89.25ps when the reaction takes place, and rapidly O<sub>2</sub> goes away from C, indicating the formation of the (S)-GC enantiomer.

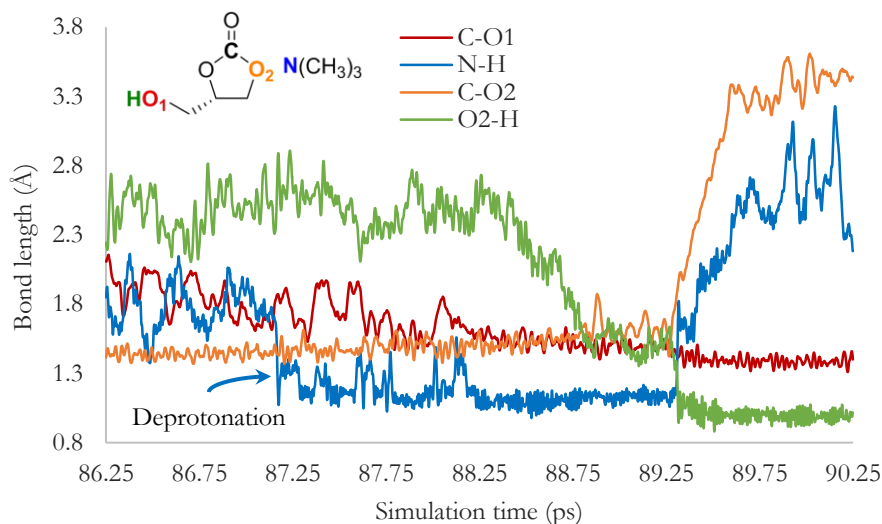


**Figure 6.9** Bond distance evolution of C-O<sub>1</sub> (red trace), N-H (blue trace), C-O<sub>2</sub> (orange trace) and O<sub>2</sub>-H (green trace) during 4ps of the metadynamics simulation.

The resulting free-energy surface is illustrated in **Figure 6.10**. The initial free-energy of GC before the simulation starts amounts  $-17\text{kcal}\cdot\text{mol}^{-1}$  with respect the saddle point or Transition State (TS) situated at  $0\text{ kcal}\cdot\text{mol}^{-1}$ , hence the activation free-energy for the racemization of GC is  $17\text{ kcal}\cdot\text{mol}^{-1}$ . Comparing this Gibbs free-energy barrier value with the previously obtained ( $12.8\text{ kcal}\cdot\text{mol}^{-1}$ ) by DFT based-methods, we confirm<sup>[167]</sup> that semi-empirical methods like PM6-DH<sup>+</sup> combined with explicit solvation described by CHARMM/TIP3P can describe this type of organocatalyzed reactions. Additionally, aiming to reaffirm the correlation between DFT and PM6-DH<sup>+</sup>/CHARMM we studied the racemization reaction using TMA as co-catalyst instead of the Al catalyzt.

Using M06-2X functional, which is particularly recommended for organic systems, we observed a stepwise mechanism similar to the metadynamic simulation, where deprotonation by TMA occurs first, followed by C-O<sub>2</sub> cleavage and protonation of O<sub>2</sub>. The computed absolute barrier for M06-2X is 23.1 kcal·mol<sup>-1</sup>. Moreover, in order to analyze the effect of QM/MM methods we also studied the system using static PM6 where the same mechanism is observed and a similar barrier of 19.3 kcal·mol<sup>-1</sup>. Therefore, PM6-DH<sup>+</sup>/CHARMM is an excellent method to study this kind of organic systems involving many bond breaking-forming processes with good accuracy comparing it to DFT based-methods.

Analyzing the 3D plot of the free-energy surface we can see two wells of equal energy (17 kcal·mol<sup>-1</sup>) and the same value of CV<sub>1</sub>, hence related to two equally stable isomers of GC interacting with TMA. Both energy minima are located at 1.5 of CV<sub>1</sub> and at 0.75 and 1.25 of CV<sub>2</sub> as it can be seen in the topographic cut of **Figure 6.10**. The reactive event can be visualized by decreasing CV<sub>2</sub> until -0.5. This value is lower than the initially postulated (-1.0) in **Table 6.1**.

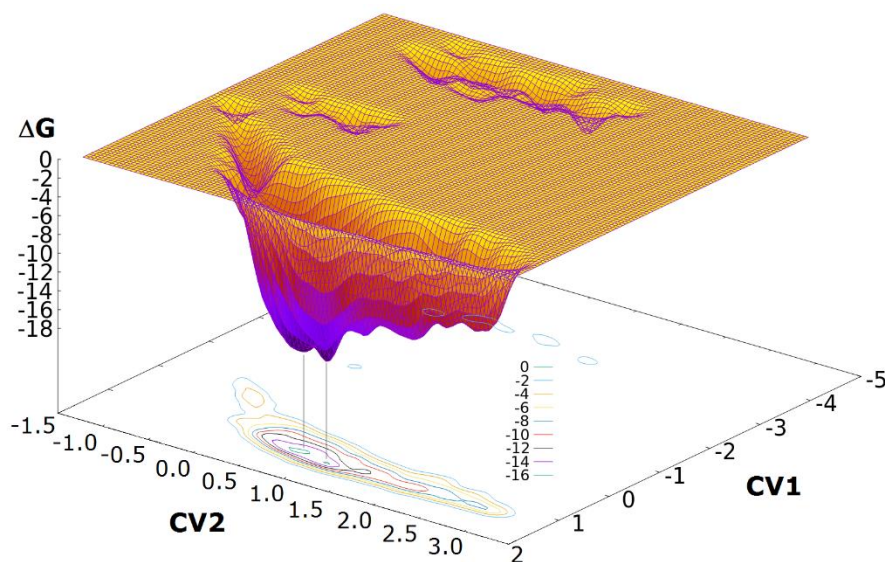


**Figure 6.10** Gibbs free-energy surface for CV<sub>1</sub> and CV<sub>2</sub> describing the racemization reaction of (R)-GC to (S)-GC.

It is worth noticing the importance of  $CV_1$  because at first sight one could think that only considering  $CV_2$  we could describe the reaction, but when approaching to the saddle point,  $CV_1$  changes from 1.5 to 0. Therefore, both CVs are required to study this reaction by metadynamics simulation. Other important information that could be obtained from the free-energy surface is the number of stable conformers. We observe several local minima at relatively low energies. If we would remove the quadratic walls that we placed to confine the reaction, we would observe a more extended free-energy surface with more conformers, but as we stated before, we would not observe any reaction until much longer simulation times.

We studied the reaction mechanism of racemization by metadynamics simulation using a correct set of CVs and we analyzed the resulting free-energy surface. After doing this, we proceeded to study the effect of  $CO_2$  on the activation barrier of the reaction. We considered three values for the  $CO_2$  pressure: 1, 10 and 50 bar. When we increase the pressure of  $CO_2$  we increase both the total pressure on the system and the concentration of  $CO_2$  in the solution.<sup>[168]</sup> Therefore, in **Table 6.2** we collected the number of  $CO_2$  molecules included in the simulation and also the calculated activation barrier.

**Table 6.2** Range of  $CO_2$  pressure considered for racemization reaction indicating the number of  $CO_2$  molecules within the periodic simulation box (second column) and the corresponding activation energy and standard deviation.

Pressure (bar)	n $CO_2$	$\Delta G^\ddagger$	Standard Dev
1	1	18	$\pm 2$
10	14	17	$\pm 1$
50	74	16	$\pm 2$

We did not observe major variations in the Gibbs free-energy barrier but we can see a decreasing trend regarding activation barrier when pressure increases. We considered several values of pressure for decarboxylation reaction too, which will be presented and discussed together with these results in the next section of this chapter.

Racemization reaction of GC catalyzed by TMA has been successfully studied by QM/MM metadynamics simulations. The resulting free-energy surface proved the necessity to use two CVs to describe this reaction mechanism that involves many bond forming and breaking processes. Moreover, we determined the most active conformer of GC to overcome the reaction by facing O<sub>1</sub> to the carbonylic carbon of GC. Finally, we could determine the absolute and relative free-energy barriers of the process. During the simulations we could observe first the deprotonation of GC by TMA to form a meta-stable alkoxide intermediate that evolves to the GC racemic product. Several pressure values have been considered observing a decrease of the activation energy when pressure increases.

#### 6.1.5.b Decarboxylation

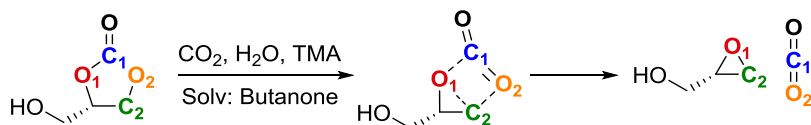
The chemical fixation of CO<sub>2</sub> using epoxides could go back through decarboxylation reaction expelling CO<sub>2</sub> from the just formed carbonate. This back-reaction can lead to lower activity and selectivity in CO<sub>2</sub> fixation processes. In this section we present and discuss the results obtained in the study of the uncatalyzed decarboxylation reaction of GC by QM/MM metadynamics simulations, using the same procedure presented in the previous section regarding racemization of GC.

Uncatalyzed decarboxylation reaction mechanism is simpler than racemization of GC. First, we did not need to consider any catalyst since only GC is involved in the reaction. Therefore, the uncatalyzed reaction is a high energy demanding process but mechanistically simpler, probably constituted by one step only. Finally, just one CV may be necessary to study the reaction, simplifying the selection of CVs and reducing the simulation time.

Decarboxylation reaction is illustrated below in **Figure 6.11**. The reaction occurs by breaking the C<sub>1</sub>-O<sub>1</sub> and C<sub>2</sub>-O<sub>2</sub> bonds and forming the O<sub>1</sub>-C<sub>2</sub> bond, hence forming an epoxy-alcohol and CO<sub>2</sub>. This reaction could be catalyzed by transition metals complexes as we presented in the introduction section. Nevertheless, in this study we considered the



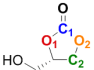
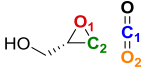
uncatalyzed reaction because we were mainly interested in evaluating the effect of CO<sub>2</sub> pressure in the rate of the reaction.



**Figure 6.11** Schematic representation of uncatalyzed glycidol carbonate decarboxylation. A tentative structure of the transition state is included.

In this case the selection of the CVs is an easier task. However, there is one aspect to take into account. By definition, the carboxylic carbon (C<sub>1</sub>) in all cyclic carbonates is connected to three oxygen atoms. Two of these oxygen atoms are bonded each one of it to another carbon. Therefore, one could think that we could decarboxylate forming CO<sub>2</sub> as O-C<sub>1</sub>-O<sub>1</sub> or O-C<sub>1</sub>-O<sub>2</sub>, and the resulting epoxide would contain O<sub>2</sub>-C<sub>2</sub> or O<sub>1</sub>-C<sub>2</sub> respectively. We considered both possibilities when running the metadynamics simulations. However, when we tried to break C<sub>1</sub>-O<sub>2</sub> bond through the corresponding CV, we did not obtain the desired product but other side-products already showed in **Figure 6.5** above. Therefore, the reaction occurred exclusively forming the O-C bond with the less substituted carbon (O<sub>1</sub>-C<sub>2</sub>). Consequently, the CV used to study the reaction is presented below in **Table 6.3**.

**Table 6.3** Definition of the CV used for metadynamics simulations. The CV is obtained from the difference of atom distances (D<sub>1</sub> and D<sub>2</sub>) that are indicated in the first rows for (R)-GC, which is the reactant and (R)-GL and CO<sub>2</sub>, which are the products. The CV used to explore the reaction is highlighted in bold.

	<b>(R)-GC</b> (Reactant)	<b>(R)-GL+CO<sub>2</sub></b> (Product)	
D <sub>1</sub> : d(C <sub>1</sub> -O <sub>1</sub> )	1.5	3.0	D <sub>1</sub> : d(C-O <sub>1</sub> )
D <sub>2</sub> : d(C <sub>2</sub> -O <sub>1</sub> )	2.5	1.5	D <sub>2</sub> : d(H-O <sub>1</sub> )
<b>CV<sub>1</sub>: D<sub>2</sub>- D<sub>1</sub></b>	<b>1.0</b>	<b>-1.5</b>	<b>CV<sub>1</sub>: D<sub>2</sub>- D<sub>1</sub></b>

We used the same methodology as in the previous section so two distances were included in one CV. We know that C<sub>1</sub>-O<sub>1</sub> distance has to

increase while  $C_2-O_1$  has to decrease, thus breaking  $C_1-O_1$  bond and forming  $C_2-O_1$  bond. Consequently,  $CV_1$  formed by  $D_2-D_1$  has to decrease.

We tracked the distances modified during 1ps of simulation time, precisely between 86.5 and 87.5ps, as plotted in **Figure 6.12**. Also, we interested in the value of  $O-C_1-O_2$  angle, which is the angle of the  $CO_2$  molecule. The  $CO_2$  angle facilitates the visualization of the product formation because the typical angle of a carbonate is approximately  $130^\circ$  and a free  $CO_2$  molecule has an angle of  $180^\circ$  according to its linearity. In  $CO_2$  fixation, this angle is a simple parameter to notice if  $CO_2$  is free ( $180^\circ$ ), activated ( $\sim 150^\circ$ ) or included in the target molecule ( $120-130^\circ$ ).

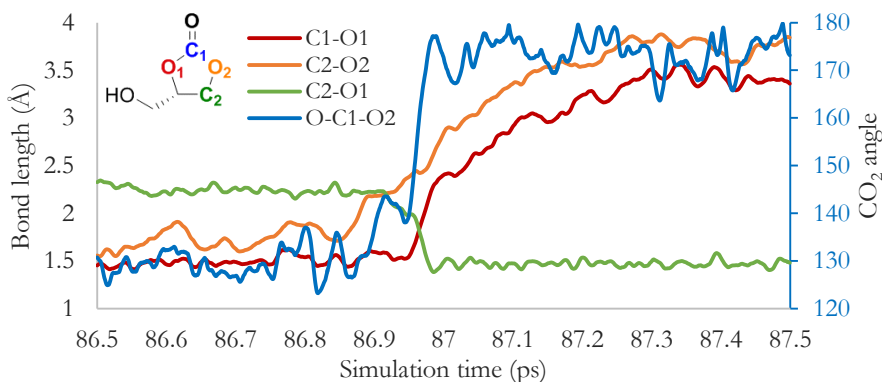


**Figure 6.12** Graphic representation of  $C_1-O_1$  (red),  $C_2-O_2$  (orange) and  $C_2-O_1$  (green) bond length variation during 1ps of the metadynamics simulation related to the reactive event. The angle formed by  $O-C_1-O_2$  (blue) is also included (right axis).

As it can be seen in **Figure 6.12**, this reaction mechanism shows a single step at simulation time 86.95ps. The angle formed by  $O-C_1-O_2$  starts oscillating at 86.75ps, at the same time that  $C_2-O_2$  distance starts to increase. If  $C_2-O_2$  is the first coordinate to change, we could think that a good catalytic strategy to facilitate decarboxylation would be to activate this  $C_2-O_2$  bond breaking. For example, coordinating a Lewis acid decreasing the nucleophilicity of oxygen atom  $O_2$ . In the case that we aim to prevent decarboxylation, we should do the opposite: increase the stability of  $C_2-O_2$  bond. After  $O-C_1-O_2$  angle reaches  $140^\circ$  and  $C_2-O_2$

reaches 2.2Å, C<sub>1</sub>-O<sub>1</sub> and C<sub>2</sub>-O<sub>1</sub> change rapidly indicating the formation of the product. First, C<sub>2</sub>-O<sub>1</sub> distance decreases, forming the C<sub>2</sub>-O<sub>1</sub> bond, and C<sub>1</sub>-O<sub>1</sub> distance increases rapidly, indicating C<sub>1</sub>-O<sub>1</sub> bond breaking. When C<sub>1</sub>-O<sub>1</sub> and C<sub>2</sub>-O<sub>2</sub> increase, also increase O-C<sub>1</sub>-O<sub>2</sub>, confirming the formation of CO<sub>2</sub>.

In decarboxylation reaction we considered only one CV. Additionally, the reaction is not catalyzed, leading to a simple parabola function with a minimum at 71 kcal·mol<sup>-1</sup> of CV<sub>1</sub> equal to 1, indicating the activation barrier for this reaction. While in the racemization reaction the energy of reactant and product is the same, in the decarboxylation energy of reactants and products is distinct. The calculated Gibbs free-energy of the reaction is 14 kcal·mol<sup>-1</sup>, indicating the higher stability of GC in comparison to the sum of the epoxide and CO<sub>2</sub>. Therefore, uncatalyzed decarboxylation of cyclic carbonates is an unfeasible process even at high temperatures. In order to determine the kinetic competition between CO<sub>2</sub> fixation and decarboxylation, we would have to consider decarboxylation reaction catalyzed by the same catalyst as CO<sub>2</sub> fixation. Decarboxylation reaction of carbonates or carboxylic acids, should also be considered with the respective catalytic species to determine the viability of the reaction. These mechanistic studies could also be carried out using standard static methods with implicit solvent as we did in the previous section.

We did not focus in the study of the kinetic competition between decarboxylation and CO<sub>2</sub> fixation but on the effect of the CO<sub>2</sub> pressure on the activation barrier. The higher we increase CO<sub>2</sub> pressure, the higher solubility of CO<sub>2</sub> in the reaction media and also, the higher total pressure applied to the entire system. Therefore, we considered three different states: 10, 20 and 50 bar, increasing CO<sub>2</sub> solubility accordingly to each pressure.<sup>[168]</sup> In all cases, we used the same CV as indicated above in the initial results, where 10 bar of CO<sub>2</sub> pressure were considered. The obtained results are collected in **Table 6.4**.

The value for the Gibbs free-energy barrier that we obtain by metadynamics simulation slightly increases when pressure of CO<sub>2</sub>

increases. This behavior is the opposite that we observed in the previous section regarding GC racemization where  $\Delta G^\ddagger$  decreased when pressure increased.

**Table 6.4** Range of CO<sub>2</sub> pressure considered for decarboxylation reaction indicating the number of CO<sub>2</sub> molecules within the periodic simulation box (second column) and the corresponding activation energy and standard deviation.

Pressure (bar)	n CO <sub>2</sub>	$\Delta G^\ddagger$	Standard Dev
10	14	71	$\pm 2$
20	28	72	$\pm 2$
50	74	76	$\pm 2$

This different trend in the two reactions is due to the variation in the total number of particles in the system. In the case that we change from one body to two bodies (decarboxylation reaction), when we increase the pressure we difficult the reaction. On the other hand, in racemization reaction, we need two bodies being brought together (TMA and GC) to form the reaction, hence the reaction is enhanced when the pressure increases.

### 6.1.6 Conclusions

QM/MM metadynamics simulation is a powerful tool to study complex reaction mechanisms in detail. First, we can describe the interaction of the reactant with the catalyst or the solvent. Next, we can track the variation of geometrical parameters during the reaction, facilitating the visualization of interactions between molecules, isomerization or bond breaking and forming processes. Finally, by inverting the Gaussian functions added during the metadynamics simulation, we can map the free-energy surface of the reaction, determining how the energy changes among the set of coordinates. By choosing different CVs we can study how the reaction takes place through alternative reaction paths and then, we can compare them.

Herein, we used QM/MM metadynamics to unravel the racemization reaction of GC, discovering the crucial effect of the catalyst carrying the proton from one oxygen to another and also, the importance of the C-O dihedral conformation to facilitate the nucleophilic attack of the deprotonated oxygen to the carbonylic carbon. We mapped the free-energy surface for two CVs that allowed us to efficiently describe the reaction. Exploring this free-energy surface we can differentiate all conformers (local minima) and transition states (saddle points) of the reaction.

We studied also the uncatalyzed decarboxylation reaction of GC to produce GL and CO<sub>2</sub>. We kept the same procedure as in the previous study of racemization reaction, hence analyzing the structural changes during the simulation and determining the activation energy of the reaction. Finally, we aimed to investigate the effect of CO<sub>2</sub> pressure on the rate of both reactions. We observed that we only can take into account the effect of the pressure on the system, since the concentration of the CO<sub>2</sub> requires a more complex simulation involving the equilibrium of the reaction. The observed trend when increasing the pressure is the opposite for the two reactions. The more we increase the pressure to the system, the more the rate increases in the racemization reaction and alternatively, the more decreases the rate in decarboxylation reaction.

UNIVERSITAT ROVIRA I VIRGILI

Computational Design of Catalysts for Carbon Dioxide Recycling

Joan González Fabra

*“Research is what I’m doing when I  
don’t know what I’m doing.”  
Wernher von Braun*

# Chapter 7

## Conclusions

In this Thesis we studied computationally several reactions where carbon dioxide was used as substrate. We described in detail the reaction mechanism for all cases, taking into consideration the experimental results provided by our collaborators. The results collected in this Thesis contribute to understand better how important CO<sub>2</sub> fixation reactions work and consequently, these results may help in the rational design of new and more active catalysts for this type of reactions involving CO<sub>2</sub> or substrates of similar properties.

Below we summarize the most relevant conclusions for each chapter of this Thesis. A more detailed description can be found in the last section of each chapter.

### **Chapter 3: Cyclic carbonates**

In the first part of this chapter we analyzed the influence of i) solvation, ii) translational entropy and iii) the DFT functional in the calculated Gibbs free-energy profile for the reaction of 1,2-epoxyhexane and CO<sub>2</sub>. Different approaches for correcting the entropy in solution have been

evaluated. The corrections proposed by Martin and Wertz and Ziegler lead to similar results in correlation with the experimental reference. Accounting dispersions corrections have found to be crucial, although when considering the entropy corrections, the description of the system by B3LYP have found to be reasonable.

In the second part of the Chapter we elucidated the reaction mechanism of CO<sub>2</sub> and epoxy-alcohols catalyzed only by an aluminum aminotriphenolate complex. Several mechanistic pathways were compared in order to determine the reaction order of the catalyst and explain the regioselectivity and enantioselectivity observed experimentally. The reaction mechanism catalyzed by one Al-complex and co-catalyzed by a water molecule was found to be the most feasible one. This reaction mechanism occurs in a concerted manner where the CO<sub>2</sub> insertion and the ring-closing step take place at the same time. This type of mechanism was not observed previously in similar systems when simple epoxides were used instead of functionalized epoxides. Moreover, the experimentally observed enantioselectivity was explained by a racemization process that occurs during the characterization of the product.

The results collected in this chapter advocate that a proper combination of DFT and entropic corrections may be combined with experimental characterization to study in detail a complex system and therefore, design new catalysts to contribute in the field of CO<sub>2</sub> fixation with efficient processes.

#### **Chapter 4: N-Aryl Carbamates**

In this chapter we elucidated by DFT methods the organocatalyzed reaction mechanism of cyclic carbonates and arylamines to efficiently and selectively produce N-aryl carbamates. We compared the catalytic activity of TBD with water, demonstrating the high efficiency of the chosen organocatalyst. Additionally, we also analyzed the reaction mechanism of alkylamines and arylamines. As expected, we observed higher reactivity



for alkylamines for the uncatalyzed reaction. Nevertheless, when TBD is used, similar both substrates present similar reactivity.

## Chapter 5: Polycarbonates

This chapter is divided in two parts. In the first part, we investigated in detail the reaction mechanism of cyclohexene and CO<sub>2</sub> to produce polycarbonates. We compared several mechanistic routes including a monometallic route that was found to be unfeasible, and two bimetallic pathways considering two Al-complexes separated or forming a non-covalent dimer. Also, we raised two different carbonyl attacks in the propagation step to explain the regioselectivity of the process. The dimeric structure was the most catalytically active species, thus leading to the most energetically favorable pathway. In order to evaluate the effect of the nucleophilic co-catalyst and the aromatic substituents of the ligand of the catalyst, we tested different binary catalytic systems, observing that using chloride as nucleophile and aromatic substituent of the ligand the absolute barrier of the process decreased compared to the system using iodide as nucleophile or the ligand of the catalyst with methyl groups in the aromatic positions.

The second part of the chapter reports our findings on the reaction mechanism between limonene oxide and CO<sub>2</sub> to form a renewable and bio-based polycarbonate. We pay special attention in the stereoregularity of the obtained polymer due to the complexity of limonene oxide, which presents three stereocenters in its structure. Therefore, we compared the relative barrier of the epoxide ring-opening process when using chloride or bromide and also when attacking both carbon atoms of the epoxide, observing a non-expected preference for the most substituted one. Then, we considered the most energetically plausible pathways to produce polycarbonate, proving the preference for the formation of *trans* polycarbonate from *cis* epoxide, hence observing inversion of configuration when the most substituted carbon was attacked through an S<sub>N</sub>2 type reaction mechanism. Our computational results were found to be in full agreement with the experimental observations.

## **Chapter 6: Effect of CO<sub>2</sub> Pressure**

The last chapter of the Thesis collects our results regarding the study of the effect of CO<sub>2</sub> pressure in two different reactions. In this chapter we used multiscale metadynamics to map the free-energy surface of the racemization and decarboxylation reactions of glycidol carbonate, which is the product of the reaction studied in Chapter 3. Additionally, we also determined the Gibbs free-energy barrier of both processes, in agreement with our static DFT calculations. Also, we proved that the pressure of the system plays an important role in the absolute barrier of the process. If we consider a dissociation reaction like decarboxylation, the reaction rate decreases when increasing the pressure. Alternatively, when an associative mechanism like racemization is studied, the reaction rate is accelerated when increasing the pressure in the system.

# References

- [1] M. Roser and E. Ortiz-Ospina in *World Population Growth. Published online at OurWorldInData.org*, Vol. **2018**.
- [2] J. W. Erisman, M. A. Sutton, J. Galloway, Z. Klimont and W. Winiwarter, *Nature Geoscience* **2008**, *1*, 636.
- [3] H. Shaftel, R. Jackson and S. Callery in *Global Climate Change. Retrieved from: <https://climate.nasa.gov/>*, Vol. **2018**.
- [4] P. Ciais, C. Sabine, G. Bala, L. Bopp, V. Brovkin, J. Canadell, A. Chhabra, R. DeFries, J. Galloway, M. Heimann, C. Jones, C. Le Quéré, R. B. Myneni, S. Piao and P. Thornton in *Carbon and Other Biogeochemical Cycles*, Vol. Eds.: T. F. Stocker, D. Qin, G.-K. Plattner, M. Tignor, S. K. Allen, J. Boschung, A. Nauels, Y. Xia, V. Bex and P. M. Midgley), Cambridge University Press, Cambridge, United Kingdom and New York, NY, USA, **2013**, pp. 465–570.
- [5] a) N. L. Bindoff, P. A. Stott, K. M. AchutaRao, M. R. Allen, N. Gillett, D. Gutzler, K. Hansingo, G. Hegerl, Y. Hu, S. Jain, I. I. Mokhov, J. Overland, J. Perlwitz, R. Sebbani and X. Zhang in *Detection and Attribution of Climate Change: from Global to Regional*, Vol. Eds.: T. F. Stocker, D. Qin, G.-K. Plattner, M. Tignor, S. K. Allen, J. Boschung, A. Nauels, Y. Xia, V. Bex and P. M. Midgley), Cambridge University Press, Cambridge, United Kingdom and New York, NY, USA, **2013**, pp. 867–952; b) J. H. Christensen, K. Krishna Kumar, E. Aldrian, S.-I. An, I. F. A. Cavalcanti, M. de Castro, W. Dong, P. Goswami, A. Hall, J. K. Kanyanga, A. Kitoh, J. Kossin, N.-C. Lau, J. Renwick, D. B. Stephenson, S.-P. Xie and T. Zhou in *Climate Phenomena and their Relevance for Future Regional Climate Change*, Vol. Eds.: T. F. Stocker, D. Qin, G.-K. Plattner, M. Tignor, S. K. Allen, J. Boschung, A. Nauels, Y. Xia, V. Bex and P. M. Midgley), Cambridge University Press, Cambridge, United Kingdom and New York, NY, USA, **2013**, pp. 1217–1308; c) M. Collins, R. Knutti, J. Arblaster, J.-L. Dufresne, T. Fichet, P. Friedlingstein, X. Gao, W. J. Gutowski, T. Johns, G. Krinner, M. Shongwe, C. Tebaldi, A. J. Weaver and M. Wehner in *Long-term Climate Change: Projections, Commitments and Irreversibility*, Vol. Eds.: T. F. Stocker, D. Qin, G.-K. Plattner, M. Tignor, S. K. Allen, J. Boschung, A. Nauels, Y. Xia, V. Bex and P. M. Midgley), Cambridge University Press, Cambridge, United Kingdom and New York, NY, USA, **2013**, pp. 1029–1136.
- [6] J. A. Church, P. U. Clark, A. Cazenave, J. M. Gregory, S. Jevrejeva, A. Levermann, M. A. Merrifield, G. A. Milne, R. S. Nerem, P. D. Nunn, A. J. Payne, W. T. Pfeffer, D. Stammer and A. S. Unnikrishnan in *Sea Level Change*, Vol. Eds.: T. F. Stocker, D. Qin, G.-K. Plattner, M. Tignor, S. K. Allen, J. Boschung, A. Nauels, Y. Xia, V. Bex and P. M. Midgley), Cambridge University Press, Cambridge, United Kingdom and New York, NY, USA, **2013**, pp. 1137–1216.
- [7] a) P. M. Cox, R. A. Betts, C. D. Jones, S. A. Spall and I. J. Totterdell, *Nature* **2000**, *408*, 184; b) M. Aresta and A. Dibenedetto, *Catalysis Today* **2004**, *98*, 455-462; c) S. M. Benson and F. M. Orr, *MRS Bulletin* **2008**, *33*, 303-305; d) S. Solomon, G.-K. Plattner, R. Knutti and P. Friedlingstein, *Proceedings of the National Academy of Sciences* **2009**.
- [8] G. A. Olah, G. K. S. Prakash and A. Goepfert, *Journal of the American Chemical Society* **2011**, *133*, 12881-12898.

- [9] S. L. Wells and J. DeSimone, *Angewandte Chemie International Edition* **2001**, *40*, 518-527.
- [10] a) M. Aresta, A. Dibenedetto and A. Angelini, *Chemical Reviews* **2014**, *114*, 1709-1742; b) P. Styring, E. Quadrelli and K. Armstrong, *Carbon Dioxide Utilisation: Closing the Carbon Cycle: First Edition*, **2014**, p. 1-311; c) Q. Liu, L. Wu, R. Jackstell and M. Beller, *Nat Commun* **2015**, *6*.
- [11] a) M. Pérez-Forbes, A. Bocin-Dumitriu and E. Tzimas, *Energy Procedia* **2014**, *63*, 7968-7975; b) I. Dimitriou, P. Garcia-Gutierrez, R. H. Elder, R. M. Cuellar-Franca, A. Azapagic and R. W. K. Allen, *Energy & Environmental Science* **2015**, *8*, 1775-1789; c) H. Naims, *Environmental Science and Pollution Research* **2016**, *23*, 22226-22241.
- [12] W. Steffen, K. Richardson, J. Rockström, S. E. Cornell, I. Fetzer, E. M. Bennett, R. Biggs, S. R. Carpenter, W. de Vries, C. A. de Wit, C. Folke, D. Gerten, J. Heinke, G. M. Mace, L. M. Persson, V. Ramanathan, B. Reyers and S. Sörlin, *Science* **2015**, *347*.
- [13] a) G. Centi and S. Perathoner, *Catalysis Today* **2009**, *148*, 191-205; b) A. A. Peterson, F. Abild-Pedersen, F. Studt, J. Rossmeisl and J. K. Nørskov, *Energy & Environmental Science* **2010**, *3*, 1311-1315; c) D. Kim, J. Resasco, Y. Yu, A. M. Asiri and P. Yang, *Nature Communications* **2014**, *5*, 4948.
- [14] L. Walter, *Angewandte Chemie International Edition in English* **1995**, *34*, 2207-2221.
- [15] a) M. Mikkelsen, M. Jorgensen and F. C. Krebs, *Energy & Environmental Science* **2010**, *3*, 43-81; b) W. Wang, S. Wang, X. Ma and J. Gong, *Chemical Society Reviews* **2011**, *40*, 3703-3727; c) G. Centi, E. A. Quadrelli and S. Perathoner, *Energy & Environmental Science* **2013**, *6*, 1711-1731.
- [16] T. Sakakura, J.-C. Choi and H. Yasuda, *Chemical Reviews* **2007**, *107*, 2365-2387.
- [17] a) K. H., *Justus Liebig's Annalen der Chemie* **1860**, *113*, 125-127; b) S. R., *Journal für Praktische Chemie* **1885**, *31*, 397-411.
- [18] J. Louie, J. E. Gibby, M. V. Farnworth and T. N. Tekavec, *Journal of the American Chemical Society* **2002**, *124*, 15188-15189.
- [19] a) T. Fujihara, T. Xu, K. Semba, J. Terao and Y. Tsuji, *Angewandte Chemie International Edition* **2011**, *50*, 523-527; b) Y. Zhang and S. N. Riduan, *Angewandte Chemie International Edition* **2011**, *50*, 6210-6212.
- [20] a) S. Feng, D. Youquan, S. Tianlong, P. Jiajian, G. Yanlong and Q. Botao, *Angewandte Chemie* **2003**, *115*, 3379-3382; b) O. Jacquet, C. Das Neves Gomes, M. Ephritikhine and T. Cantat, *Journal of the American Chemical Society* **2012**, *134*, 2934-2937; c) L. Yuchui, F. Xianjie, J. Kathrin and B. Matthias, *Angewandte Chemie International Edition* **2013**, *52*, 9568-9571.
- [21] A. Wurtz, *Comptes rendus* **1859**, *48*, 5.
- [22] M. Cokoja, C. Bruckmeier, B. Rieger, W. A. Herrmann and F. E. Kühn, *Angewandte Chemie International Edition* **2011**, *50*, 8510-8537.
- [23] a) W. Xia, K. A. Salmeia, S. I. Vagin and B. Rieger, *Chemistry – A European Journal* **2015**, *21*, 4384-4390; b) H. Zhang, X. Lin, S. Chin and M. W. Grinstaff, *Journal of the American Chemical Society* **2015**, *137*, 12660-12666.
- [24] a) D. Adhikari, S. T. Nguyen and M.-H. Baik, *Chemical Communications* **2014**, *50*, 2676-2678; b) S. Elmas, M. A. Subhani, M. Harrer, W. Leitner, J. Sundermeyer and T. E. Muller, *Catalysis Science & Technology* **2014**, *4*, 1652-1657.
- [25] a) K. Nakano, K. Kobayashi, T. Ohkawara, H. Imoto and K. Nozaki, *Journal of the American Chemical Society* **2013**, *135*, 8456-8459; b) M. Taherimehr, S. M. Al-Amsyar, C. J. Whiteoak, A. W. Kleij and P. P. Pescarmona, *Green Chemistry* **2013**, *15*, 3083-3090.
- [26] a) M. R. Kember, P. D. Knight, P. T. R. Reung and C. K. Williams, *Angewandte Chemie International Edition* **2009**, *48*, 931-933; b) R. Ma, L.-N. He and Y.-B. Zhou, *Green Chemistry* **2015**.

- [27] a) M. R. Kember and C. K. Williams, *Journal of the American Chemical Society* **2012**, *134*, 15676-15679; b) T. Ema, Y. Miyazaki, J. Shimonishi, C. Maeda and J.-y. Hasegawa, *Journal of the American Chemical Society* **2014**, *136*, 15270-15279.
- [28] a) S. Supasitmongkol and P. Styring, *Catalysis Science & Technology* **2014**, *4*, 1622-1630; b) M. North, S. C. Z. Quek, N. E. Pridmore, A. C. Whitwood and X. Wu, *ACS Catalysis* **2015**, *5*, 3398-3402.
- [29] a) T. Aida and S. Inoue, *Journal of the American Chemical Society* **1983**, *105*, 1304-1309; b) S. Hiroshi and I. Shohei, *Journal of Polymer Science Part A: Polymer Chemistry* **2004**, *42*, 5561-5573.
- [30] a) D. J. Darensbourg and M. W. Holtcamp, *Coordination Chemistry Reviews* **1996**, *153*, 155-174; b) D. J. Darensbourg and J. C. Yarbrough, *Journal of the American Chemical Society* **2002**, *124*, 6335-6342; c) D. J. Darensbourg and A. D. Yeung, *Polymer Chemistry* **2014**, *5*, 3949-3962.
- [31] G. Zemplén and A. Kunz, *Chemische Berichte* **1922**, *55*, 13.
- [32] A. Chandrasekaran, R. O. Day and R. R. Holmes, *Journal of the American Chemical Society* **2000**, *122*, 1066-1072.
- [33] a) C. J. Whiteoak, N. Kielland, V. Laserna, E. C. Escudero-Adán, E. Martin and A. W. Kleij, *Journal of the American Chemical Society* **2013**, *135*, 1228-1231; b) P. C. Leticia, G. F. Joan, C. G. Fernando, B. Carles and K. A. W., *Chemistry – A European Journal* **2015**, *21*, 6115-6122.
- [34] a) R. Tanaka, M. Yamashita, L. W. Chung, K. Morokuma and K. Nozaki, *Organometallics* **2011**, *30*, 6742-6750; b) T. Walter, *Angewandte Chemie International Edition* **2014**, *53*, 8605-8613.
- [35] a) A. Buchard, F. Jutz, M. R. Kember, A. J. P. White, H. S. Rzepa and C. K. Williams, *Macromolecules* **2012**, *45*, 6781-6795; b) S. Kissling, P. T. Altenbuchner, M. W. Lehenmeier, E. Herdtweck, P. Deglmann, U. B. Seemann and B. Rieger, *Chemistry – A European Journal* **2015**, *21*, 8148-8157.
- [36] P. Hohenberg and W. Kohn, *Physical Review* **1964**, *136*, B864-B871.
- [37] W. Kohn and L. J. Sham, *Physical Review* **1965**, *140*, A1133-A1138.
- [38] A. D. Becke, *Physical Review A* **1988**, *38*, 3098-3100.
- [39] a) J. P. Perdew, *Physical Review B* **1986**, *34*, 7406-7406; b) J. P. Perdew, *Physical Review B* **1986**, *33*, 8822-8824.
- [40] C. Lee, W. Yang and R. G. Parr, *Physical Review B* **1988**, *37*, 785-789.
- [41] S. Grimme, *Journal of Computational Chemistry* **2006**, *27*, 1787-1799.
- [42] S. Grimme, S. Ehrlich and L. Goerigk, *Journal of Computational Chemistry* **2011**, *32*, 1456-1465.
- [43] A. D. Becke, *The Journal of Chemical Physics* **1993**, *98*, 5648-5652.
- [44] J.-D. Chai and M. Head-Gordon, *Physical Chemistry Chemical Physics* **2008**, *10*, 6615-6620.
- [45] Y. Zhao and D. G. Truhlar, *The Journal of Chemical Physics* **2006**, *125*, 194101.
- [46] Y. Zhao, N. E. Schultz and D. G. Truhlar, *Journal of Chemical Theory and Computation* **2006**, *2*, 364-382.
- [47] S. Grimme, *Journal of Computational Chemistry* **2004**, *25*, 1463-1473.
- [48] S. A. Grimme, J.; Ehrlich, S.; Krieg, H., *The Journal of Chemical Physics* **2010**, *132*, 154104.
- [49] G. Stefan, *Journal of Computational Chemistry* **2006**, *27*, 1787-1799.
- [50] a) J. Tomasi and M. Persico, *Chemical Reviews* **1994**, *94*, 2027-2094; b) J. Tomasi, B. Mennucci and R. Cammi, *Chemical Reviews* **2005**, *105*, 2999-3094.

- [51] a) S. Miertuš, E. Scrocco and J. Tomasi, *Chemical Physics* **1981**, *55*, 117-129; b) M. Cossi, V. Barone, R. Cammi and J. Tomasi, *Chemical Physics Letters* **1996**, *255*, 327-335.
- [52] A. V. Marenich, C. J. Cramer and D. G. Truhlar, *The Journal of Physical Chemistry B* **2009**, *113*, 6378-6396.
- [53] a) Y. Liang, S. Liu, Y. Xia, Y. Li and Z.-X. Yu, *Chemistry – A European Journal* **2008**, *14*, 4361-4373; b) M.-A. Courtemanche, M.-A. Légaré, L. Maron and F.-G. Fontaine, *Journal of the American Chemical Society* **2014**, *136*, 10708-10717.
- [54] D. H. Wertz, *Journal of the American Chemical Society* **1980**, *102*, 5316-5322.
- [55] J. Cooper and T. Ziegler, *Inorganic Chemistry* **2002**, *41*, 6614-6622.
- [56] R. L. Martin, P. J. Hay and L. R. Pratt, *The Journal of Physical Chemistry A* **1998**, *102*, 3565-3573.
- [57] A. Laio and M. Parrinello, *Proceedings of the National Academy of Sciences* **2002**, *99*, 12562-12566.
- [58] V. Van Speybroeck, K. De Wispelaere, J. Van der Mynsbrugge, M. Vandichel, K. Hemelsoet and M. Waroquier, *Chemical Society Reviews* **2014**, *43*, 7326-7357.
- [59] X. Biarnés, A. Ardèvol, J. Iglesias-Fernández, A. Planas and C. Rovira, *Journal of the American Chemical Society* **2011**, *133*, 20301-20309.
- [60] A. Barducci, M. Bonomi and M. Parrinello, *Wiley Interdisciplinary Reviews: Computational Molecular Science* **2011**, *1*, 826-843.
- [61] B. Ensing, M. De Vivo, Z. Liu, P. Moore and M. L. Klein, *Accounts of Chemical Research* **2006**, *39*, 73-81.
- [62] G. M. Torrie and J. P. Valleau, *Journal of Computational Physics* **1977**, *23*, 187-199.
- [63] A. Laio, A. Rodriguez-Forteza, F. L. Gervasio, M. Ceccarelli and M. Parrinello, *The Journal of Physical Chemistry B* **2005**, *109*, 6714-6721.
- [64] A. Warshel and M. Levitt, *Journal of Molecular Biology* **1976**, *103*, 227-249.
- [65] M. Feliu and M. Keiji, *Journal of Computational Chemistry* **1995**, *16*, 1170-1179.
- [66] R. E. Buló, B. Ensing, J. Sikkema and L. Visscher, *Journal of Chemical Theory and Computation* **2009**, *5*, 2212-2221.
- [67] J. C. R., B. S. Maya, B. R. E., G. A. S. Pereira, G. A. W., K. Karin, S. Jetze and V. Lucas, *Journal of Computational Chemistry* **2011**, *32*, 2328-2338.
- [68] in *Observations: Atmosphere and Surface, Vol.* (Ed. C. Intergovernmental Panel on Climate), Cambridge University Press, Cambridge, **2014**, pp. 159-254.
- [69] a) R. Revelle and H. E. Suess, *Tellus* **1957**, *9*, 18-27; b) U. Siegenthaler and J. L. Sarmiento, *Nature* **1993**, *365*, 119; c) H. Arakawa, M. Aresta, J. N. Armor, M. A. Barteau, E. J. Beckman, A. T. Bell, J. E. Bercaw, C. Creutz, E. Dinjus, D. A. Dixon, K. Domen, D. L. DuBois, J. Eckert, E. Fujita, D. H. Gibson, W. A. Goddard, D. W. Goodman, J. Keller, G. J. Kubas, H. H. Kung, J. E. Lyons, L. E. Manzer, T. J. Marks, K. Morokuma, K. M. Nicholas, R. Periana, L. Que, J. Rostrup-Nielsen, W. M. H. Sachtler, L. D. Schmidt, A. Sen, G. A. Somorjai, P. C. Stair, B. R. Stults and W. Tumas, *Chemical Reviews* **2001**, *101*, 953-996; d) W. Cramer, A. Bondeau, S. Schaphoff, W. Lucht, B. Smith and S. Sitch, *Philosophical Transactions of the Royal Society of London. Series B: Biological Sciences* **2004**, *359*, 331-343; e) A. Otto, T. Grube, S. Schiebahn and D. Stolten, *Energy & Environmental Science* **2015**, *8*, 3283-3297.
- [70] a) A. Behr, *Angewandte Chemie International Edition in English* **1988**, *27*, 661-678; b) L. Plasseraud, *ChemSusChem* **2010**, *3*, 631-632; c) C.-C. Hwang, J. J. Tour, C. Kittrell, L. Espinal, L. B. Alemany and J. M. Tour, *Nature Communications* **2014**, *5*, 3961.

- [71] a) M. North and R. Pasquale, *Angewandte Chemie International Edition* **2009**, *48*, 2946-2948; b) A. Decortes, A. M. Castilla and A. W. Kleij, *Angewandte Chemie International Edition* **2010**, *49*, 9822-9837; c) H. Büttner, L. Longwitz, J. Steinbauer, C. Wulf and T. Werner, *Topics in Current Chemistry* **2017**, *375*, 50.
- [72] H.-J. Buysch in *Carbonic Esters, Vol.* **2000**.
- [73] A.-A. G. Shaikh and S. Sivaram, *Chemical Reviews* **1996**, *96*, 951-976.
- [74] a) J. Sun, S.-i. Fujita and M. Arai, *Journal of Organometallic Chemistry* **2005**, *690*, 3490-3497; b) M. F. Rojas, F. L. Bernard, A. Aquino, J. Borges, F. D. Vecchia, S. Menezes, R. Ligabue and S. Einloft, *Journal of Molecular Catalysis A: Chemical* **2014**, *392*, 83-88.
- [75] Y. Jung, T. Shin, K. Kim, H. Byun, S. J. Cho, H. Kim and H. Song, *Chemical Communications* **2017**, *53*, 384-387.
- [76] Y. Ren, C.-H. Guo, J.-F. Jia and H.-S. Wu, *The Journal of Physical Chemistry A* **2011**, *115*, 2258-2267.
- [77] V. Caló, A. Nacci, A. Monopoli and A. Fanizzi, *Organic Letters* **2002**, *4*, 2561-2563.
- [78] a) J.-Q. Wang, J. Sun, W.-G. Cheng, K. Dong, X.-P. Zhang and S.-J. Zhang, *Physical Chemistry Chemical Physics* **2012**, *14*, 11021-11026; b) B. Chatelet, L. Joucla, J.-P. Dutasta, A. Martinez, K. C. Szeto and V. Dufaud, *Journal of the American Chemical Society* **2013**, *135*, 5348-5351; c) J. A. Castro-Osma, J. W. Comerford, S. Heath, O. Jones, M. Morcillo and M. North, *RSC Advances* **2015**, *5*, 3678-3685; d) S. Sopena, G. Fiorani, C. Martín and A. W. Kleij, *ChemSusChem* **2015**, *8*, 3248-3254; e) B. A. Vara, T. J. Struble, W. Wang, M. C. Dobish and J. N. Johnston, *Journal of the American Chemical Society* **2015**, *137*, 7302-7305.
- [79] a) A. Decortes and A. W. Kleij, *ChemCatChem* **2011**, *3*, 831-834; b) F. Castro-Gómez, G. Salassa, A. W. Kleij and C. Bo, *Chemistry – A European Journal* **2013**, *19*, 6289-6298; c) J. W. Comerford, I. D. V. Ingram, M. North and X. Wu, *Green Chemistry* **2015**, *17*, 1966-1987; d) D. Alhashmialameer, J. Collins, K. Hattenhauer and F. M. Kerton, *Catalysis Science & Technology* **2016**, *6*, 5364-5373.
- [80] a) J. Meléndez, M. North and R. Pasquale, *European Journal of Inorganic Chemistry* **2007**, *2007*, 3323-3326; b) C. Beattie, M. North, P. Villuendas and C. Young, *The Journal of Organic Chemistry* **2013**, *78*, 419-426; c) C. Beattie and M. North, *Chemistry – A European Journal* **2014**, *20*, 8182-8188; d) C. J. Whiteoak, N. Kielland, V. Laserna, F. Castro-Gómez, E. Martin, E. C. Escudero-Adán, C. Bo and A. W. Kleij, *Chemistry – A European Journal* **2014**, *20*, 2264-2275; e) S. H. Kim, S. Y. Han, J. H. Kim, Y. Y. Kang, J. Lee and Y. Kim, *European Journal of Inorganic Chemistry* **2015**, *2015*, 2323-2329; f) J. Martínez, J. A. Castro-Osma, A. Earlam, C. Alonso-Moreno, A. Otero, A. Lara-Sánchez, M. North and A. Rodríguez-Diéguez, *Chemistry – A European Journal* **2015**, *21*, 9850-9862; g) L. Cuesta-Aluja, J. Castilla and A. M. Masdeu-Bulto, *Dalton Transactions* **2016**, *45*, 14658-14667; h) J. Rintjema and A. W. Kleij, *ChemSusChem* **2017**, *10*, 1274-1282; i) P. Li and Z. Cao, *Organometallics* **2018**, *37*, 406-414.
- [81] L. Jin, H. Jing, T. Chang, X. Bu, L. Wang and Z. Liu, *Journal of Molecular Catalysis A: Chemical* **2007**, *261*, 262-266.
- [82] T. Ema, Y. Miyazaki, S. Koyama, Y. Yano and T. Sakai, *Chemical Communications* **2012**, *48*, 4489-4491.
- [83] R. L. Paddock and S. T. Nguyen, *Journal of the American Chemical Society* **2001**, *123*, 11498-11499.
- [84] a) B. Valeria, R. Nino, C. Ugo, G. Claudio, M. Giorgio, P. Demetrio and S. Emilia, *ChemCatChem* **2016**, *8*, 1167-1175; b) M. North, R. Pasquale and C. Young, *Green Chemistry* **2010**, *12*, 1514-1539.

- [85] a) S. Kozuch, S. E. Lee and S. Shaik, *Organometallics* **2009**, *28*, 1303-1308; b) S. Kozuch and S. Shaik, *Accounts of Chemical Research* **2011**, *44*, 101-110; c) K. Sebastian, *Wiley Interdisciplinary Reviews: Computational Molecular Science* **2012**, *2*, 795-815.
- [86] M. J. T. Frisch, G. W.; Schlegel, H. B.; Scuseria, G. E.; Robb, M. A.; Cheeseman, J. R.; Scalmani, G.; Barone, V.; Mennucci, B.; Petersson, G. A.; Nakatsuji, H.; Caricato, M.; Li, X.; Hratchian, H. P.; Izmaylov, A. F.; Bloino, J.; Zheng, G.; Sonnenberg, J. L.; Hada, M.; Ehara, M.; Toyota, K.; Fukuda, R.; Hasegawa, J.; Ishida, M.; Nakajima, T.; Honda, Y.; Kitao, O.; Nakai, H.; Vreven, T.; Montgomery, J. A., Jr.; Peralta, J. E.; Ogliaro, F.; Bearpark, M.; Heyd, J. J.; Brothers, E.; Kudin, K. N.; Staroverov, V. N.; Kobayashi, R.; Normand, J.; Raghavachari, K.; Rendell, A.; Burant, J. C.; Iyengar, S. S.; Tomasi, J.; Cossi, M.; Rega, N.; Millam, M. J.; Klene, M.; Knox, J. E.; Cross, J. B.; Bakken, V.; Adamo, C.; Jaramillo, J.; Gomperts, R.; Stratmann, R. E.; Yazyev, O.; Austin, A. J.; Cammi, R.; Pomelli, C.; Ochterski, J. W.; Martin, R. L.; Morokuma, K.; Zakrzewski, V. G.; Voth, G. A.; Salvador, P.; Dannenberg, J. J.; Dapprich, S.; Daniels, A. D.; Farkas, Ö.; Foresman, J. B.; Ortiz, J. V.; Cioslowski, J.; Fox, D. J. in *Gaussian 09, Revision D.01*, Vol. Gaussian, Inc., Wallingford CT, **2009**.
- [87] a) A. D. Becke, *The Journal of Chemical Physics* **1996**, *104*, 1040-1046; b) G. Stefan, E. Stephan and G. Lars, *Journal of Computational Chemistry* **2011**, *32*, 1456-1465.
- [88] Y. Zhao and D. G. Truhlar, *Theoretical Chemistry Accounts* **2008**, *120*, 215-241.
- [89] a) R. Krishnan, J. S. Binkley, R. Seeger and J. A. Pople, *The Journal of Chemical Physics* **1980**, *72*, 650-654; b) A. D. McLean and G. S. Chandler, *The Journal of Chemical Physics* **1980**, *72*, 5639-5648.
- [90] P. J. Hay and W. R. Wadt, *The Journal of Chemical Physics* **1985**, *82*, 270-283.
- [91] D. R. Lide, *CRC Handbook of Chemistry and Physics, 84th Edition*, Taylor & Francis, **2003**, p.
- [92] C. Zazza, A. Amadei, A. Palma, N. Sanna, S. Tatoli and M. Aschi, *The Journal of Physical Chemistry B* **2008**, *112*, 3184-3192.
- [93] U. Andreas, K. Sebastian and S. Sason, *Journal of Computational Chemistry* **2011**, *32*, 978-985.
- [94] a) Z.-X. Yu and K. N. Houk, *Journal of the American Chemical Society* **2003**, *125*, 13825-13830; b) L. Yong, L. Song, X. Yuanzhi, L. Yahong and Y. Zhi-Xiang, *Chemistry – A European Journal* **2008**, *14*, 4361-4373; c) P. A. Dub and R. Poli, *Journal of Molecular Catalysis A: Chemical* **2010**, *324*, 89-96; d) P. A. Dub and T. Ikariya, *Journal of the American Chemical Society* **2013**, *135*, 2604-2619; e) S. Qu, Y. Dang, C. Song, M. Wen, K.-W. Huang and Z.-X. Wang, *Journal of the American Chemical Society* **2014**, *136*, 4974-4991.
- [95] A. D. Becke, *The Journal of Chemical Physics* **1997**, *107*, 8554-8560.
- [96] R. D. J. III, *NIST Standard Reference Database Number 101* **2016**, *18*.
- [97] J. P. Perdew, K. Burke and Y. Wang, *Physical Review B* **1996**, *54*, 16533-16539.
- [98] a) C. K. De, E. G. Klauber and D. Seidel, *Journal of the American Chemical Society* **2009**, *131*, 17060-17061; b) P. P. M., *Angewandte Chemie International Edition* **2004**, *43*, 2062-2064; c) P. R. Schreiner, *Chemical Society Reviews* **2003**, *32*, 289-296; d) S. Sergio, F. Giulia, M. Carmen and K. A. W., *ChemSusChem* **2015**, *8*, 3248-3254; e) E. Van Lenthe, E. J. Baerends and J. G. Snijders, *The Journal of Chemical Physics* **1993**, *99*, 4597-4610.
- [99] a) M. R. Kember, A. Buchard and C. K. Williams, *Chemical Communications* **2011**, *47*, 141-163; b) X.-B. Lu and D. J. Darensbourg, *Chemical Society Reviews* **2012**, *41*, 1462-1484; c) C. G. W. and M. D. R., *Angewandte Chemie International Edition* **2004**, *43*, 6618-6639.
- [100] a) B. Enguerrand, P. Jacky and C. Thibault, *Angewandte Chemie International Edition* **2014**, *53*, 12186-12190; b) B. Kassem, v. S. Thorsten, K. Jürgen and L. Walter, *Angewandte Chemie International Edition* **2013**, *52*, 9554-9557; c) W. Sebastian, H. Ulrich and L. Walter, *Angewandte Chemie*



*International Edition* **2012**, *51*, 8585-8588; d) L. Yuehui, Y. Tao, J. Kathrin and B. Matthias, *Angewandte Chemie International Edition* **2014**, *53*, 10476-10480.

[101] J. H. Clements, *Industrial & Engineering Chemistry Research* **2003**, *42*, 663-674.

[102] a) W. Binshen, Y. Sijuan, M. Lijun, G. Yanlong, Z. Yongya, W. Xiaopei, Z. Lifeng, E. E. H. M., W. Shi and G. Guohua, *Advanced Synthesis & Catalysis* **2014**, *356*, 3125-3134; b) M. J. Gresser and W. P. Jencks, *Journal of the American Chemical Society* **1977**, *99*, 6963-6970; c) W. Guo, V. Laserna, E. Martin, E. C. Escudero-Adán and A. W. Kleij, *Chemistry – A European Journal* **2016**, *22*, 1722-1727; d) W. Guo, L. Martínez-Rodríguez, R. Kuniyil, E. Martin, E. C. Escudero-Adán, F. Maseras and A. W. Kleij, *Journal of the American Chemical Society* **2016**, *138*, 11970-11978.

[103] a) in *Stereoselective Aldol Condensations, Vol.*; b) D. A. Evans, J. S. Tedrow, J. T. Shaw and C. W. Downey, *Journal of the American Chemical Society* **2002**, *124*, 392-393.

[104] a) A. Cornille, R. Auvergne, O. Figovsky, B. Boutevin and S. Caillol, *European Polymer Journal* **2017**, *87*, 535-552; b) A. Cornille, M. Blain, R. Auvergne, B. Andrioletti, B. Boutevin and S. Caillol, *Polymer Chemistry* **2017**, *8*, 592-604; c) T. Hidetoshi, S. Fumio and E. Takeshi, *Journal of Polymer Science Part A: Polymer Chemistry* **2001**, *39*, 3678-3685; d) R. H. Lambeth and T. J. Henderson, *Polymer* **2013**, *54*, 5568-5573.

[105] H. J. Assumption and L. J. Mathias, *Polymer* **2003**, *44*, 5131-5136.

[106] W. Ye, J. Xu, C.-T. Tan and C.-H. Tan, *Tetrahedron Letters* **2005**, *46*, 6875-6878.

[107] D. Simoni, M. Rossi, R. Rondanin, A. Mazzali, R. Baruchello, C. Malagutti, M. Roberti and F. P. Invidiata, *Organic Letters* **2000**, *2*, 3765-3768.

[108] a) R. Chinchilla, C. Nájera and P. Sánchez-Agulló, *Tetrahedron: Asymmetry* **1994**, *5*, 1393-1402; b) D. Simoni, R. Rondanin, M. Morini, R. Baruchello and F. P. Invidiata, *Tetrahedron Letters* **2000**, *41*, 1607-1610.

[109] a) A. Chuma, H. W. Horn, W. C. Swope, R. C. Pratt, L. Zhang, B. G. G. Lohmeijer, C. G. Wade, R. M. Waymouth, J. L. Hedrick and J. E. Rice, *Journal of the American Chemical Society* **2008**, *130*, 6749-6754; b) R. C. Pratt, B. G. G. Lohmeijer, D. A. Long, R. M. Waymouth and J. L. Hedrick, *Journal of the American Chemical Society* **2006**, *128*, 4556-4557; c) L. Simón and J. M. Goodman, *The Journal of Organic Chemistry* **2007**, *72*, 9656-9662.

[110] N. Y. Rakhmanina and J. N. van den Anker, *Expert Opinion on Drug Metabolism & Toxicology* **2010**, *6*, 95-103.

[111] C. E. Stafstrom, S. Grippon and P. Kirkpatrick, *Nature Reviews Drug Discovery* **2011**, *10*, 729.

[112] a) M. Blain, L. Jean-Gerard, R. Auvergne, D. Benazet, S. Caillol and B. Andrioletti, *Green Chemistry* **2014**, *16*, 4286-4291; b) J. Gao, H. Li, Y. Zhang and Y. Zhang, *Green Chemistry* **2007**, *9*, 572-576; c) C. Han and Porco, *Organic Letters* **2007**, *9*, 1517-1520.

[113] D. Chaturvedi, *Tetrahedron* **2012**, *68*, 15-45.

[114] V. L. K. Valli and H. Alper, *The Journal of Organic Chemistry* **1995**, *60*, 257-258.

[115] D. Gaussian 09, Frisch, M. J.; Trucks, G. W.; Schlegel, H. B.; Scuseria, G. E.; Robb, M. A.; Cheeseman, J. R.; Scalmani, G.; Barone, V.; Mennucci, B.; Petersson, G. A.; Nakatsuji, H.; Caricato, M.; Li, X.; Hratchian, H. P.; Izmaylov, A. F.; Bloino, J.; Zheng, G.; Sonnenberg, J. L.; Hada, M.; Ehara, M.; Toyota, K.; Fukuda, R.; Hasegawa, J.; Ishida, M.; Nakajima, T.; Honda, Y.; Kitao, O.; Nakai, H.; Vreven, T.; Montgomery, J. A., Jr.; Peralta, J. E.; Ogliaro, F.; Bearpark, M.; Heyd, J. J.; Brothers, E.; Kudin, K. N.; Staroverov, V. N.; Kobayashi, R.; Normand, J.; Raghavachari, K.; Rendell, A.; Burant, J. C.; Iyengar, S. S.; Tomasi, J.; Cossi, M.; Rega, N.; Millam, J. M.; Klene, M.; Knox, J. E.; Cross, J. B.; Bakken, V.; Adamo, C.; Jaramillo, J.; Gomperts, R.; Stratmann, R. E.; Yazyev, O.; Austin, A. J.; Cammi, R.; Pomelli, C.; Ochterski, J. W.; Martin, R. L.; Morokuma, K.; Zakrzewski, V. G.; Voth, G. A.; Salvador, P.; Dannenberg, J. J.; Dapprich, S.;

Daniels, A. D.; Farkas, Ö.; Foresman, J. B.; Ortiz, J. V.; Cioslowski, J.; Fox, D. J., *Gaussian Inc., Wallingford CT* **2013**.

[116] A. D. Becke, *J. Chem. Phys.* **1997**, *107*, 8554-8560.

[117] R. Krishnan, J. S. Binkley, R. Seeger and J. A. Pople, *J. Chem. Phys.* **1980**, *72*, 650-654.

[118] a) R. J. Bartlett, *Ann. Rev. Phys. Chem.* **1981**, *32*, 359-401; b) R. J. Bartlett and G. D. Purvis, *Int. J. Quantum Chem.* **1978**, *14*, 561-581.

[119] J. A. Pople, M. Head-Gordon and K. Raghavachari, *J. Chem. Phys.* **1987**, *87*, 5968-5975.

[120] a) M. I. Childers, J. M. Longo, N. J. Van Zee, A. M. LaPointe and G. W. Coates, *Chemical Reviews* **2014**, *114*, 8129-8152; b) S. Paul, Y. Zhu, C. Romain, R. Brooks, P. K. Saini and C. K. Williams, *Chemical Communications* **2015**, *51*, 6459-6479.

[121] a) K. S. Bisht and T. F. Al-Azemi in *Synthesis of Functional Polycarbonates from Renewable Resources, Vol. 1043* American Chemical Society, **2010**, pp. 175-199; b) D. J. Darensbourg, W.-C. Chung, C. J. Arp, F.-T. Tsai and S. J. Kyran, *Macromolecules* **2014**, *47*, 7347-7353; c) Y. Wang, J. Fan and D. J. Darensbourg, *Angewandte Chemie International Edition* **2015**, *54*, 10206-10210.

[122] P. Braunstein, D. Matt and D. Nobel, *Journal of the American Chemical Society* **1988**, *110*, 3207-3212.

[123] Y. Li, J. Hong, R. Wei, Y. Zhang, Z. Tong, X. Zhang, B. Du, J. Xu and Z. Fan, *Chemical Science* **2015**, *6*, 1530-1536.

[124] H.-Y. Chen, J. Zhang, C.-C. Lin, J. H. Reibenspies and S. A. Miller, *Green Chemistry* **2007**, *9*, 1038-1040.

[125] C. Bakewell, G. Fateh-Iravani, D. W. Beh, D. Myers, S. Tabthong, P. Hormnirun, A. J. P. White, N. Long and C. K. Williams, *Dalton Transactions* **2015**, *44*, 12326-12337.

[126] a) L. Mespouille, O. Coulembier, M. Kawalec, A. P. Dove and P. Dubois, *Progress in Polymer Science* **2014**, *39*, 1144-1164; b) R. Nakano, S. Ito and K. Nozaki, *Nat Chem* **2014**, *6*, 325-331.

[127] T. Aida, M. Ishikawa and S. Inoue, *Macromolecules* **1986**, *19*, 8-13.

[128] a) K. Nakano, K. Kobayashi and K. Nozaki, *Journal of the American Chemical Society* **2011**, *133*, 10720-10723; b) X. Sheng, W. Wu, Y. Qin, X. Wang and F. Wang, *Polymer Chemistry* **2015**, *6*, 4719-4724.

[129] a) Z. Hošťálek, R. Mundil, I. Císařová, O. Trhlíková, E. Grau, F. Peruch, H. Cramail and J. Merna, *Polymer* **2015**, *63*, 52-61; b) M. Winkler, C. Romain, M. A. R. Meier and C. K. Williams, *Green Chemistry* **2015**, *17*, 300-306; c) H. Masahiro, N. Koji, O. Shin-ichi and N. Kyoko, *Chemistry – A European Journal* **2016**, *22*, 13677-13681; d) F.-T. Tsai, Y. Wang and D. J. Darensbourg, *Journal of the American Chemical Society* **2016**, *138*, 4626-4633.

[130] D. J. Darensbourg and A. D. Yeung, *Polymer Chemistry* **2015**, *6*, 1103-1117.

[131] D. J. Darensbourg, W.-C. Chung, A. D. Yeung and M. Luna, *Macromolecules* **2015**, *48*, 1679-1687.

[132] M. Reiter, S. Vagin, A. Kronast, C. Jandl and B. Rieger, *Chemical Science* **2017**, *8*, 1876-1882.

[133] M. W. Lehenmeier, C. Bruckmeier, S. Klaus, J. E. Dengler, P. Deglmann, A.-K. Ott and B. Rieger, *Chemistry – A European Journal* **2011**, *17*, 8858-8869.

[134] T. Ohkawara, K. Suzuki, K. Nakano, S. Mori and K. Nozaki, *Journal of the American Chemical Society* **2014**, *136*, 10728-10735.

[135] Y.-Z. Hua, X.-C. Yang, M.-M. Liu, X. Song, M.-C. Wang and J.-B. Chang, *Macromolecules* **2015**, *48*, 1651-1657.

- [136] C. T. Cohen, T. Chu and G. W. Coates, *Journal of the American Chemical Society* **2005**, *127*, 10869-10878.
- [137] H. Li and Y. Niu, *Reactive and Functional Polymers* **2011**, *71*, 121-125.
- [138] a) N. Pilkington and R. Robson, *Australian Journal of Chemistry* **1970**, *23*, 2225-2236; b) J. Gao, J. H. Reibenspies, R. A. Zingaro, F. R. Woolley, A. E. Martell and A. Clearfield, *Inorganic Chemistry* **2005**, *44*, 232-241.
- [139] M. W. Lehenmeier, S. Kissling, P. T. Altenbuchner, C. Bruckmeier, P. Deglmann, A.-K. Brym and B. Rieger, *Angewandte Chemie International Edition* **2013**, *52*, 9821-9826.
- [140] a) R. C. Jeske, A. M. DiCiccio and G. W. Coates, *Journal of the American Chemical Society* **2007**, *129*, 11330-11331; b) A. M. DiCiccio and G. W. Coates, *Journal of the American Chemical Society* **2011**, *133*, 10724-10727; c) N. J. Van Zee and G. W. Coates, *Chemical Communications* **2014**, *50*, 6322-6325; d) N. J. Van Zee and G. W. Coates, *Angewandte Chemie International Edition* **2015**, *54*, 2665-2668.
- [141] C. M. Byrne, S. D. Allen, E. B. Lobkovsky and G. W. Coates, *Journal of the American Chemical Society* **2004**, *126*, 11404-11405.
- [142] G.-F. Joan, C.-G. Fernando, K. A. W. and B. Carles, *ChemSusChem* **2017**, *10*, 1233-1240.
- [143] S. Charles, *Flavour and Fragrance Journal* **1995**, *10*, 60-60.
- [144] K. Jian, H. Shijun, L. Jin, Z. Min and S. Weiping, *Angewandte Chemie International Edition* **2015**, *54*, 2199-2203.
- [145] a) C. Shen, P. Zhang, Q. Sun, S. Bai, T. S. A. Hor and X. Liu, *Chemical Society Reviews* **2015**, *44*, 291-314; b) D. Zhongyu, R. Sadananda, Z. Pengfei and L. Xiaogang, *Chemistry – A European Journal* **2009**, *15*, 3666-3669.
- [146] a) J. Liu, C. Fan, H. Yin, C. Qin, G. Zhang, X. Zhang, H. Yi and A. Lei, *Chemical Communications* **2014**, *50*, 2145-2147; b) L. Jie, L. Qiang, Y. Hong, Q. Chu, B. Ruopeng, Q. Xiaotian, L. Yu and L. Aiwen, *Angewandte Chemie* **2014**, *126*, 512-516.
- [147] a) N. A. Till, R. T. Smith and D. W. C. MacMillan, *Journal of the American Chemical Society* **2018**, *140*, 5701-5705; b) C. C. Le and D. W. C. MacMillan, *Journal of the American Chemical Society* **2015**, *137*, 11938-11941; c) Z. Zuo, D. T. Ahneman, L. Chu, J. A. Terrett, A. G. Doyle and D. W. C. MacMillan, *Science* **2014**, *345*, 437-440; d) L. Candish, M. Freitag, T. Gensch and F. Glorius, *Chemical Science* **2017**, *8*, 3618-3622.
- [148] B. M. Trost in *Transition metal templates for selectivity in organic synthesis*, Vol. 53 **1981**, p. 2357.
- [149] a) J. Tsuji in *Catalytic reactions via  $\pi$ -allylpalladium complexes*, Vol. 54 **1982**, p. 197; b) J. Tsuji, I. Shimizu, I. Minami and Y. Ohashi, *Tetrahedron Letters* **1982**, *23*, 4809-4812; c) I. Minami, I. Shimizu and J. Tsuji, *Journal of Organometallic Chemistry* **1985**, *296*, 269-280.
- [150] M. Braun and T. Meier, *Angewandte Chemie International Edition* **2006**, *45*, 6952-6955.
- [151] a) M. Yoshida, M. Fujita, T. Ishii and M. Ihara, *Journal of the American Chemical Society* **2003**, *125*, 4874-4881; b) Y. Masahiro and I. Masataka, *Chemistry – A European Journal* **2004**, *10*, 2886-2893.
- [152] a) A. Cai, W. Guo, L. Martínez-Rodríguez and A. W. Kleij, *Journal of the American Chemical Society* **2016**, *138*, 14194-14197; b) W. Guo, L. Martínez-Rodríguez, E. Martín, E. C. Escudero-Adán and A. W. Kleij, *Angewandte Chemie International Edition* **2016**, *55*, 11037-11040.
- [153] L. Alessandro and L. G. Francesco, *Reports on Progress in Physics* **2008**, *71*, 126601.
- [154] S.-Y. Yang and T. Ziegler, *Organometallics* **2006**, *25*, 887-900.

- [155] A. Magistrato, T. K. Woo, A. Togni and U. Rothlisberger, *Organometallics* **2004**, *23*, 3218-3227.
- [156] T. K. Woo, P. M. Margl, L. Deng, L. Cavallo and T. Ziegler, *Catalysis Today* **1999**, *50*, 479-500.
- [157] L. Petersen, A. Ardèvol, C. Rovira and P. J. Reilly, *The Journal of Physical Chemistry B* **2009**, *113*, 7331-7339.
- [158] C. L. Stanton, I. F. W. Kuo, C. J. Mundy, T. Laino and K. N. Houk, *The Journal of Physical Chemistry B* **2007**, *111*, 12573-12581.
- [159] a) J. M. Boereboom, R. Potestio, D. Donadio and R. E. Bulo, *Journal of Chemical Theory and Computation* **2016**, *12*, 3441-3448; b) S. O. Nielsen, R. E. Bulo, P. B. Moore and B. Ensing, *Physical Chemistry Chemical Physics* **2010**, *12*, 12401-12414.
- [160] J. Řezáč, J. Fanfrlík, D. Salahub and P. Hobza, *Journal of Chemical Theory and Computation* **2009**, *5*, 1749-1760.
- [161] a) B. J. Alder and T. E. Wainwright, *The Journal of Chemical Physics* **1959**, *31*, 459-466; b) A. Rahman, *Physical Review* **1964**, *136*, A405-A411.
- [162] J. J. P. Stewart, *Journal of Computer-Aided Molecular Design* **1990**, *4*, 1-103.
- [163] a) W. L. Jorgensen, J. Chandrasekhar, J. D. Madura, R. W. Impey and M. L. Klein, *The Journal of Chemical Physics* **1983**, *79*, 926-935; b) B. B. R., B. R. E., O. B. D., S. D. J., S. S. and K. Martin, *Journal of Computational Chemistry* **1983**, *4*, 187-217.
- [164] M. T. Nelson, W. Humphrey, A. Gursoy, A. Dalke, L. V. Kalé, R. D. Skeel and K. Schulten, *The International Journal of Supercomputer Applications and High Performance Computing* **1996**, *10*, 251-268.
- [165] M. L., A. R., B. E. G. and M. J. M., *Journal of Computational Chemistry* **2009**, *30*, 2157-2164.
- [166] Y. S. Baek and C. H. Choi, *Journal of Chemical Theory and Computation* **2018**, *14*, 2312-2321.
- [167] a) N. D. Yilmazer and M. Korth, *The Journal of Physical Chemistry B* **2013**, *117*, 8075-8084; b) S. J. A. H., E. Ralf-Uwe, K. Ralph and S. Gerrit, *Journal of Physical Organic Chemistry* **2011**, *24*, 1072-1080; c) S. I. Gorelsky and A. B. P. Lever, *Journal of Organometallic Chemistry* **2001**, *635*, 187-196.
- [168] X. Gui, Z. Tang and W. Fei, *Journal of Chemical & Engineering Data* **2011**, *56*, 2420-2429.

UNIVERSITAT ROVIRA I VIRGILI

Computational Design of Catalysts for Carbon Dioxide Recycling

Joan González Fabra